THE EFFECT OF FLOW OSCILLATIONS ON CAVITY DRAG, AND A TECHNIQUE FOR THEIR CONTROL

Thesis by
Morteza Gharib

In Partial Fulfillment
of the Requirements for the Degree of
Doctor of Philosophy

California Institute of Technology
Pasadena, California

1983
(Submitted 20 May 1983)

ACKNOWLEDGEMENTS

I am grateful to my advisor Professor Anatol Roshko, who taught me the art of scientific research.

I would like to extend my thanks to Dr. Virendra Sarohia for his support and encouragement throughout this work. I am indebted to Drs. Luis Bernal, for his guidance and assistance during the difficult LDV measurements, and Dan Nosenchuck, for his assistance during the early strip-heater experiments. Thanks are also due to the technical staff of the Fluid Mechanics Group in the Jet Propulsion Laboratory, especially to chief technician Mr. Wayne Bixler and Messrs. Barny Green, Stan Kikkert and Robert Smither for their excellent workmanship and willing assistance in constructing the experimental apparatus. My thanks to fellow friends in GALCIT Dr. Miguel Hernan and Messrs. M.M. Koochesfahani and F.A. Roberts for their inspiration with ideas and stimulating discussions.

Financial support from the U.S. Army Research Office Contract No. 17134E and National Sciences Foundation Grant No. CME-7723541 is acknowledged.

I thank Mrs. Betty Wood for her drafting skills displayed in the graphs of the paper. My special thanks to Mrs. Kathy Eriksen for her assistance in organizing and typing the manuscript and for efforts beyond the call of duty.

This work has been successful through the continued love and support of my family, especially my wife Shohreh, through her excellent help in carrying out the experiments and her constant encouragement during difficult times.

ABSTRACT

The phenomenon of cavity flow oscillation is investigated to determine the conditions for onset of periodic oscillations and to understand the relationship between the state of the shear layer and the cavity drag. Experiments have been performed in a water tunnel using a 4" axisymmetric cavity model instrumented with a strip heater on the nose cone and pressure taps in and around the cavity. A complete set of measurements of oscillation phase, amplitude amplification along the flow direction, distribution of shear stress and other momentum flux is obtained by means of a laser Doppler velocimeter. Drag measurements were made by integrating the mean pressure over the solid surfaces of the cavity. Results indicated exponential cavity drag dependence on the length of the cavity. A jump in the cavity drag coefficient is observed as the cavity flow shows a bluff body wake type behavior. An independent estimate of the drag, which is obtained by integration of shear and mean momentum transfer terms over the peripheral area of the cavity, confirms the exponential dependence of drag on the length of the cavity. Results, also reveal that the drag of the cavity in the non-oscillating mode is less than the case if the cavity were replaced by a solid surface. Natural and forced oscillations of the cavity shear layer spanning the gap are studied. The forced oscillations are introduced by a sinusoidally heated thin-film strip which excites the Tollmein-Schlichting waves in the boundary layer upstream of the gap. For a sufficiently large gap, self-sustained periodic oscillations are observed while for smaller gaps, which do not oscillate naturally, periodic oscillations can be obtained by external forcing through the strip-heater. In the latter case resonance is observed whenever the forcing frequency satisfies the phase criterion $\frac{\varphi}{2\pi} = N$, and its amplitude

exceeds

certain threshold levels, but the phenomenon is non-self-supporting. The drag of the cavity can be increased by one order of magnitude in the non-oscillating case through external forcing. For naturally occurring oscillations, it is possible for two waves to co-exist in the shear layer (natural and forced). Also, it is possible to completely eliminate mode switching by applying external forcing. For the first time a test is performed to cancel or dampen the amplitude of Kelvin-Helmholtz wave in the cavity shear layer. This is done through introducing an external perturbation with the same frequency of the natural component but having a different phase. Reduction by a factor of 2 is obtained in the amplitude of the oscillation.

TABLE OF CONTENTS

LIST OF FIGURES

LIST OF SYMBOLS

Symbol	Description
A	frontal area for the model
A_1	cavities peripheral area
A_2	downstream face area (=A)
A_3	stings peripheral area
A_4	upstream face area
b	cavity width
b_{min}	minimum cavity width for self-sustained oscillations
b_{cr}	cavity width for transition to the wake mode
c	speed of sound
C_D	cavity drag coefficient
C_{DS}	sting drag coefficient
C_{DP}	pressure drag coefficient of the cavity
$C_{D\overline{uv}}$	drag coefficient based on $\overline{uv}$ term
$C_{\overline{uv}}$	drag coefficient based on edge velocity dynamic pressure
C_p	pressure coefficient based on edge veolcity dynamic pressure
$C_{P_{max}}$	maximum local pressure coefficient of the cavity
d	model diameter
dr	length element along the model radius
dx	length element along the cavity width
ds	sting diameter
F	frequency of the cavity flow oscillation
h	two-dimensional cavity depth
H	boundary layer shape factor $\left[\frac{\delta_0^*}{\theta_0}\right]$

κ	LDV conversion factor
κ_B	LDV conversion factor, blue channel
κ_G	LDV conversion factor, green channel
$\underline{n}$	direction cosine for the cavity surface
P	static pressure
P_e	free-stream static pressure oustide the upstream boundary layer
r	radius from center line of the model
R	model radius
R_e	Reynolds number based on model diameter
Re_{δ^*}	Reynolds number based on boundary layer displacement thickness
Re_θ	Reynolds number based on boundary layer momentum thickness
S	streamwise distance over the model nose
SH_1	location of first strip heater
SH_2	location of second strip heater
SH_3	location of third strip heater
u	streamwise velocity component
U_c	convection or phase velocity of the perturbation
U_e	free stream velocity outside the upstream boundary layer
v	transverse velocity component
w	strip heater width
x	streamwise direction
y	outward direction of the model perpendicular to x-z plane
$y_{.5}$	locus of $\frac{\overline{u}}{U_e} = .5$
z	vertical direction of the tunnel
α	angle between laser beams
δ^*	boundary layer displacement thickness
$\Delta\varphi$	phase difference between two signals

Δt_i	time between data points in LDV signal
$\Delta\tau$	time shift in cross correlation calculation
θ	boundary or shear layer momentum thickness
λ	wave length of perturbations
λ_a	acoustic wave length
ρ	fluid density
τ_{xy}	viscous shear stress
φ	overall phase difference between two corners
ω	Doppler frequency
$(\,)_0$	upstream condition
$(\,)_{min}$	minimum value
$(\,)_{max}$	maximum value
$\overline{(\,)}$	time average or mean value
$(\,)'$	fluctuation about the mean
$\overline{(\,)}'$	rms value
$\underline{(\,)}$	vector quantity
$(\,)_e$	free stream condition outside the upstream boundary layer

Chapter 1

Introduction

1.1. Background

Cavity flow phenomena occur in a variety of structures; slots between movable parts of control surfaces of aircraft; ships; tandem arrangements of bluff bodies such as adjacent tall buildings or tractor-trailer combinations, gas dynamic lasers; hydraulic gates; and control valves. The presence of cavities can give rise to drastic changes in the steady and unsteady loading character of these structures. The flow past cavity-type geometries (cut-outs) may introduce large amplitude velocity and pressure fluctuations in and around the cavity which are often damaging to the structures. Flow oscillation over gaps between insulation tiles used on the space shuttle outer surface, caused by evaporation of the filler material at reentry, is suspected of being responsible for the loss of a portion of the tiles. Emission of acoustical noise is another unwanted aspect of cavity flow type oscillation. On the other hand, flow over cavities can be effectively utilized to alter heat transfer (White 1971) and drag characteristics of aerodynamic configurations (Koenig 1978).

Charwat, et al. (1961) categorized cavity flows into open or closed types; "open" when the separated shear layer spans the gap while "closed" refers to flows where the separated shear layer reattaches on the bottom of the cavity and separates again ahead of the downstream corner. For supersonic speeds and for subsonic speeds with turbulent boundary layers, closed cavities are found to have a width-to-depth b/h ratio of more than 11 (Charwart, et al. 1961). Sarohia (1975) shows a demarcation line between an open and closed cavity to be around $b/h \approx 7\text{–}8$ for low subsonic speeds with laminar upstream

boundary layers. Furthermore, open cavity flows are divided into shallow and deep cavities, depending on the type of acoustic resonance present in the flow. When an acoustic resonance is present in the flow, the standing acoustic wave is oriented longitudinally for shallow cavities ($b/h > 1$). The standing wave is of transverse type for deep cavities ($b/h < 1$) (Charwat et al., 1961, Plumblee et al., 1962, East 1966, Tam and Block 1978). Such a definition for the shallow and deep cavities loses its meaning in the absence of the acoustic resonance in the cavity. Tani et al., (1961) define cavity flows as deep and shallow cavities based on their respective low and high pressure drag values. The demarcation line based on Tani's definition is about $b/h \approx 1.4$.

Sketch 1 illustrates the physically significant parameters of the cavity flow.

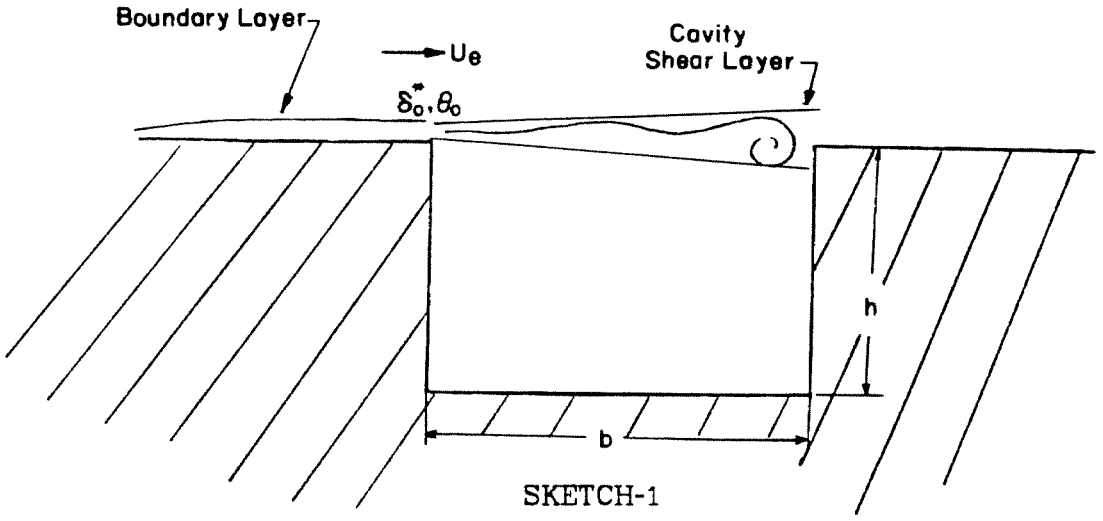

SKETCH-1

where U_e is the upstream edge velocity outside the boundary layer, δ^*_0 is the displacement thickness and θ_0 is momentum thickness. For fixed flow parameters (U_e, θ_0, δ^*_0), cavity flow shows a strong oscillation of the shear layer when the width b exceeds a critical minimum width, b_{min}, (Karamcheti 1956, Sarohia 1975, Rockwell and Naudascher 1978). The existence of this minimum

width for the onset of oscillation is linked to the nature of the instability growth in the shear layer. Previous investigators noticed that the main driving force of the acoustic resonance condition in the cavity was the amplification of instabilities by the respective cavity shear layer. In the shear layers, the final growth and saturation of the instability waves result in roll-up of the shear layer and appearance of large vortical structures (Brown and Roshko 1974). The velocity fluctuation associated with the cavity flow oscillations can be attributed to the presence of these large vortical structures (Sarohia 1975, Rockwell and Knisely 1979). In his study of the frequency selection process, Sarohia (1975) concluded that the frequency at which the cavity chooses to oscillate is such that:

(1) certain phase criteria necessary for the
self-sustainment of the flow are satisfied; and

(2) maximum integrated amplification through
the cavity shear layer occurs.

The cavity flow oscillation was described as a self-sustained type. Rockwell and Naudascher (1978) suggest the following chain of events to be responsible for the self-sustaining nature of the oscillation: impingement of organized vortical structures upon the downstream corner; resultant upstream influence (interpreted as Biot-Savart induction); reception and conversion of this upstream influence into velocity perturbation by the sensitive region of the shear layer close to the upstream corner; amplification of these fluctuations by the shear layer; growth into vortex structures. Consideration of the acoustic speed becomes important in the nature of the upstream propagating waves for high Mach number flows or when the impingement length, b, is of the same order of magnitude as the acoustic wave length ($b \approx \lambda a$) (Heller and Bliss 1975, Rossiter 1964, and Rockwell and Naudascher 1978).

The self-sustained nature of the cavity flow oscillation is similar to that of the jet-edge oscillation (edge tone phenomenon). Self-sustained oscillation of cavity flow has the following properties:

(1) for a fixed cavity depth and fixed flow parameters ($U_e, \theta_0, \delta_0^*$) there exists a minimum width (b_{min}) below which no oscillation occurs;

(2) for fixed cavity depth (h) and fixed boundary layer thickness there exists a minimum Mach number or free stream velocity (U_e) below which no oscillation occur ;

(3) for $b > b_{min}$ *or* $U_e > U_{e_{min}}$ and fixed boundary layer thickness the frequency of oscillation decreases as the parameter $\frac{U_e}{b}$ decreases.

At certain values of $\frac{U_e}{b}$, the frequency undergoes a jump to a higher mode of oscillation with a corresponding higher frequency. Hysteresis is observed in the transition region. In the new mode, frequency also decreases as $\frac{U_e}{b}$ decreases. Sarohia (1975) has found that for a fixed value of U_e, b, and h, there exists a maximum boundary layer thickness $\left[\theta_{0_{max}} \text{ or } \delta_{0_{max}}^*\right]$ above which no oscillation occurs.

The ladder-type behavior of frequency versus $\frac{U_e}{b}$ (which has the dimension of frequency) is remarkably similar for self-sustained flows and externally forced free shear layers (Ho and Huang 1982). However there is a significant difference between the nature of perturbations introduced at the sensitive region of the shear layer by the downstream corner and that of an external forcing source. External forcing subjects the shear layer to a constant amplitude perturbation at one frequency. But flows excited by the impingement of

the shear layer at the corner are subjected to variation in strength of events at the corner (Knisely 1980). Often this variation gives rise to the amplitude modulation of the fluctuations which appears as low frequency component in the spectrum of fluctuations. Knisely (1980) shows that transverse positioning of the successive vortices as they approach the downstream corner result in varying degree of severing of incident structures. It is not clear what sort of mechanism is responsible for the presence of these low frequencies in the cavity shear layer. Also, the precise role of the downstream corner as a source of external forcing for the shear layer and generation of different frequency components of oscillation is not fully understood.

As mentioned before, the presence of cavities (gaps) can be used effectively to change the drag characteristics of bluff bodies. A novel experiment by Koenig and Roshko (1978) demonstrated that by properly choosing dimensions, a gap generated by placing a disk in front of a circular cylinder can drastically reduce the drag coefficient of the system. A similar observation for different configurations of bluff bodies in tandem was made by Mair (1965) and Zdravkovich (1977). It is not clear into which category these types of cavity flows oscillations fall. Scattered information about the frequency of the shear layer oscillation shows behavior characteristic of self-sustained flow for the low drag cases of flow over gaps generated by bluff bodies in tandem.

1.2. Statement of the Problem

A large portion of cavity flow investigations are devoted to the study of instability aspects of this problem. Quite independently, a second group of studies can be found which deal only with the pressure field and drag characteristics of this flow (Roshko 1955, Tani 1961, Fox 1964, Koenig 1978). To our knowledge no investigator has tried to fill the gap between the first and the second group of experiments. It was this gap that motivated the present investigation into the

role of instabilities in drag and pressure field formation of cavities.

Another important aspect of cavity flow study is to develop a technique to control the frequency and amplitude of oscillations. Previous work involving control of the cavity flow oscillation has dealt with changing the geometry of the downstream or upstream corner of the cavity by rounding the corners (Ethembabaoglu 1973) or by placement of external objects in the cavity such as flaps, deflectors or perforated plates (Heller and Bliss 1975 and Ball 1957). Usually these devices introduce their own complexities into the problem. There was a need for a clean technique that can control the oscillations by purely introducing external perturbation to the shear layer.

The following were objectives set for the present investigation.

(1) To understand the relation between the state of the shear layer and the drag of the cavity.

(2) To determine the influence of initial conditions on the onset of self-sustained oscillation and to obtain a better understanding of the feed-back mechanism.

(3) To develop and use a technique which is capable of controlling (enhancing or damping) established oscillations.

1.3. Approach

The connection between the state of the shear layer and the drag of the cavity system can be made by studying the quantities that are responsible for the transfer of the momentum in and out of the cavity ($\overline{u'v'}$ and $\overline{uv}$). These quantities carry the necessary information about the nature of the instabilities in the shear layer and play an inherent role in the formation of the pressure distribution inside the cavity system. Thus, accurate measurements of these quantities

for different width-to-height ratios (b/h) in conjunction with the pressure distribution measurements would provide the necessary information for fulfilling the first objective. External forcing by strip heating was used to study the feedback mechanism and control of cavity flow oscillation thus, fulfilling the second and third objectives.

Chapter 2

EXPERIMENTAL DETAILS

2.1. Water Channel

The experiments were performed in a newly constructed free surface water tunnel, which is located at the Jet Propulsion Laboratory, California Institute of Technology. This tunnel is specially designed to attain a low turbulence level for the purpose of carrying out sensitive instability type experiments. The essential features of the free surface tunnel are shown in figure 1. Water is recirculated in a closed loop by a 50 horsepower axial flow pump, located 5m below the free surface, in the lower leg of the tunnel. The desired flow speeds are achieved by throttling flow through an on-line and a by-pass valve. The upper portion of the tunnel consists of a diffuser, a straight wall section comprised of flow manipulators and a test section. The high speed flow from the pump is then diffused by the 22° half angle diffuser. In order to prevent severe flow separation, the effect of an unfavorable pressure gradient is reduced by matched pressure drops of three perforated plates installed in the diffuser section. Before entering the test section, the flow passes through different flow manipulators and a final 4:1 fifth order polynomial contraction. Each manipulator and contraction is designed to break up and suppress different scales of the turbulence.

The test section is 45.7 cm (18 inches) wide and 63.5 cm (25 inches) deep. The wetted depth can be increased up to 56 cm (22 inches). The test section is bounded by glass windows on sides, bottom and top to permit visual and optical study of the flow throughout its 1.83 m (6 feet) length.

The existing arrangement made it possible to achieve a maximum velocity of 1 m/sec in the test section. Turbulence levels and velocity profiles at 20 cm from the entrance to the test section and outside of the wall's boundary layer were obtained using hot film probes and an LDV system. The uniformity of the flow within a square area (30 cm x 30 cm) centered at the center of the test section was below 1% of the center line mean velocity. The free stream turbulence level at 25 cm/sec on the centerline was near .05%. The power spectrum of freestream velocity fluctuations, a sample of which is shown in figure 2a, indicates most of the energy was concentrated at frequencies below .5 Hz, which is primarily below the range of frequencies of interest in this study, 2 to 10 Hz (figure 2).

2.2. Model

An axisymmetric model, constructed of anodized aluminum and Plexiglas, was used throughout the investigation. The model was composed of a rear portion and a front portion which were connected by a sting as shown schematically in figure 3. The rear portion, a hollow cylinder 10.16 cm (4 inches) in diameter and 91.4 cm (36 inches) in length, was connected by a strut to a traversing mechanism which was installed on top of the test section. This allowed for movement of the model up and down and also along the test section axis. The front portion consisted of a half portion 2:1 ellipsoidal cone with a 10.16 cm (4 inch) minor diameter. The ellipsoidal cone was extended in the downstream direction by a straight section which also was 10.16 cm (4 inches) in diameter and 5.08 cm (2 inches) in length.

The sting was made from a 1.27 cm (1/2 inch) O.D. thick wall stainless steel tube. Twelve brass tubes were installed inside of its walls to carry pressure signals from the front nose while the interior of the sting was devoted to dye tubes and electrical wires for the strip heaters. The front end of the sting was fixed to

the inside wall of the front nose while the rear end was connected to a vertical rod by means of a 90° gearing mechanism. The vertical rod was then brought out of the model through the strut. By manual rotation of the vertical rod, the sting could be moved longitudinally relative to the rear portion of the model. With the aid of this mechanism, plus a dial and a helipot at the end of the vertical rod, it was possible to change and read the cavity length. The solid inner faces of the cavity were equipped with 14 pressure taps on the downstream face and 8 pressure taps on the upstream face. The diameter of each tap opening was .1 cm (.041 inch).

2.3. Pressure Measurements

The low velocities in the range of interest introduced the well known difficulty of measuring low differential pressures under high head. A free stream velocity of 25 cm/sec generated a dynamic head of .38 cm (.15 inch) of water, while a typical value of total head at the point where the pressure transducer was located was 63.5 cm (25 inches) of water. Further, since differential pressures inside the cavity are much smaller than for a free stream dynamic head, the demand on the pressure measuring system for high resolution and repeatability is very severe.

Another common problem in pressure measurements with water as a medium arises from the presence of air bubbles in the system, which may cause erroneous pressure readings. The following approach was taken to solve the air bubble problem and to achieve high resolution. Each line, Tygon tube ID = .16 cm (1/16 inch), from the model pressure taps or from the pitot-static probe was connected to a common drain through a toggle valve (figure 4). Each line then extended and manifolded into a 24 port fast switch (Scanivalve type W2460). The common end of the Scanivalve was connected to the low pressure side of a pressure transducer (Validyne type Wet-Wet DP-103-12) which was able to

measure differential pressures in the range of 0 to .762 cm (.3 inch) of water with a resolution of 1% of the total range. The high pressure side of the transducer was connected to the total pressure tube in the test section, which was chosen as the reference. The common drain was connected to a vacuum line and was used as a sink into which air bubbles could rise. Also, it was used to fill the lines from the model to the toggle valves. A special calibration tank was designed to provide a differential head of 0 to 10.16 cm (4 inch) of water with a resolution of .00254 cm (.001 inch) of water. One port of the Scanivalve was devoted to the low head side of the calibration tank, while the higher head side was connected to the high pressure side of the transducer through a 3-way valve. A schematic of the pressure sensing system is given in figure 4. The average height of the calibration tank was set close to that of the free surface. This was done to prevent overpressurizing the transducer during switching. Table 1 gives different operational positions of the valves. The pressure measurement process was automated by using a HP data logger. A proper software program was written for the data logger in order to actuate the Scanivalve and to digitize the analog signal from the transducer. Prior to each run the digitization rate, the lag time between each point, and the averaging time were specified to the machine. After each run, the program stored the pressure distributions, and the calculated drag coefficient as well as other parameters of each run on a floppy disc.

2.4. Frequency, Phase and Corrolation Measurement

Velocity fluctuation measurements were made with a TSI hot film probe (1277-10A) using a TSI 1050C anemometer in conjunction with a TSI true rms meter (1076). The output of the hot film anemometer was fed to a digital power spectrum analyzer (SL20). A bandwidth of .1 Hz was used for locating and distinguishing frequency content of the velocity signals on line. A hard copy of the spectrum was obtained by either taking pictures of the spectrum analyzer

screen or by plotting the spectrum on an x-y plotter (HP model 7001A).

For phase angle and cross correlation measurements a second hot-film probe was mounted on a traversing mechanism which was able to traverse the entire width of the cavity. Throughout this experiment the first probe was used as a reference probe. This probe was placed above the upstream corner at x = b and $y_{.95}$, the latter being the y-location of $\bar{u}/U_e = .95$. Phase measurements were made by moving the second probe relative to the reference probe along the edge of the shear layer where $U/U_e = .95$ ($y = y_{.95}$). The signals from the reference and the second probe were fed to a digital probability and correlation analyzer (SAICOR 43A). Throughout the phase angle or cross correlation measurements a sampling rate of 200 per second, limited by 400 samples and a corresponding Nyquist frequency of about 30, was used. Again a hard copy of the output was obtained on an x-y plotter. See Appendix A for the details of phase angle measurement.

2.5. Velocity Measurements by Laser Doppler Velocimetry

Due to sensitivity of the cavity flow oscillations to the presence of external objects in the flow, hot-film anemometry is not suitable for velocity measurements. Severe interference of the probes with cavity flow mode switching is observed in the present study. Existence of large regions of reversed flow is another reason for making hot-film anemometry unappealing for this flow. The only instrument currently available to measure velocity field non-intrusively and unambiguously in such a flow condition is the laser Doppler velocimeter (LDV). Other useful properties of the LDV include the small sampling volume, high frequency response and linearity of the instrument. In this study, the velocity field of the cavity flow was measured by a two-component, two-color, frequency shifted laser Doppler velocimeter (TSI 9100-7 system). It is a dual beam (forward) scatter configuration and processor, which was operated in single-burst

mode. The LDV processor operated in conjunction with a minicomputer system (PDP-11), which was also used for processing the results. A forward scatter configuration was used in these experiments, with the transmitting and receiving optics located at the bottom and top side of the facility as shown in figure 5.

The physical arrangement of the LDV optics relative to the facility and information regarding focal volume are given in figure 6 and table 2. The transmitting and receiving optics are mounted on an optical table with their optical axes perpendicular to the flow direction. The focal volume has its longitudinal axis in the z direction of the facility. The streamwise velocity component is measured by the fringe system formed in the z-x plane of the tunnel while velocity components perpendicular to the mean free stream are measured by the fringe system formed in the z-y plane of the channel. The velocity bias technique (Bragg cell) is used to detect velocity reversals. For details of the optical setup and Bragg shifting see Appendix B and C respectively.

The focal volume can be moved within the test section by means of remotely operated stepping motors. Motion on a fixed horizontal plane was obtained by a corresponding motion of the optical table. Motion along the z-axis resulted from the displacement of the focussing lens and receiving optics along their optical axis. The table position was controlled to a resolution better than 100 μm.

2.5.1. *Signal Processor and Data Acquisition.* The measurement of the velocity can be obtained only after suitable processing of the outputs of the photomultiplier tubes. Two counter processors were used, one for each velocity component. They were operated in the single-burst mode, for which only one particle is present in the focal volume when the measurement is made. In addition, the system was operated in coincident mode, in which the output of the processors is tested for coincidence in time so that the two components of the velocity vector as determined by the optical set-up are measured on the same

particle.

The signal processing is accomplished in four stages: analog processing, burst processing, coincidence test and transfer to the computer. The analog processing involves suitable filtering and amplification of the signal for optimum signal to noise ratio. Only low pass filters were used. A built-in filter in the Bragg cell circuitry removes pedestal noise (low frequencies). The low pass filter is used for removal of high frequency noise. Cut-off values from 30 KHz to 100 KHz were used, depending on flow velocity. The output of the filter is processed by an amplifier. In the present experiments the gain was set at 2 or 4 depending on the condition of the signal. A detailed description of the valid burst processing is given in Appendix D.

2.5.2. *Operating Conditions.* A typical signal to noise ratio, as observed from high sampling rate measurements in a quiescent fluid, was in excess of 100. An equivalent background noise level of .4% and .6% was detected for the streamwise and the transverse velocity fluctuations respectively. When the signals from two channels were correlated for the purpose of shear stress measurement, the corresponding noise level for $\sqrt{\frac{\overline{u'v'}}{U_e^2}}$ measurements was .07%. The better noise level value was due to the fact that much of the uncorrelated noise from two independent processors was eliminated during the correlation process, resulting in an extremely low noise level for shear stress measurement.

A time window of 50 μsec was used in all velocity measurements. The amplitude threshold level and the gain of the amplifier were adjusted to maintain the data rate between 60 to 200 particles/sec, which corresponds to a minimum Nyquist frequency of 10. It was found under the present experimental conditions that particles less than 15 μm had sufficient response frequency. Thus for the purpose of LDV measurements, particles larger than 15 μm were filtered

from the water.

2.5.3. *Operating Procedures.* Prior to every experimental run with the LDV system, a variety of tests were conducted to verify adequate operation of the system, e.g., the transmitting optics alignment and overlapping of the green and blue focal volumes. The alignment of the receiving optics was verified with the facility in operation. Adjustment of the location of the pin-hole and photomultiplier assembly was often necessary for maximum data acquisition rate at the operating conditions of the water channel.

After the high-pass and low-pass filters were set to their predetermined values, the gain of the amplifier stage was adjusted for optimum signal to noise ratio. After these tests were completed, the actual measurements were initiated. A 16,000 word buffer was obtained at every point. The data were stored temporarily on disk. At the end of the test run, all the data were transferred to a magnetic tape for permanent storage and processing at a later time. The size of the data buffer combined with the data rate to give a total sampling time between 15 to 60 sec. This sampling time was considered adequate to properly characterize mean turbulent quantities.

2.5.4. *Data Processing.* The velocity data generated by the data acquisition programs was processed using the minicomputer system. Processing involved several steps, e.g., error detection, computation of flow characteristics in the frame of reference of the optics, transformation of those quantities to the physical frame of reference, and the computation of integral quantities in the physical reference frame.

There was one condition that could have lead to a significant error in the measurements. This condition arises from transmission line noise, resulting in a spurious data word being included in the stream of data as it is transferred to

the computer. Because catastrophic effects could result from this condition, the data processing programs had to verify that the data were in the correct order. If an error were detected, the data point would be discarded. Less than 1% of the data was removed by this test. At every measurement point, a frequency histogram was constructed for each channel. This histogram provided information about the proper operation of the system; i.e., filter setting, and the electronic noise.

The Doppler frequency and the time between data points were utilized to calculate the flow velocity using the appropriate Doppler constant. The mean, second moment and cross-correlation between the two velocity components were evaluated. For a detailed description of the expressions used for the data processing see Appendix E.

2.6. Flow Visualization

The model was equipped with two dye injection tubes whose axes each made an angle of 1 ° with local curvature of the nose cone at the point of the injection. The injection points were 2.54 cm (1 inch) off the stagnation point. Two visualization techniques were employed in this study. In both cases, diluted coloring dye or fluorescein dye was gravity fed to the injection tubes and then discharged into the boundary layer over the cavity.

In the first method, using blue dye, a uniform background illumination was provided specifically for photographic purposes. In the second technique fluorescein dye was used and excited by a laser sheet. The laser sheet was obtained from a 2-watt argon-ion laser with a thickness less than 1mm. The technique was used first by Dewey (1976). Photographs of the resulting flow patterns were made using a 35 mm SLR camera with a focal length F3.6 lens at shutter speed 2 to 1/1000 sec and either TRI-X black and white print film or high speed Ektachrome tungsten color slide film.

2.7. Operational Procedures, Accuracies and Flow Parameters

The pressure and velocity measurements procedure was as follows. Prior to each run with the tunnel running at idle, the nullity of the pressure readings was checked. The desired speed of the tunnel was set. The tunnel speed, extracted from the dynamic pressure measurement, was checked against the one measured by laser Doppler velocimeter. The cavity gap was set to the desired width and the frequency of cavity flow oscillation was checked. Depending on the degree of the flow unsteadiness, the pressure averaging time was set from 30 to 120 seconds. The alignment of the model was checked by pressure reading differences of taps on the four sides of the downstream face. A cross check of the model alignment was made through flow visualization.

At the end of a test run, with the tunnel again set at idle, the tap pressures were checked to insure they had returned to zero. For velocity field measurements, the measuring volume was fixed at a reference point on the model. This was done by observing the position of measuring volume with respect to the model through the eyepiece on the receiving side of the LDV. Measurements were made at speeds covering the range of 16 to 27 cm/sec. The corresponding Reynolds number, Re, based on the model diameter, d = 10.16 cm (4 inches) and at $U_e = 23 cm/sec$ was 24×10^{-3} . Most of the pressure data points were measured at least twice and at some points up to 5 times. The repeatability of the calculated drag coefficient was about 4% of the average value.

2.8. Reference Quantities

Throughout the experiment, the origin of the reference co-ordinate system was located at the upstream corner. The x and y axes lie in the symmetry plane. The x-axis was in the direction of flow; the y-axis was measured positive outward with respect to the center of the cavity. The components of velocity vector in the direction of x and y axes were denoted u and v.

The cavity width, b, was non-dimensionalized by normalizing it with respect to θ_0, the momentum thickness of the upstream boundary layer at the point of separation. Momentum thickness for the shear layer is defined as

$$\theta = \int_{-\infty}^{+\infty} \frac{U}{U_e}\left(1 - \frac{U}{U_e}\right)dy \qquad (2.1)$$

where U_e is the free stream velocity on the outside edge of the boundary layer at the point of separation. Using U_e instead of U_∞, the free stream velocity in front of the model nose eliminated the need for the blockage correction. This also made the results independent of the front nose shape (provided there existed no substantial pressure gradient over the length of the cavity).

The boundary layer upstream of the cavity was considered laminar at $U_e = 23cm/sec$ and had a shape factor of $H = \frac{\delta^*}{\theta_0} = 2.5$ where $\delta^* = .1cm$ (displacement thickness), $\theta_0 = 0.041cm$ and $Re_{\theta_0} = 95$. For the shear layer, the transverse distance y was non-dimensionalized as $\frac{\left(y - y_{.5}\right)}{\theta}$, where $y_{.5}$ is the location of the non-dimensional velocity $\frac{\overline{u}}{U_e}$ with a value of .5, and θ is the local momentum thickness of the shear layer as defined by equation (2.1). The radius of the axisymmetric cavity, which is 5.08 cm (2 inches) was used to normalize the radial distance of pressure taps (r) on the inner surfaces of the cavity. All drag forces were normalized by $\frac{1}{2}\rho U_e^2 A$, where ρ is water density and A is the cross- sectional area of the model.

Chapter 3

Flow Documentation

The measurements of various parameters relevant to the cavity oscillations reported in this chapter are not all novel, some of them having been reported in references cited above and in others. The purpose here was to provide a solid reference condition for the measurements to be described in Chapters 4 and 5. Nevertheless, some new definitions and clarifications and features are introduced.

3.1. Cavity Flow Oscillations as a Function of b/θ_0

It is known [Karamcheti (1956), Sarohia (1975), Rockwell and Naudascher (1979)] that shear layers over cavities undergo transition from a steady layer to an unsteady layer at a critical dimensionless width $b/\theta_0|_{min}$. For $b/\theta_0 < b/\theta_0|_{min}$, the shear layer bridges smoothly over the cavity with no distinct oscillation in it. The onset of unsteadiness is always associated with the presence of a distinct fundamental frequency, which is amplified by the shear layer. In this study, the fundamental frequency is identified as the one that has the highest peak in the power spectrum of the velocity fluctuations. Velocity fluctuations were measured at $x = b$ and $y = y_{.95}$,($y_{.95}$ being the locus of $\frac{\overline{u}}{U_e} = .95$) throughout the frequency measurements.

Figure 7 presents the variation of fundamental frequency, F, with b/θ_0 at a fixed edge velocity ($U_e = 23 cm/sec$). Oscillation starts at $b/\theta_0 \approx 81$ which represents the minimum cavity width $b/\theta_0|_{min}$, for the present experimental condition. The fundamental frequency of oscillation decreases as b/θ_0 increases. This course of frequency variation is interrupted by a sudden jump

of frequency from F = 4.6 to 6.2 Hz. This new frequency initiates another course of decreasing frequency as b/θ_0 is further increased. A non-dimensional frequency can be defined for these two modes of oscillation as $\frac{Fb}{U_e}$ (Strouhal Number). This Strouhal Number has a value of $\approx$ 1 over the entire range of the starting mode then, jumps to a value of $\approx$ 1.5 which it maintains over the next mode. According to Sarohia (1975) and Rockwell and Knisely (1980) these two modes correspond to Modes II and III of the cavity flow oscillation.

A sequence of power spectra of the velocity fluctuations as a function of b/θ_0 is shown in figure 8. Several features of these spectra are noteworthy. First is the presence of peaks both at 4.6 Hz and 6.2 Hz during the transition region between the modes. From these average power spectra it is not possible to determine whether the two frequencies alternate intermittently or whether both co-exist simultaneously. To clarify this matter, figure 9 shows three oscilloscope traces of the velocity fluctuations in Mode II, in the transitional region, and in Mode III of the oscillations, respectively.

Figure 9b confirms the coexistence of two frequencies by showing a strong modulated trace of the signal. A region of hysteresis, as shown in figure 7, is associated with the transition region. Presence of frequencies lower than fundamental is a prominent feature of Mode III (figure 8c). Such low frequencies have been observed by Knisely (1980) and were shown to be associated with the interaction of successive shear layer vortices with the down stream corner. A possible explanation for the existence of such a low frequency is given in the flow model section (Section 4.10). End of Mode III is marked by a loss of coherence in the oscillation and the disappearance of the fundamental frequency. At this stage, ($b/\theta > 160$) , cavity flow begins to exhibit bluff body wake behavior, and a distinct frequency for this regime cannot be detected.

3.2. Phase Measurements

Information about the overall phase difference between fluctuations at the upstream corner (x = 0) and the downstream corner (x = b), is needed for improving our understanding of the cavity flow oscillation. This is the subject of the following discussion.

The existence of a strong phase gradient across laminar and turbulent shear layers is well known [Freymuth (1966), Sarohia (1975), Elder (1978), Ziada and Rockwell (1981), and Hussain (1981)]. This gradient can be well approximated by inviscid theory, (Michalke, 1965), except for regions close to the downstream corner. Existence of such a phase gradient introduces difficulties in choosing a proper criterion to define an overall phase difference between the two corners of the cavity. Knisely (1980), Ziada and Rockwell (1981), Rockwell and Schachenmann (1982), in their effort to define an overall phase difference for different types of self-sustaining flows, concluded that tracking values of phase along the edge of the shear layer ($\overline{u}/U_e = .95$) will result in an overall phase difference of $\sim 2N\pi$. In contrast, other criteria e.g., following one of the disturbance amplitude maxima within the shear layer, yield different overall phase difference for different geometries of self-sustaining flows.

In the present study, phase measurements were obtained by following the outer edge of the shear layer along the locus of $\overline{u}/U_e = .95$. The reference probe was located at x = b, $y = y_{.95}$, while the second probe was moved along $y_{.95}$ of the shear layer. Before each set of measurements were to be taken, the auto correlation of the reference signal with respect to itself or to that of the second probe (cross-correlation) was obtained. In this way, any initial phase difference due to circumferential or longitudinal distances between two probes was detected. A sample of such a measurement is given in figure 10. For the case of $b/\theta_0 = 85$, and $U_e = 23 cm/sec$ a typical phase angle distribution of the velocity

fluctuations as a function of x/θ_0 is presented in figure 11. The cavity shear layer has a fundamental frequency of 5.9 Hz with corresponding $\frac{Fb}{U_e} = 1$ which identifies it as the second mode of oscillations. Figure 11 depicts an overall phase difference of 4π between two corners of the cavity. Similar measurements to determine the overall phase difference between the two corners were carried out for the entire range of Modes II and III of cavity flow oscillation. Figure 12 represents the distribution of the overall phase difference as a function of b/θ_0. It is important to note that the cavity flow retains a 4π phase difference during Mode II, while having a 6π phase difference during Mode III. This fact suggests that overall phase difference between the two corners be formulated as

$$\frac{\varphi}{2\pi} = N \tag{3.1}$$

where N represents the mode of the cavity flow oscillation. Using the relation $U_c = F\lambda$, where U_c is the convection velocity (phase velocity) of the fundamental frequency of oscillation and λ is the wave length, equation 3.1 can be rearranged as

$$\frac{\varphi}{2\pi} = \frac{b}{\lambda} = \frac{Fb}{U_c} \tag{3.2}$$

Equation 3.2 indicates that cavity during Mode II contains two wave lengths of the fundamental frequency, while Mode III contains three wave lengths. Also, emergence of the Strouhal number based on the phase velocity in equation 3.2, directs us to define the mode of the oscillations based on $\frac{Fb}{U_c} = N$ rather than $\frac{Fb}{U_c} = \frac{N}{2}$. This convention defines each mode by the number of wave lengths that it contains and establishes a relation between the mode's name and the

corresponding Strouhal number.

It is important to note that close to the transition region, an important phase deviation from $\frac{\varphi}{2\pi} \approx 2$ occurs (figure 12). Such a deviation of overall phase difference also was observed by Rockwell and Schachenmann (1982) for impinging turbulent jets at low Mach numbers.

3.3. Overall Features of Cavity Flow Regimes

3.3.1. *Non-oscillating Cavity Flow.* The non-oscillating regime of the cavity flow is marked by a fairly steady and weak vortex stationed inside of the cavity. Unsteady mass transfer in and out of the cavity is minimal due to lack of any substantial oscillations in the shear layer. Figure 13 presents flow visualization of the cavity flow in this regime. Often, color dye trapped in the cavity remained there for a long time. The effect of the cavity presence on the outer flow field is minimal. Branching of the shear layer at the downstream corner is another feature of this mode observed in flow visualization studies. It should be mentioned that for $b/\theta_0 < b/\theta_0|_{min}$ hot-film signals indicated the presence of weak periodic fluctuations in the shear layer. Due to lack of long enough cavity width, these perturbations do not amplify enough to make the flow self-sustained. This matter will be discussed in more detail in Chapter 5.

3.3.2. *Self-Sustaining Cavity Flow.* The definition of self-sustaining flow and the description of the chain of events that result in flow self-sustainment is given in the introduction. As mentioned before, natural cavity flow oscillation is by definition self-sustaining.

3.3.2.1 *General Characteristics of the Self-sustaining Modes..* A self-sustaining oscillation appears in the cavity when b/θ_0 reaches $b/\theta_0|_{min}$. The wave length of the fundamental frequency scales itself with the width of the cavity (figure 12). Flow in this regime is stable. Even severe attempts to perturb the course of oscillations is resisted, depending on the strength of the self-sustainment. In this study, the most stable case is defined as the one that generates the highest level of organized fluctuations for given b/θ_0.

Overall phase difference between the two corners of the cavity satisfies the relation $\frac{\varphi}{2\pi} = \frac{b}{\lambda} = \frac{Fb}{U_c} = N$, where N is the number of wave lengths contained by the cavity width during Nth mode of oscillations. Shown in figure 14 are flow visualizations of Modes II and III of the cavity flow oscillations. In the present study, the cavity always started the oscillation with Mode II, omitting the first mode $\frac{Fb}{U_c} \approx 1$. Sarohia (1975) observed similar omission of the first mode in his study of cavity flow for some freestream velocities.

Instantaneous flow visualization pictures (figure 14) show that the wave amplitude grows as it approaches the downstream corner. This growth, which is exponential according to the linear theory, results in a vortex roll up. This roll up is very similar to that observed by Brown and Roshko (1974), Winant and Browand (1974) in the free shear layer. Mode III shows, usually, two complete roll ups of the shear layer. Unlike the case in a free shear layer, no vortex pairing is observed during the cavity self-sustaining modes. Thus, presence of low frequency peaks in the power spectra of Mode III of the present study cannot be associated with vortex coalescence.

Presence of a strong stable vortex is another characterstic of the self-sustaining mode.

3.3.2.2 *Similarity to Externally Forced Free Shear Layers*.. The ladder-like variation of cavity shear layer frequency shows striking resemblance to the externally forced free shear layers (Miksad 1973, Ho and Huang 1982). One can imagine that the downstream corner plays the role of external forcing source. Also the term b/U_c can be assumed to be equivalent to the forcing frequency in an externally forced free shear layer experiment. Figure 15 shows the variations of the fundamental cavity shear layer frequency as a function of b/U_c. In this figure, several cases of the cavity flow geometries and velocities fall on the corresponding mode lines of externally forced experiments. In general, one must treat this resemblance with caution, because at high subsonic or supersonic cavity flows, the wave length will not scale with cavity width b. As suggested by Laufer and Monkowits (1980) such a scaling should follow the more complicated feed back equation

$$\frac{Fb}{U_c} + \frac{Fb}{C} = N \tag{3.3}$$

where C is the sound velocity. In the subsonic case $C >> U_c$, equation (3.3) reduces to our familiar relation for the Strouhal number $\frac{Fb}{U_c} = N$.

3.3.3. *Wake Mode of Cavity Flow.* The last Mode (III) of oscillations, observed in this study, shows strong intermittency as the cavity width is increased. It seems that eventually an intermittency overcomes the coherent oscillation and the feedback mechanism becomes ineffective. The flow visualization studies revealed that when the self-sustaining regime ends, the shear layer no longer reattaches onto the downstream corner. The cavity flow becomes semi-periodically unstable in a larger scale, comparable to the scale of the model (figure 16a, b). Time averaged flow visualization (figure 16c) shows that the mean flow reattaches below the downstream corner. Instantaneous flow

visualization indicates that the flow is highly asymmetrical (figure 16a). The flow field in this regime shows some resemblance to a three-dimensional bluff body wake (Werle 1974), even though the presence of the rear body is still strongly being felt by the wake of the front body. A detailed exploration of the flow for cavity-diameters ratio $b/R > 1.65$ was not carried out.

3.4. Mean Velocity Distributions in the Shear Layer

For three values of cavity width $b/\theta_0 = 85$, $b/\theta_0 = 103$ and $b/\theta_0 = 130$, mean velocity profiles were obtained at a number of streamwise stations. Edge velocity (U_e) was fixed at 23 cm/sec. The cavity width $b/\theta_0 = 85$ marks the beginning region of Mode II $\left[\frac{Fb}{U_c} \approx 2\right]$, while the cavity width $b/\theta_0 = 103$ marks the middle of the same mode. For $b/\theta_0 = 130$ $\left[\frac{Fb}{U_c} \approx 3\right]$, the cavity was oscillating in Mode III. Figure 17 presents nondimensionalized mean velocity profiles at selected downstream stations for $b/\theta_0 = 85$. As shown in figure 17, in the early stages of the shear layer growth, the velocity profile changes from a boundary layer profile to a shear layer profile. Free-shear-layer similarity in the $\frac{\bar{u}}{U_e}$ profiles is attained for $b/\theta_0 \geq 30$. In figures 18 and 19, which present nondimensionalized mean velocity profiles for $b/\theta_0 = 103$ and $b/\theta_0 = 130$, respectively, self-similarity in the $\frac{\bar{u}}{U_e}$ profiles is also observed.

Figures 20 through 22 present the nondimensionalized mean transverse component of the velocity, $\frac{\bar{v}}{U_e}$, in the shear layer. These figures reveal that unlike the $\frac{\bar{u}}{U_e}$ profiles, mean transverse velocity profiles do not scale with the downstream distance. Thus no self-similarity can be found for $\frac{\bar{v}}{U_e}$ profiles. Gorree, Dimotakis and Koochesfahani (1980) were able to show that for free shear

layers with much higher Reynolds number, self-similarity exists for $\frac{\bar{v}}{U_e}$ profiles. The lack of similarity in the $\frac{\bar{v}}{U_e}$ profiles of the cavity shear layers might be due to existance of the strong recirculating flow inside of the cavity. Figure 23 presents the locus of $y_{.5}$ values as a function of $\frac{x}{b}$. As in previous studies of Browand (1966), Sarohia (1975), and Knisely (1980), the $y_{.5}$ values were found initially to lie above the level of the separation edge. Depending on the stage of the cavity flow, the locus of $y_{.5}$ approaches the $y=0$ line as the profile develops. The shear layer shows a stronger deflection into the cavity for the $b/\theta_0 = 103$ than for $b/\theta = 85$.

0.1. Growth Rate of the Shear Layer

For four values of cavity width, $b/\theta_0 = 85$ (Mode II) $b/\theta_0 = 103$ (Mode II), $b/\theta_0 = 119$ (Mode II) and $b/\theta_0 = 135$ (Mode III), the momentum thickness growth of the shear layer is given in figure 24. As in the studies of Sarohia (1975) and Rockwell and Knisely (1980), the momentum thickness is found to grow linearly with x/θ_0. Because of this linear growth, one might assume a self-similarity for the cavity shear layers, but it is interesting to mention that in both the previous studies and the present experiment, the value of the maximum shear stress is not constant (figure 24) as is required for the self-similarity of the free shear layer.

For all cases with $b/\theta_0 \geq 103$, the growth rate is fairly constant $\left[\frac{d\theta}{dx} \approx .031\right]$ and does not experience a sudden change during the mode switching region. It should be noted that the cavity shear layer growth rate is comparable to that of turbulent mixing layers. For $\frac{U_1}{U_2} = 0$, the high Reynolds number shear layer of Liepmann and Laufer (1947) had a growth rate of momentum thickness of 0.035.

0.2. Shear Stress and Velocity Fluctuation Distributions of the Cavity Shear Layer

Measurements of shear stress and fluctuating components of the velocity field are essential to an understanding of the overall nature of the cavity shear layer. As discussed previously, due to the nature of the present LDV measurements, shear stress measurements show fairly low background noise levels. Such an advantage was not available for $\frac{\overline{u'}}{U_e}$ or $\frac{\overline{v'}}{U_e}$ measurements. Figure 25 presents a sample of time traces of the streamwise and transverse velocity fluctuations as well as their respective simultaneous correlation.

Figures 26 through 28 depict the streamwise evolution of the transverse profile of the shear stress for $b/\theta_0 = 85$ (Mode II), $b/\theta_0 = 103$ (Mode II), and $b/\theta = 130$ (III Mode). For large $\frac{x}{\theta_0}$, shear stress profiles tend to show a second peak in the lower portion of the shear layer. Existence of such a second peak has been observed by Freymuth (1966), Knisely (1980); Ziada and Rockwell (1981) showed that it can be predicted by Stuart's (1967) theoretical vortex model. Also important for our consideration is the fact that, even though the mean streamwise velocity profiles scale with $\frac{x}{\theta_0}$, the maximum of the shear stress profiles does not have a constant value as would be required for self-similarity, they show an exponential growth with x/θ_0 (figures 29 and 30). Streamwise growth of the maximum shear stress for several cavity widths is shown in figures 29 and 30. Short cavity cases, $b/\theta_0 = 85$ (Mode II) and $b/\theta_0 = 103$ (Mode II), show a region of exponential growth of the maximum shear stress. For long cavities $b/\theta_0 > 103$, the region of exponential growth is followed by a saturation region. In Mode II, the rate of growth for $\frac{\overline{u'v'}}{U_e^2}\Big|_{max}$ increases as b/θ_0 increases (figure 29). The transition region does not show a noticeable change in the growth rate, but the general level of the shear stress

decreases for the transition region (figure 29).

Figure 30 gives the distribution of maximum shear stress growth for Mode III. This mode, too, shows exponential growth for the maximum shear stress in the shear layer. Again growth rate increases as b/θ_0 increases. It is important to mention that the general level of the maximum shear stress distribution is higher for $b/\theta_0 = 151.8$ and $b/\theta_0 = 158.5$ which are close to the end of Mode III.

The maximum shear stress achievable during Mode II, 0.0086, is lower than that in Mode III. which is .013. For comparison the value of maximum shear stress for a self-similar, two-dimensional turbulent mixing layer as determined by integrating the velocity profiles presented in Liepmann and Laufer (1947) is .0125. Integration of the velocity profiles measured by Wygnanski and Fiedler (1970) gives $\tau_{max}/\rho U^2_e = .015$. Kistler (1967) reported a maximum value of .012 for two-dimensional cavity shear layers.

Figures 31 and 32 depict the variation of the maximum streamwise and transverse fluctuation as a function of b/θ_0. Again an exponential growth of the disturbances is evident. It is clear from these figures that rms fluctuations suffer from a high percentage noise level of either flow background or electronics.

3.7. Mean and Fluctuating Velocity Field of the Cavity Flow

Figures 33 through 37 present traverses of the velocity field through the cavity for one selected cavity width $(b/\theta_0 = 103)$ in Mode II $\left(\frac{Fb}{U_e} \approx 2\right)$. The particular case selected has a fundamental frequency of 5.1 Hz. Figure 33 presents the mean streamwise $\left(\frac{\bar{u}}{U_e}\right)$ velocity profiles of the upstream boundary layer at the upstream corner, at four stations within the cavity and two stations downstream of the downstream corner. Similarly figure 34 displays the mean $\frac{\bar{v}}{U_e}$

profiles.

The change in flow direction inside the cavity shown in figures 33 and 34 is due to the recirculating vortex flow that is visible in the flow pictures. The upstream boundary layer is laminar and has a shape factor of 2.5. The downstream boundary layer profiles at $x/\theta_0 = 110$ and $x/\theta_0 = 142$, give respective boundary layer shape factors of 1.54 and 1.46. These shape factors are close to that of a turbulent boundary layer.

Figures 35 and 36 reveal that significant fluctuations occur inside the cavity, but the flow field inside the cavity has a much lower shear stress level than that of the shear layer (figure 37), possibly revealing that most of the u' and v' fluctuations are not well correlated. Perhaps the most important difference between $\frac{\overline{u'}}{U_e}$ and $\frac{\overline{v'}}{U_e}$ behavior is shown in the downstream boundary layer profiles (figure 38). The maximum value of the $\frac{\overline{v'}}{U_e}$ profiles in the shear layer continues to increase, even after the shear layer transforms to a boundary layer. On the contrary the maximum value of the $\frac{\overline{u'}}{U_e}$ profiles shows a decrease after the downstream corner. The shear stress profile shows a monotonic decrease in the maximum value of the profile as the shear layer transforms to the boundary layer.

Chapter 4

The Drag Coefficient of the Cavity

Throughout this study the term "drag coefficient of the cavity" refers to the net force in the flow direction being experienced by the gap. The overall changes in the net drag coefficient of the model which might arise from cavity presence, will not be discussed in this study.

4.1. Momentum Balance of the Cavity

A momentum balance for the fluid enclosed by the control surface shown in sketch 5.1 gives

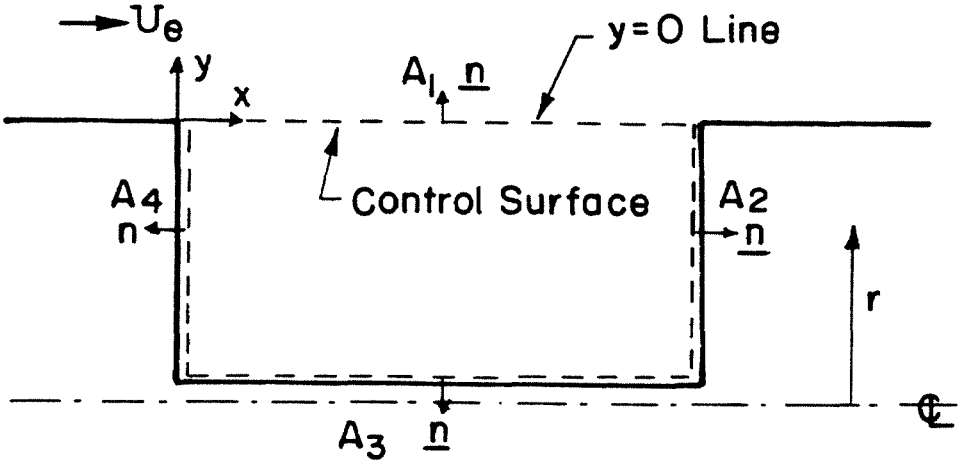

SKETCH 5.1

$$\int_S \underline{U}\,(\underline{U}\cdot\underline{n})dA_1 = -\int_S P\,\underline{n}dA_{2,4} + \int_S \tau\,\underline{n}\,dA_{1,3} \qquad (4.1)$$

where $dA_1 = \pi ddx_1$, $dA_{2,4} = 2\pi r dr$, $dA_3 = \pi ddx_3$ and $\underline{U} = u\underline{i} + v\underline{j}$. The x-

component of momentum balance will be

$$+\rho\pi d \int uv \, dx_1 = -2\pi \int \left[P_2 - P_4\right] r dr + \pi d \int \tau_{xy} dx_1 + \pi d_s \int \tau_{yx} dx_3 \quad (4.2)$$

Introducing $u = \bar{u} + u', v = \bar{v} + v'$ to (2), taking the time average and neglecting the viscous shear stress on the free surface will give

$$+\rho\pi \, d \int (\overline{uv} + \overline{u'v'}) dx_1 = -2\pi \int \left[P_2 - P_4\right] r dr + \pi d \int \tau_{yx} \, dx_3 \quad (4.3)$$

Using the following definition will reduce equation (3) to equation (4)

$$C_{DP} = \textit{cavity pressure drag coefficient} = 2\pi \int \left[P_2 - P_4\right] r dr / \frac{1}{2} \rho U_e^2 \pi d^2 / 4$$

$$C_{DS} = \textit{drag coefficient of the sting} = -\rho\pi d_s \int \tau_{yx} dx_3 / \frac{1}{2} \rho U_e^2 \, \pi d^2 / 4$$

$$-\rho\pi d \int (\overline{uv} + \overline{u'v'}) dx_1 = + C_{DP} + C_{DS} \quad (4.4)$$

However, by definition the drag coefficient of the cavity can be written as

$$C_D = C_{DP} + C_{DS} \quad (4.5)$$

The combination of equations (4.4) and (4.5) results in a new relation for the drag coefficient of the cavity:

$$C_D = -\pi d \int (\overline{uv} + \overline{u'v'}) dx_1 / \frac{1}{2}\rho u^2_e \, \pi d^2/4 \qquad (4.6)$$

Relation (4.6) reveals that it is possible to determine the cavity drag coefficient by evaluating the mean and turbulent momentum transfer terms along a straight line connecting two corners of the cavity. Throughout this section, this line will be called y = 0 line. Roshko (1955) found that the skin friction coefficient along the walls of two-dimensional cavities were two orders of magnitude less than the pressure and pressure drag coefficient. Therefore, skin friction in the cavity as a contribution to the drag is entirely negligible and

$$C_D \approx C_{DP} \qquad (4.7)$$

4.2. Measurement of the Cavity Drag Coefficient.

The drag coefficient of the cavity is determined by measuring the integral of the pressure distribution over the solid walls of the cavity. Figure 39 presents the variation of drag coefficient with b/θ_0 in the three distinct regimes of cavity flow as defined in chapter 3. This figure reveals two rather significant characteristics of the cavity drag. First, the average level of the drag coefficient stays low as long as the flow remains in either the non-oscillating mode or the self-sustained oscillating mode. A second feature is the existence of a critical b/θ_0, in which, by exceeding its value, the drag coefficient of the cavity jumps to a value which is one order of magnitude higher than the typical average drag coefficient during oscillating modes. During the course of the wake mode the drag coefficient increases monotonically and reaches to a value of .39 at $b/\theta_0 = 250$. No more measurements were made beyond this point due to model limitations.

4.2.1. *Cavity Drag Coefficient in Non-Oscillating Mode.*. The drag coefficient in non-oscillating mode has a typical value of 1.3×10^{-4} at $b/\theta_0 = 77$. When the cavity was replaced by a solid surface, the drag coefficient of this surface based on the upstream boundary layer shape factor was estimated to be $.7 \times 10^{-3}$. In turn, this drag coefficient is equivalent to that of $b/\theta_0 = 98$ of Mode II of the oscillations. However, based on observations in Chapter 3, the presence of the cavity reduces the shape factor of the downstream boundary layer and consequently may increase the skin friction drag on the rest of the model. At this point, it is not clear that a net drag reduction can be obtained for the whole model.

4.2.2. *Exponential Growth of the Cavity Drag Coefficient During Oscillating Modes.* Distributions of the drag coefficient in Modes II and III, plotted on a log-linear scale, are presented in figure 40. At the beginning of the oscillating modes (Mode II in this study), the drag coefficient has a value of 0.9×10^{-3} at $b/\theta_0 = 85$. The drag coefficient then increases exponentially and reaches a peak value of 0.02 at $b/\theta_0 = 108$. Toward the end of Mode II, the drag coefficient decreases and reaches a minimum value of 0.004 at $b/\theta_0 = 120$. The transition region between Mode II and Mode III is marked by an increase in the drag coefficient value; $C_{DP} = .0072$ at $b/\theta_0 = 126$. Mode III exhibits another course of exponential growth for the drag coefficient value. A final value of 0.39 for the drag coefficient value is reached at $b/\theta_0 = 250$ before transition to the wake mode occurs.

4.3. Cavity Pressure Distribution

A better understanding of the drag generation mechanism can be obtained from pressure distributions along the solid surfaces of the cavity.

Figures 41 through 43 present the pressure coefficient, $\left[C_p = \frac{P - P_e}{\frac{1}{2}\rho U_e^2}\right]$, along

along a radius of the upstream and downstream faces of the cavity for several selected values of b/θ_0. With each distribution the corresponding value of C_{D_p} is shown.

4.3.1. *Pressure Distribution for Non-oscillating Mode* $b/\theta_0 < 82$.. Figure 41a reveals that in the non-oscillating region, the cavity is slightly under pressure, i.e., $C_p < 0$. No significant differences were observed between the upstream and the downstream face pressure distribution which corresponds to closed and open symbols, respectively.

4.3.2. *Pressure Distribution for Oscillating Modes.*

1) Mode II $\left(82 \leq b/\theta_0 \leq 120\right)$

Figures 41b through 41g show the cavity pressure coefficient distribution for Mode II of the oscillation. All cases have negative pressure distribution over the entire upstream face. The most important point to note in all cases is the steep pressure rise near the outer edge of the downstream face. In each case, C_p reaches its maximum positive value $(C_{p_{max}})$ at the corner. The magnitude of $C_{p_{max}}$ reaches a maximum at $b/\theta_0 = 108$, then decreases toward the end of Mode II. The downstream face experiences a negative pressure below the downstream corner with the same level and trend as that of the upstream face. Thus, the contribution to the total drag from these two portions of the cavity walls cancel each other. This leaves the outer edge of the downstream face with $C_p > 0$, the main contributor to the cavity drag. It is also interesting to mention that in all cases, the average pressure on the upstream face is negative; and thus this face experiences thrust during Mode II of the oscillations.

The pressure buildup near the upstream corner is evidently due to the deflection of the shear layer into the cavity. This deflection of the shear layer

causes a strong inflow to the cavity and contributes to the generation of a stable vortex. A large portion of the cavity experiences negative pressure coefficient due to the presence of strong recirculating flow inside of the cavity. Similar types of observations were made by Johannsen (1955), Roshko (1955), McGregor and White (1970), Charwat, et al. (1961), Fox (1964) and Rossiter (1964).

2) Mode III $120 \leq b/\theta_0 \leq 155$

Figures 42a through 42d present pressure distribution for Mode III. Except for a smoother pressure rise near the outer edge, the pressure distribution on the upstream face shows behavior similar to that of Mode II.

4.3.3. *Pressure Distribution for the Wake Mode..* Pressure distributions for three cases of the wake mode are shown in figure (43). Two main features distinguish the wake mode from the oscillating mode. First, the entire upstream face of the cavity experiences positive pressure, i.e., $C_p > 0$. Second, the stagnation point, the position of $C_{p_{max}}$, steadily migrates toward the center of the cavity. We expect that for a large enough value of b, the stagnation point should settle at the center of downstream face. While pressure on the rear face is increasing, the average base pressure level decreases as b/θ_0 increases (figure (43)).

4.3.4. *Overall Characteristics of the Cavity Pressure Distribution.* Figure 44 presents a collection of typical upstream corner pressure distributions for different regimes of the cavity flow. The start of the self-sustained oscillations is accompanied by an overall drop of the upstream face pressure distribution. The transition from Mode II to Mode III ($b/\theta_0 = 128$) is marked by a substantial increse in the upstream face pressure level. Flow visualization study revealed that the absence of a strong recirculating flow inside the cavity might be responsible for the pressure rise of the upstream face. In Mode III, low upstream face

pressure recovers and shows a level similar to that of Mode II.

Upon the loss of the self-sustained oscillations, another drastic decrease in the average level of the upstream face pressure distribution occurs. At $b/\theta_0 = 210$ ($b/R \approx 1.7$), average upstream face pressure coefficient has a value of -0.13.

Figure 45 represents variation of maximum pressure, $C_{p_{max}}$, with b/θ_0. The value of $C_{p_{max}}$ increases as b/θ_0 increases until it reaches to a local maximum at $b/\theta_0 = 108$. This maximum is immediately followed by a valley which marks the last point of Mode II. The transition region and Mode III show a monotonic increase in the value of $C_{p_{max}}$. Appearance of the wake mode is marked by a sudden increase in the value of $C_{p_{max}}$ from +0.17 to +0.43 at $b/\theta_0 \approx 162$. The value of $C_{p_{max}}$ shows slight decrease during the wake mode. The postion of the stagnation point shifts toward the center of the cavity as b/θ_0 increases. It is important that the location of $C_{p_{max}}$ is fixed in the vicinity of the upstream corner in the self-sustained modes. Migration of this point toward the center of the cavity starts only when the cavity loses the self-sustained oscillation to the wake mode. The rather dramatic change in the pressure field of the cavity caused by exceeding a critical value of b/θ_0 has been observed by Roshko (1955) Charwat (1961), Fox (1968), and Maul (1963). However, the role of self-sustained oscillations in the determination of this critical b/θ_0 was in general unnoticed.

Variation of C_{DP} at the middle of two-dimensional cavities studied by Roshko and Fox as well as those of the present study are shown in figure 46. It is interesting that in all three cases the location of steep jump in the value of C_p agrees fairly well.

4.4. Observation of Sudden Drag and Pressure Change in Other Flows

Several other investigators have reported a sudden change from a steady low-drag flow to a highly non-steady high-drag flow over cavities, cutouts, or bluff bodies in tandem. The intention in this section is to compare some of their results with those of the present study, and to give a possible explanation for the existence of the critical length, b/θ_0.

Koenig (1978) in his study of flow over the combination of a disk and a cylinder, defined two regimes based on the drag behavior of the system, namely, sub and super critical. Drag in a subcritical regime has values one order of magnitude lower than that of a supercritical regime. Separated shear layer in a subcritical regime smoothly joins onto the rearbody, while in the supercritical regime the shear layer becomes unsteady on a much greater scale. Koenig's flow visualization study revealed that the optimum low drag case appears to be a more general example of flow over cavities. Figure 47 presents optimum drag measurements (Koenig, 1978) superimposed on the present drag measurements. Despite the basic differences in the geometry and the curvature of the shear layer, figure 47 confirms Koenig's flow visualization conclusions.

Koenig also reports the presence of a steady and stable flow field in the supercritical region. Production of sharp acoustic tones was another feature of subcritical regime that was reported by Koenig. The symptoms of subcritical regime are similar to those of simple self-sustained cavity flow oscillations.

Mair (1965) reported a sudden change from steady low-drag flow to nonsteady high-drag flow near the base of a streamwise oriented cylinder as the gap between the cylinder and a downstream disk was changed. Zdravkovich (1977) observed an abrupt start of vortex shedding from an upstream cylinder accompanied by an increase in drag of a system comprised of two cylinders in tandem when spacing between them was changed.

The presence of a feedback loop actively doing the task of cross-communication between two corners in the gap generated by two bluff bodies in tandem may possibly explain extra stability and low drag characteristics of such flow systems.

The lock-on of the separated shear layer, or the position of $C_{P_{max}}$ to the downstream corner due to feedback mechanism, has been overlooked by previous investigators and has often been considered a secondary effect. A further discussion of this matter will be given in section 4.10.

4.5. Estimate of C_D by Evaluation of $\frac{\overline{uv}}{U_e^2}$ and $\frac{\overline{u'v'}}{U_e^2}$ Terms Along y = 0 Line

An estimate of C_D can be obtained by integrating the shear stress and mean momentum term over the periphery of the cavity (equation 4.6). LDV technique was used to measure the x and y component of the velocity vector, to determine $\frac{\overline{uv}}{U_e^2}$ and $\frac{\overline{u'v'}}{U_e^2}$ terms along y = 0 line. For each case between 20 to 30, measurement points were selected along the y = 0 line, depending on cavity length. Smaller spacing between measurement points was selected close to the downstream corner. Due to the flow field symmetry of the wake mode, no repeatable measurements could be done in that regime. Thus, evaluation of $\frac{\overline{uv}}{U_e^2}$ and $\frac{\overline{u'v'}}{U_e^2}$ terms were limited to the oscillating regime of the cavity flow.

4.5.1. *Confirmation of Exponential Growth for C_D.*. Figure 40 presents the variation of C_D based on the integration of $\frac{\overline{u'v'}}{U_e^2}$ and $\frac{\overline{uv}}{U_e^2}$ along the y = 0 line with b/θ_0. It is important to note that the exponential growth of C_D during oscillating modes has been confirmed by this independent method. Except for the cases close to the end of Mode II and close to the transition region between Modes II and III, the absolute values of C_{D_p} and C_D agree fairly well. Study of

the $\frac{\bar{v}}{U_e}$, $\frac{\bar{u}}{U_e}$, $\frac{\overline{u'v'}}{U_e^2}$ and $\frac{\overline{uv}}{U_e^2}$ distributions along the y = o line is essential in further understanding of the mechanism which is responsible for the C_D behavior. This is the subject of the following chapters.

4.6. Distribution of $\frac{\bar{v}}{U_e}$ Along y = 0 Line.

Provided that the distribution of $\bar{v}$ at a fixed x position is uniform on the periphery of the cavity, the integral of $\bar{v}$ term along y = 0 line should be minimal for a satisfactory mass balance of the cavity.

Starting from figures 48a through 48g, a sequence of $\frac{\bar{v}}{U_e}$ distributions for several selected b/θ_0 in Mode II is given. Each figure is accompanied by its corresponding drag coefficient.

A common feature of all $\frac{\bar{v}}{U_e}$ distributions is the existence of a narrow region of inflow to the cavity $-\bar{v}$ close to the downstream corner. The negative $\bar{v}$ region is balanced by a broader region of the outflow from the cavity $+\bar{v}$ close to the upstream corner. The stronger the inshooting of flow into the cavity, the higher is the peak of the positive $\bar{v}$ region. The peak of $-\bar{v}$ increases as b/θ_0 increases and reaches a maximum at $b/\theta = 112.5$, which corresponds to the maximum drag case. This peak eventually decreases toward the end of Mode II. In Mode III the $\bar{v}$ region becomes slightly broader and shows a small change (figure 49).

In terms of stable vortex inside the cavity, $\frac{\bar{v}}{U_e}$ distribution can be interpreted as the induced velocity of cavity vortex on the y = 0 line. Therefore, it can be concluded that the strength of the vortex increases during the Mode II as b/θ_0 increases. The strongest and most stable vortex appears at the drag

maximum case; i.e., at b/θ_0 = 112.5, F = 5 Hz. The cavity vortex becomes weaker during transition and recovers its strength during Mode III.

A check of mass balance showed that between 93 to 97 percent of mass entrance, $\int \bar{v} dx \,|_{-v\ REGION}$, exit the cavity. Either a slight angle of attack or presence of three-dimensionalities in flow are responsible for imperfections in the mass balance. It remains to mention that it is logical to assume that positive entrainment to the shear layer, at the upstream region, is the primary process for generating $+\bar{v}$ region and consequently causing the deflection of the shear layer into the cavity at the downstream corner. Relation between the positive entrainment and amplification of the perturbations in the initial region of the shear layer will be discussed in the flow model section.

4.7. Distribution of $\frac{\bar{u}}{U_e}$ Along y = 0 Line.

The $\frac{\bar{u}}{U_e}$ distribution along y = 0 line (figures 50a through 50g) exhibits some interesting features. A typical distribution shows that $\frac{\bar{u}}{U_e}$ increases from zero at x = 0 to a peak value, and is usually followed by a stagnation flow-like behavior where velocity experiences a sharp decrease down to zero at x = b.

The stagnation region often shows several local peaks and valleys. In Mode II, the peak value of $\frac{\bar{u}}{U_e}$ shows an increase until it reaches its maximum at b/θ_0 = 112.5 , corresponding to the maximum drag case. The end of Mode II and the transitional region are marked by lower values for the peak of $\frac{\bar{u}}{U_e}$ similar to that of the $\frac{\bar{v}}{U_e}$ distribution.

Mode III does not show a substantial change in $\frac{\overline{u}}{U_e}$ distribution or value of peak velocity during its course (figure 51). It is important to note that $\frac{\overline{u}}{U_e}|_{max}$ changes from 0.3 to 0.6 during its rise in Mode II, which is a clear indication of deflection of shear layer into the cavity. Consequently this deflection will cause the stagnation of the high velocity portion of the shear layer velocity profile at the downstream corner. It seems that the natural diffusion of the shear layer due to the cavity width increase (shear layer length), plays less a important role in bringing higher velocity fluid into the stagnation region. Decrease in the peak value of $\frac{\overline{u}}{U_e}|_{max}$ during the transitional region, despite the increase of cavity width, supports the previous argument. In Mode III, the averaged level of the $\frac{\overline{u}}{U_e}|_{max}$ (while having a value of 0.5) stays constant (figure 51). Diffusion of the shear layer into the cavity in Mode III probably plays a more important role than the deflection of the shear layer in bringing high velocity fluid to the stagnation region.

4.8. Evaluation of $\frac{\overline{uv}}{U_e^2}$ Along y = 0 Line

The $\frac{\overline{uv}}{U_e^2}$ term is evaluated along the y = 0 line, using the independent measurements of $\frac{\overline{u}}{U_e}$ and $\frac{\overline{v}}{U_e}$ and the results are shown in figures 52a through 52g. A typical distribution of $\frac{\overline{uv}}{U_e^2}$ shows a wide region of positive values for $\frac{\overline{uv}}{U_e^2}$ which is followed by a sharp negative peak close to the downstream corner. The region of positive values of $\frac{\overline{uv}}{U_e^2}$ contributes thrust to the net force balance while the region of negative values of $\frac{\overline{uv}}{U_e^2}$ contributes drag.

It was found that $\int_0^b \frac{\overline{uv}}{U_e^2} dx$ is always negative during Modes II and III of the oscillations. Even though $\frac{\bar{v}}{U_e}$ distribution showed a fairly good mass balance for the cavity, but $-\bar{v}$ region was weighted by higher values of $+\bar{u}$ during integration along the y = 0 line, resulting in a positive net drag for the cavity.

For convenience, the following conventions are introduced. The net contribution of $\frac{\overline{uv}}{U_e^2}$ term to total drag coefficient

$$\equiv C_{D\overline{uv}} = -\frac{8}{d}\int_0^b \frac{\overline{uv}}{U_e^2} dx$$

Net contribution of $\frac{\overline{u'v'}}{U_e^2}$ term to total drag coefficient

$$\equiv C_{D\overline{u'v'}} = -\frac{8}{d}\int_b^0 \frac{\overline{u'v'}}{U_e^2} dx$$

Total Drag Coefficient $\equiv C_D$.

Therefore

$$C_D = C_{D\overline{uv}} + C_{D\overline{u'v'}}$$

A comparison between $C_{D\overline{uv}}$ and $C_{D\overline{u'v'}}$ contributions to the net drag will be given in the next section.

4.9. Shear Stress Distribution Along y=0 Line.

Figures 54a through 54g present shear stress distribution for Mode II. Shear stress grows along the y = 0 line, reaches a peak and vanishes steeply as the flow approaches the downstream stagnation point. Often two peaks appear before the decrease in the stagnation region starts. The peak of $\frac{\overline{u'v'}}{U_e^2}$ reaches the maximum value of .0063 at $b/\theta_0 = 112.5$, which corresponds to the maximum drag case. During the transition region the peak value of the shear stress decreases to 0.003.

The start of Mode III is marked by the appearance of a wide region of high shear stress value close to the downstream corner. In Mode III (figure 55), the peak value of $\frac{\overline{u'v'}}{U_e^2}$ increases from .007 at $b/\theta_0 = 132$ to 0.0098 at $b/\theta_0 = 146$. Figure 56 presents the variation of $\frac{C_{Du\overline{v}}}{C_D}$ and $\frac{C_{D\overline{u}v}}{C_D}$ versus b/θ_0. It also reveals that in Mode II, especially in the beginning stages, $C_{Du\overline{v}}$ contributes up to 80% of the total drag coefficient. As b/θ_0 increases, the role of $C_{D\overline{u}v}$ becomes more important but its contribution never exceeds that of $C_{Du\overline{v}}$. Mode III shows a dominant role for $C_{D\overline{u}\overline{v}}$. Immediately after transition, $C_{D\overline{u}\overline{v}}$ constitutes 60% of C_D and increases to 70% at the critical gap ($b/\theta_0 = 146$). The message of figure 56 is that consideration of the shear stress, $\frac{\overline{u'v'}}{U_e^2}$, as the only means of momentum transfer along the cavity y = 0 line will result in a 30 to 80% underestimation of the cavity drag depending on cavity length.

Kistler (1967) used a similar technique to estimate the drag coefficient of a two-dimensional cavity with a turbulent upstream boundary layer. Using hot wire anemometry, he determined the shear stress distribution along the cavity mouth. His results show up to 60% underestimation of C_D with respect to C_{DP}.

It is important to recall that, due to insensitivity of hot-wire techniques to the direction of the flow, it is impossible to accurately estimate the term $\frac{\overline{uv}}{U_e^2}$ along y = 0 line.

4.10. A Possible Flow Model.

The drag coefficient of the cavity stays low as long as self-sustained oscillations are present in the flow. Flow visualization studies have revealed that the shear layer (time averaged) re-attaches onto the downstream corner. Only during the wake mode does the shear layer stagnate below the downstream corner. The fact that the stagnation point (average position of maximum pressure) is always fixed at the downstream corner supports the flow visualization conclusion. There remains one question to answer: what mechanism keeps the flow from stagnating below the downstream corner and consequently results in a low drag value for the cavity? What follows is a possible answer to the above question.

It is logical to assume that the volume of flow that is entrained by the shear layer is proportional to the strength of the shear forces in the shear layer. Figure 57 reveals that the amount of fluid that is entrained by the shear layer (or exits the cavity $\left[\int \bar{v} dx \,|_{+v}\right]$ follows the trend of maximum shear stress of the shear layer at a fixed streamwise position; e.g., $x/\theta_0 = 65$.

On the other hand, mass balance of the cavity requires that the shear layer deflect into the cavity in order to supply fluid for positive entrainment to its initial region. Figure 23 presents the location of $\frac{\overline{u}}{U_e} = 0.5$ in the shear layer. At the beginning of Mode II ($b/\theta_0 = 83$, F = 6), where shear stress level and growth is low, the shear layer displays mild curvature. At the maximum drag case ($b/\theta_0 = 112.5$), where the shear stress level throughout the shear layer is

higher, the shear layer shows steeper curvature at the initial region and a sharp deflection into the cavity. Therefore, the degree of the deflection of the shear layer depends on the nature of the instability growth in the shear layer. The severity of the shear layer deflection is decisive in the nature of the shear layer interaction with the downstream corner.

Rockwell and Knisely (1979) show that if the respective location of the downstream corner is raised by $\frac{\varepsilon}{\theta_0} = 6$, the rms transverse fluctuations, $\overline{v'}$, will drop by a factor of 2. Sarohia (1976) demonstrated that by external mass injection to the cavity, it is possible to deflect back the shear layer at the corner and weaken the strength of the cavity flow fluctuations. Based on these experiments it can be concluded that for given b/θ_0 the displacement of the impinging shear layer on the corner due to deflection should occur in such a way that the feedback loop would not lose its strength. Any severe external interference with the established self-sustained oscillations would result in an overall drop of the fluctuation level throughout the shear layer. These two experiments provide the missing link between the role of the corner and the fluctuation level. Once the feedback loop due to the frequency selection process is established, any inboard displacement of the velocity profile caused by the natural tendency of the wake mode will be resisted by the following mechanism. A negative displacement of velocity profile at the downstream corner will result in the lowering of the shear stress level which will be followed by a decrease in the volume of positive entrainment. However, a less positive entrainment would result in reduced deflection of the shear layer and restoration of the initial position of the shear layer velocity profile at the downstream corner. This mechanism will not allow the full velocity profile at the impinging corner to be displaced more than its total thickness, and as a consequence, keeps the location of $C_{p_{max}}$ fixed at the downstream corner. The strength of this restoration mechanism depends on

the stability of the cavity flow oscillations, which was already established by the frequency selection process. It is possible that because of the existence of such a restoration mechanism, some low frequency oscillations appear in the shear layer. According to the above process these frequencies need not be the harmonics of fundamental frequency. As was mentioned before, Knisely (1980) observed .5, .4, .6, of fundamental frequency in the shear layer over cavities. In the present study severe low frequency components were observed in Mode III (last mode) of the oscillations. Toward the end of Mode III, as a result of a decrease in the effectiveness of the feedback loop, the restoration force became weaker. Consequently, the natural wake mode of the front body overcame the restoration mechanism, and the shear layer had more freedom to move below the downstream corner and stagnate inside the cavity.

Chapter 5

Control of Cavity Flow Oscillations

One of the objectives of the present study was to develop and use a technique which is capable of controlling the frequency and amplitude of established flow oscillations. However, such a technique can be used to obtain information regarding the necessary conditions for the onset of self-sustained oscillations.

This chapter will report on and discuss a series of experiments regarding the application of a new technique for forcing the cavity shear layer. Throughout these experiments, the response of the cavity shear layer, both in non-oscillating and oscillating modes, is studied against different forcing frequencies and amplitudes.

5.1. Forcing of the Shear Layers

Forcing of the unstable and stable modes of laminar or turbulent shear layers has been the topic of many previous studies. Basically, forcing techniques fall into two catagories:

1) Perturbations to the bulk of either
   flow stream (Miksad 1972, Ho and Huang 1982).
2) Localized perturbations in the initial region of
   the shear layer (Oster and Wygnanski 1982).

In the first type of forcing, e.g., by oscillating one of the streams, the whole streamwise length of the shear layer experiences forcing effects. As a result no accurate information can be deduced about the influence of perturbations on the initial regions of the shear layer.

Wygnanski and Oster showed that forcing effects can be localized by sinusoidal oscillation of a pivoted thin flap at the leading edge of the shear layer splitter plate. The other technique used to localize the effect of forcing is to introduce controlled excited (T-S)* waves, amplified by the boundary layer, into the shear layer. The idea of actively forcing the boundary layer was first proposed by Liepmann (1943). The most popular technique to facilitate the idea was the vibrating-ribbon developed by Schubauer and Skramstad (1947). The difficulty with either the vibrating-ribbon or the flapping edge technique for the present experiments is that it cannot be adapted to axisymmetric flows.

5.2. Surface Heating Technique

Liepmann, Brown and Nosenchuck (1982) recently showed that time-dependent surface heating can be used to introduce perturbations into laminar boundary layers. Such a technique can be easily adapted to excite T-S waves in an axisymmetric boundary layer such as that of the present study. The idea of periodic heat release into the boundary layer for the purpose of exciting T-S waves was also realized by Kendall (1967) in supersonic boundary layers. By applying periodic current to two closely spaced parallel wires flush mounted on the wall, Kendall was able to initiate glowing between the two wires and consequent heat release into the boundary layer. As a result of this periodic heat release into the boundary layer, T-S waves of up to 30 KHz were excited. Requirement of low pressure to attain glowing makes this technique of limited use for subsonic flow applications.

For cases in water, Liepmann, et al. (1982) show that the effect of "heating and cooling of the surface is roughly equivalent to suction and blowing or negative and positive surface displacements," with

* Tollmein-Schlichting

$$\frac{v'}{U_e} = \frac{Pr^{1/3}}{R_x^{\frac{1}{2}}} \left(\frac{x}{w}\right)^{1/3} \frac{d\ LOG\ \mu}{d\ LOG\ T} \frac{\Delta T}{T}$$

where μ is dynamic viscosity, T is the temperature of the fluid, Pr is the Prandtl number, w is the width of the strip, and R_x is the Reynolds number. Such an equivalent normal surface oscillation would periodically redistribute vorticity. Depending on the state of the boundary layer, the external perturbations would either be dampened or amplified exponentially. Linear theory can predict the exponential growth of the (T-S) waves, based on the parameters $\frac{F\theta}{U_e}$ and $Re\delta^*$ for given pressure distribution.

5.2.1. *Application of T-S Waves as a Means of Forcing of the Shear Layer.* Forcing T-S waves in boundary layers has been practiced for a long time. However, to our knowledge, no use has been made of T-S waves to force a separated shear layer resulting from such a boundary layer. In the present study, inspired by the experiment of Liepmann, et al., periodic heating of a thin film was used to excite the T-S waves in the boundary layer upstream of the cavity shear layer, benefitting from amplification of the waves before their introduction into the shear layer (figure 58). One can imagine that the effect of the T-S waves or v' component at the upstream corner of the cavity would be similar to that of the oscillating flap at the leading edge of the splitter plate in Oster and Wygnanski's experiment. It will be seen later that the frequencies needed to excite the free shear layer are available in the range of boundary layer T-S waves. Thus, a transformation of boundary layer T-S waves to the shear layer Kelvin-Helmholtz waves is possible.

5.2.2. *Strip Heater Set-up.* Initially three strip heaters were mounted on the ellipsoidal nose of the model (figure 59) at s = 9.2 cm, 12 cm, and 15.5 cm where s is the distance on the model surface from the nose of the model. Double stick scotch tape was used to electrically isolate heaters from the model. The first and third heaters were stainless steel ribbons 3.7 mm (.125 inch) wide, .051 mm (.002 inch) thick, wrapped around the front nose of the model. The second heater was narrower, .08 cm (.2 inch) wide. Each heater entered the model from a flush mounted round adaptor, designed to connect the heaters to the current supply lines. The resistance of the strip heaters was 2 - 4 ohms.

A high quality commercial dual channel power amplifier (Hafler DH-500) was used to supply current to the strip heaters. DH-500 is a 500 watts per channel amplifier which can be easily modified to provide frequencies even below 1 Hz while delivering adequate power to the strip heater. An HP Function Generator (3325A) was used to provide the selected frequency to the power amplifier. It should be mentioned that due to the quadratic dependence of Joule heating on the voltage, the input frequency to the power amplifier had to be half of the desired forcing frequency.

5.2.3. *Important Parameters of Strip Heater Technique.* Several parameters are important for the efficiency of a strip heater in forcing both the T-S waves and the shear layer. Liepmann, et al. concluded that $\frac{W}{\delta^*}$ (where W is the strip heater width and δ^* is the boundary layer displacement thickness) is an important parameter in effectiveness of strip heater operation on the local forcing of T-S waves. The state of the free stream pressure gradient is another important factor. In the present study, the width-to-boundary layer thickness ratio, $\frac{W}{\delta^*}$ was 5.6 for the first strip heater and maintained at 3 for the second and third heaters.

The preliminary experiments indicated that for a fixed input frequency and power level, the first heater, s = 9.2 cm, was far more effective in forcing the free shear layer than the second and third heaters, set at s - 12 cm and s = 15,5 cm, respectively. Also, it was noticed that having the same ratio $\frac{W}{\delta^*}$, the second heater operated more effectively than the third heater. Figure 59reveals that (T-S) waves initiated by the first and second heaters benefitted from a positive pressure gradient as well as a longer period of amplification than that of the third heater.

In the final version of the experimental model, a single strip heater was flush mounted at s = 9.2 with $\frac{W}{\delta^*} = 5.3$.

5.3. External Forcing of the Non-Oscillating Cavity Flow

The receptivity of the cavity shear layer to externally imposed disturbances was studied. Two different cavity widths were examined, with corresponding $b/\theta = 66 < b/\theta|_{min}$ and $b/\theta = 77 < b/\theta|_{min}$. Throughout this section these selected widths will be called case A and B respectively. In both cases edge velocity was fixed at $U_e = 22 cm/sec$. Cavity flow response was measured in terms of the maximum shear stress that was developed in the shear layer at a station .254 cm (.1 inch) upstream of the downstream corner.

Spectral analysis of the response velocity fluctuations indicated a one to one relation between forcing and the response frequency. For Case A, figure 60 presents the response of the cavity shear layer to a wide band of the forcing frequencies at different levels of forcing power. The results indicate that the level of shear layer response increases as the forcing power increases. For forcing levels above 9 watts, resonance peaks appear at the forcing frequency of 7.2 Hz.

An overall phase measurement revealed that Case A satisfies the phase criterion $\frac{\varphi}{2\pi} = \frac{Fb}{U_c} \approx 2$, at the resonance (F = 7.2 Hz), thus verifing it as the second mode of oscillation. The absence of forcing caused the resonance mode to disappear, thus revealing that the flow oscillations are not self-sustaining. Figure 60 also reveals that the existence of resonance depends on a minimum amplitude threshold.

Figure 61 presents the response of the cavity shear layer for Case B at a fixed forcing level of 9 watts. This case shows a resonance peak at the forcing frequency of 6.2 Hz with $\frac{\varphi}{2\pi} = \frac{Fb}{U_c} \approx 2$. Appearance of resonance peak for Case B at a lower forcing level than that of case A, indicates that the threshold level decreases as b/θ_0 increases. In Case B, the effect of initial lower amplitude of the forcing was compensated by longer cavity length in such a way that reduced the required forcing level for the resonance condition. The effect of higher forcing power on the exponential growth of the perturbations was to increase the general level of fluctuation growth (figure 62a). Figure 62b presents the growth behavior of the different frequencies for a fixed forcing level (9 watts) for Case B.

It can be concluded that external frequencies can be imposed on naturally non-oscillating cavity flows, within the receptivity range of the shear layer. These frequencies can cause the cavity flow to resonate if they satisfy the following conditions:

1) $\frac{\varphi}{2\pi} = N$ for the given width (b); and

2) $A > A_{Th}$ where A is the amplitude of external frequency at the downstream corner and A_{Th} is the threshold amplitude. It is logical to propose that as the cavity width increases, the threshold level decreases to such an extent

that a flow background frequency, which satisfies the phase criterion and has sufficient amplitude, will initiate the self-sustained oscillation.

It is now clear that due to the absence of proper frequencies with sufficient intensities in the flow background, the first mode did not appear naturally in this study. However, by selecting a proper forcing frequency and initial amplitude, the first mode of oscillations $\left(\frac{\varphi}{2\pi} = \frac{Fb}{U_c} \approx 1\right)$ was simulated for Case A. This was accomplished at a forcing frequency of 4 Hz, a power level of 35 watts. A flow visualization of this case is shown in figure 63b. In comparison to figure 63a, which is the same case but unforced, two features are noteworthy. The first is the appearance of a small amplitude wave in the shear layer of the forced case. The second is the interaction of this wave with the downstream corner and the resultant strong recirculating flow inside the cavity.

It is interesting to note that the response of the cavity flow to external forcing is not instantaneous. Figures 64a and 64b present simultaneous traces of the velocity fluctuations taken at stations corresponding to $\frac{x}{\theta} = 10$ and $\frac{x}{\theta} = 60$, respectively. The cavity was in the non-oscillating mode with $b/\theta = 66$. Figure 62a indicates that for an external forcing frequency of 7 Hz, simulating Mode II, it takes 3 cycles of the oscillation before the peak amplitude establishes itself. When the forcing is turned off it takes many more cycles for the amplitude of oscillations to diminish.

5.3.1. *Effect of External Forcing on Cavity Drag in the Non-Oscillating Mode.*. Case B, at the resonance, had a drag coefficient of 0.0012. This drag coefficient was one order of magnitude higher than that of the same case but in the absence of forcing. Distributions of $\frac{\overline{uv}}{U_e^2}$ and $\frac{\overline{u'v'}}{U_e^2}$ along the $y = 0$ line for both the forced and unforced cavity are given in figures 65a and 65b. These

figures reveal that the difference in the drag coefficient of forced and unforced cases can be contributed to the development of a strong shear stress level in the forced case.

5.4. Effect of External Forcing on a Naturally Oscillating Cavity Flow $\left(b/\theta > b/\theta|_{min}\right)$.

Once the cavity flow established the self-sustained oscillations $\left(b/\theta_0 > b/\theta_0|_{min}\right)$, the flow resisted any external disturbances. Thus in order to interact with the flow oscillations, it was expected that the amplitude level of external forcing must be comparable to that of the self-sustained fluctuations in the flow.

A non-dimensional cavity width of $b/\theta_0 = 95$ was selected for an external forcing experiment. The cavity flow was oscillating at 5.4 Hz in Mode II. An external forcing frequency of 6 Hz was introduced to the shear layer. Depicted in figures 66a through 66g are the spectral distributions of velocity fluctuations for several levels of forcing as the forcing power was changed from 2 to 27 watts.

Spectra reveal that as the amplitude of the forcing increases, the amplitude of natural oscillation decreases and eventually disappears. At the forcing power of 40 watts, the forced frequency becomes the dominant frequency of the oscillations. Oscilloscope traces of the signal for the case when both natural and forced frequency have the same amplitude, as seen in figure 66d, are given in figure 66h. Strong modulation of the signal indicates that both frequencies are present simultaneously. Note that in the co-existence region, figures 66b through 66f, the peak amplitude of both frequencies is lower than that of the single frequency regions of figures 66f and 66g.

Miksad (1973) in his study of dual excitation of a free shear layer observed a similar interaction of two frequencies. He reported that if the excitation

amplitudes were adjusted so that both disturbances reached finite amplitude together, the final amplitudes of both components tended to be reduced, but not as strongly as when one component was clearly dominant. Miksad concluded that the distortion of the mean flow by the stronger frequency made velocity field unsuitable for the growth of the weaker frequency. Similar behavior had also been observed by Sato (1970) in symmetric wakes.

Important to our study is the fact that the amplitude of the forced frequency in figure 66g, where natural frequency just disappears, is equal to that of the natural frequency in the absence of the forced frequency (figure 66a). This fact establishes the amplitude of the natural frequency as the level which should be exceeded by the amplitude of forced frequency to change the frequency of the oscillations. With this rule it is possible to impose forced frequencies on the cavity shear layer within the receptivity range of the shear layer. These forced oscillations are not, in general, self-sustaining. During the mode switching region (hysteresis region), self-sustaining oscillation in a desired mode could be achieved by providing a proper frequency within the hysteresis region of that mode. Thus, the mode switching phenomena could be eliminated by external forcing. Transition to the wake mode could be prevented by enhancing the amplitude of natural frequency through external forcing. It is possible to extend Mode III, last mode in this study, by 20 momentum thickness through external forcing. However, once the cavity entered the wake mode, it was not possible to re-establish cavity flow oscillations by external forcing.

A map of possible interaction with the cavity flow oscillations observed in this experiment is given in figure 67.

5.5. Cancellation Experiment

Cavity width of $b/\theta_0 = 82$, with frequency of 6 Hz, was selected for the cancellation experiment. The signal from a downstream location was fed to a function generator (Tektronix FG504) which had a built-in phase lock loop. It was possible to lock to lower harmonics of the input signal. Phase variation of the output signal with respect to the first subharmonic of the input signal was possible through an independent manual adjustment knob. The power amplifier was then supplied by the output of the function generator. The experimental set up is sketched in figure 68.

The following procedure was conducted in the cancellation experiment.

1) Output amplitude of function generator was set at 0.

2) Phase lock loop was locked to first subharmonic of the input signal.

3) Knowing the threshold amplitude, the power was fixed at a level which was enough to simulate conditions as depicted in figure 66d.

4) Step (3) was repeated for different phase angles between input and output of the function generator (phase lock loop).

Due to the small rapid phase changes of the cavity flow oscillations it was not possible to have a phase lock situation for an extended period of time. Occasionally a correct phase angle could be found where the forced and natural frequencies would interact in such a way that wide band rms fluctuations were

reduced. A sample of such a cancellation is shown in figure 69. A reduction in rms fluctuation was achieved by a factor of 2 during 30 cycles of the cavity shear layer oscillations. Liepmann and Nosenchuck (1982) report a factor of 2-3 in the reduction of rms fluctuations of the natural (T-S) waves in the flat plate boundary layer.

Chapter 6

CONCLUSIONS

6.1. Summary of Results

(a) Investigation of the flow field in the oscillating mode reveals that the momentum thickness of the cavity shear layer grows linearly with x/θ_0. The linear growth of the momentum thickness may indicate the existence of self-similarity in the flow. However, the self-similarity argument for the free shear layer requires a constant maximum shear stress along the layer. In contrast, cavity shear layers show an exponential growth of the maximum shear stress with x/θ_0. The cavity shear layer in the non-oscillating mode does not develop any noticeable shear stress along its span. The velocity measurements also verify the existence of a recirculating flow inside the cavity. Streamwise and transverse velocity fluctuations as high as those of the shear layer are detected in the recirculating region.

(b) Upstream laminar boundary layer has a shape factor value of 2.5. The effect of the cavity on this profile is found to decrease the shape factor to a value of 1.54, which is close to that of the turbulent boundary layer.

(c) The drag measurement results presented in figure 39 indicate that the drag coefficient of an axisymmetric cavity with laminar upstream boundary layer remains low as long as the cavity flow stays in a non-oscillating or self-sustained oscillating mode. Results also reveal that the drag of the cavity in the non-oscillating region is less than the case in which the cavity were replaced by a solid surface.

(d) Flow visualization study (figure 16) in conjunction with the drag measurements reveals that for a long enough cavity width, $b/R > 1.2$, cavity flow exhibits a wake type behavior. Also,the average drag coefficient in this mode, $C_D \approx 0.35$, is one order of magnitude higher than the highest drag coefficient in the oscillating mode, $C_D = .036$.

(e) The most important result is presented in figure 40. The drag coefficient of the cavity exhibits an exponential dependence with b/θ_0 in Mode II of the oscillations followed by a decrease in the same mode and another course of exponential growth in Mode III. An independent estimate of the drag coefficient through measurement of the shear stress and mean momentum transfer terms $\overline{uv}$ along the y = 0 line confirmed the exponential growth of the cavity drag. Furthermore, these measurements revealed that the $\overline{uv}$ term is responsible for 30% to 80% of the net drag coefficient of the cavity.

(f) Study of the cavity pressure distribution revealed that the pressure rise close to the outer region of the downstream corner is responsible for the drag coefficient of the cavity.

(g) In the oscillating modes of the cavity flow, the maximum pressure coefficient ($C_{p_{max}}$) always occurs at the upstream corner and stays so until the wake mode appears. In the wake mode the position of maximum pressure coefficient ($C_{p_{max}}$) moves toward the center of the cavity as b/θ_0 increases.

(h) The existence of the feed-back loop introduces an extra stability to the cavity flow field which includes a fixation feature of $C_{p_{max}}$ at the upstream corner and a resultant low drag for the cavity.

(i) The distribution of the shear stress along a straight line connecting two corners of the cavity, is shown to have direct effect on the positive transverse

velocity $(+\bar{v})$ distribution on the same line. It is also shown that the deflection of the shear into the cavity is related to the distribution of positive transverse velocity through the mass balance of the cavity.

(j) Stronger deflection of the shear layer into the cavity causes a higher $\overline{uv}$ region to develop close to the downstream corner and the drag of the cavity to increase. Thus, shear stress development along the shear layer has a direct effect on the drag of the cavity as well as an indirect effect through its role on the development of the $\overline{uv}$ term.

The type of shear layer interaction with the downstream corner which depends on the shear layer deflection is decisive in the development of the shear stress throughout the cavity shear layer. Based on the findings of previous experiments, it is proposed that inward displacements of the shear layer with respect to the downstream corner will result in an overall drop of the shear stress level. As a result of this overall shear stress drop, a less positive region of transverse velocity develops. Consequently, the mass balance of the cavity requires less deflection of the shear into the cavity. It also requires that the shear layer deflect back and restore the position of the shear layer. This mechanism keeps the position of $C_{p_{max}}$ fixed at the upstream corner and it might also introduce some low frequency components to the oscillations.

(k) The control of the cavity flow oscillation is facilitated by external forcing of the cavity shear layer. It is shown that the excited T-S waves can be used to force the shear layer generated from separation of respective boundary layers. Thus, a transformation of the T-S waves of the boundary layer to the Kelvin-Helmholtz waves of the shear layer is possible.

(l) For short cavities, i.e., non-oscillating mode $b/\theta_0 \leq 82$, periodic flow oscillation at a wide range of frequencies was obtained. A resonance condition was

observed for a selected forcing frequency if it

1) satified the phase criterion $\frac{\varphi}{2\pi} = N$

and

2) its amplitude exceeded certain threshold amplitude.

For a fixed amplitude the threshold level increases as b decreases. The forced resonance cases are not self-sustaining.

(m) Previous conclusions indicate that, for a given b/θ_0 the first frequency in the flow background that satisfies the phase criterion and has sufficiently high amplitude will start the self-sustained oscillations. Thus the determination of the $b/\theta_0|_{min}$ strongly depends on the turbulence content of the flow background.

(n) Cavity drag in the non-oscillating mode can be increased by one order of magnitude through external forcing. Non-oscillating cavity flow at $b/\theta_0 = 77$ produces a drag coefficient value of 1.3×10^{-4}. External forcing at 6 Hz and power level of 9 watts increases the drag coefficient to a value of 1.2×10^{-3}. It is also possible to generate shear stress levels several orders of magnitude higher than that of the laminar shear layer by external forcing.

(o) For naturally occurring oscillations it is possible for two waves to co-exist in the shear layer (natural and forced). Spectral analysis, however, shows that the amplitude of the forcing frequency has a direct effect on the growth of the natural frequency. External forcing made possible the ability to completely subsidize the natural self-sustained frequency by a non-self-sustained frequency. It is shown that the amplitude of the established self-sustained oscillation is the amplitude level that should be exceeded by the amplitude of the forced frequency for complete switching of self-sustained to forced frequency.

(p) Mode switching or transition to the wake mode can be delayed by enhancing the self-sustained oscillations through external forcing. Once the wake mode appears, the self-sustained oscillations cannot be re-established. Different mode extension and simulation is possible by providing the proper forcing frequency to the cavity shear layer.

(q) The most important result of external forcing is the possibility of cancelling or damping the established self-sustained oscillations. An external forcing frequency equivalent to that of the cavity with an amplitude less than threshold level which has a proper phase angle respective to that of the self-sustained one was able to reduce rms fluctuations by a factor of 2.

6.2. Concluding Remarks.

This study has disclosed that the presence of self-sustained oscillations helps in keeping a low level of drag coefficient for the cavity. A more detailed study of the role of the downstream corner on the overall development of the shear stress along the shear layer and on the drag of the cavity is desirable. It is important to clarify the effect of the cavity presence on the net drag coefficient of the system.

With respect to the active control of the cavity flow oscillations, if a more elaborate feed-back system is used, a high percentage of fluctuation cancellation might be attainable.

Appendix A

Determination of Overall Phase Difference for the Cavity

For the purpose of obtaining phase information between two time dependent signals, the cross-correlation function between these two signals should be carried out. By cross-correlating two signals the relative non-dimensional phase change between the location of the reference probe and the second probe can be determined. This is done, as shown in sketch (SA-1), by measuring the time shift, along the positive τ-axis, between two corresponding peaks in the cross-correlation function of two signals and dividing this time by the average period between peaks.

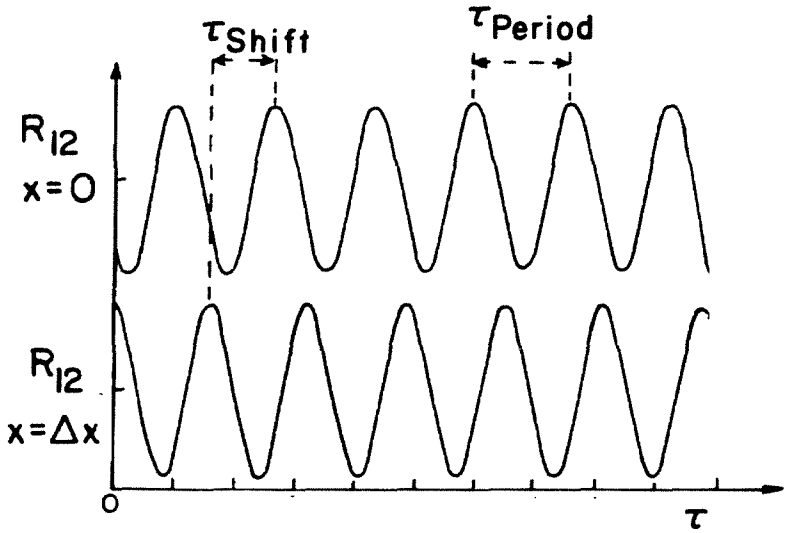

SKETCH SA-1

Then the non-dimensional phase difference between two locations separated by Δx will be

$$\frac{\Delta\varphi}{2\pi} = \frac{\tau_{SHIFT}}{\tau_{AVERAGE\ PERIOD}} \tag{1}$$

The wave length of the oscillation can be determined as

$$\lambda = \Delta x \cdot \frac{2\pi}{\Delta\varphi} \tag{2}$$

Knowing the fundamental frequency of oscillation, the phase velocity can be calculated from

$$U_c = f\,\lambda \tag{3}$$

Overall phase difference between the two corners is given by

$$\varphi = \frac{b}{\Delta x} \cdot \Delta\varphi \tag{4}$$

Appendix B

Laser Doppler Velocimeter Optical Arrangement

A two watt argon-ion laser is used as the light source. Past a collimating lens, a color separator provides two lines of the laser, the 514 nm green line and 488 nm blue line. Each beam is split into two pairs of equal intensity beams by a polarization rotator and a beam splitter. Each pair passes through its designated frequency shifter. Non-desired diffracted beams are blocked by two slit mechanisms. The measuring volume is formed by focussing the four parallel beams by a single 598 mm focal length lens. The collimator is used to minimize the lateral extent of the focal volume.

The scattered light from the particles is collected by a 600 mm focal length lens. A dichroic mirror is used for color separation, with a focussing lens used to focus the scattered light of each of the two colors into a pin-hole (250 μ m) and photomultiplier tube assembly. A first-surface flat mirror is used to rotate the beam 90 °. A second mirror is used to deflect the scattered light into the collecting optics.

The component of the velocity vector measured by the LDV and the Doppler constant, the conversion factor from frequency to velocity, is determined by the transmitting optics. The green beams pair enters the test section in a plane forming an angle of 0° with the downstream direction, while the blue beams plane forms an angle of 90°. Therefore, streamwise velocity component is measured by the fringe system formed by the green beams while velocity components perpendicular to the mean free stream are measured by the fringe system formed by the blue beams. Figure A-1 presents the schematic of focal volume formation. The Doppler constant which is related to the fringe spacing within

the focal volume is given by the equation

$$\kappa = \frac{\lambda}{2 \sin \frac{\alpha}{2}}$$

where λ is the light wavelength and α the angle at which the beams cross in the focal volume. The angle $\alpha = 4.72°$ was used which gives Doppler constants for the green and blue components $\kappa_G = 6.24\ (m/sec)\ (MHz)^{-1}$ and $\kappa_B = 5.92\ (m/sec)\ (MHz)^{-1}$ respectively. The geometrical characteristics of the focal volume are summarized in Table A-1.

Appendix C

Velocity Bias and Bragg Cell

Fringes of the measuring volume are formed by the interfering effect of the two beams crossing. These fringes are stationary and do not produce Doppler frequency for a stationary particle in the measuring volume.

Shifting the frequency of one beam can produce a system of moving fringes. Then, a stationary particle in the measuring volume will give an output frequency from the photo detector. If the velocity increases in the direction of the fringe movement, the frequency will decrease. If it is opposite to the fringe movement, the frequency will increase. Therefore knowing the direction of the fringe system movement will discern the particle direction.

In this experiment, two acousto-optic cells (Bragg cell) were used to frequency shift one beam of each color by a fixed 40 MHz. Each cell is installed in a cylindrical housing that aligns with the optical axis. A compensating wedge is used to correct for shifted beam deflection, and a tilt adjustment allows shifting light intensity to the deflected beam, as much as 80%. The cell is derived by a 40 MHz, 2 watt signal provided by a power amplifier. A frequency of 40 MHz is often too large. A downmix circuit permits decrease of the effective frequency shift of the photodetector output to values from 2KHz to 10 MHz in a 2, 5, 10, sequence. Bragg shifts of nominally 30 and 50 KHz were used. In this study the green (U component) channel was shifted against the mean flow, while the blue channel (V component) was shifted in the positive y direction (figure A-1).

Appendix D

LDV Signal Processing

The burst processing encompasses the required electronics for the actual measurement of the particle velocity. A particle burst is considered valid if it satisfies the following conditions:

1) Its amplitude crosses zero and exceeds the threshold level (about 50 mV).
2) For zero crossing (with hysteresis), the signal should be more than 10 mV.

The pulse that occurs on a zero crossing after the threshold has been exceeded is the signal of the interest. At this point the leading edge of a time envelope is marked (by the processor) and gates a high speed clock (250 MHz) into a counter. The length of the envelope is determined by the total number of cycles that exceed the threshold. The first cycle that exceeds the hysteresis level but not the threshold level determines the trailing edge of the envelope. The trailing edge stops the counter and the clock. The input frequency is then:

$$INPUT\ FREQUENCY\ (\omega) = \frac{ENVELOPE\ CYCLE\ NUMBERS}{TOTAL\ ENVELOPE\ TIME}$$

The resolution of time measurement is 1 nsec. In this experiment only bursts with more than 16 cycles were used for processing. A schematic of valid burst processing is given in figure A-2. The output of the burst processor is in digital form. It feeds into the computer interface that incorporates the coincidence test between the two processors. The coincidence test consists of the initiation of a time window after completion of processing by one of the processors. If

data from the other processor are not received before the end of the window the data are discharged; otherwise coincidence is attained and the data from both processors are transferred to the computer.

A minicomputer was used to acquire and store the data. A computer program was developed for data acquisition using the LDV system. This computer program accomplishes two tasks. It generates a header which contains information relevant to the conditions of the experiment and the LDV setup. It also acquires a buffer of 16,000 words of data. This buffer size corresponds to a total of 3200 velocity measurements in two-component measurements, since two words are generated for each component and one word was used for the time interval information between data points.

Appendix E

LDV Data Processing

The following expressions are used to calculate the mean, second moment and cross-correlation between two velocity components.

$$\overline{\omega}_G = \sum_{i=1}^{N} \frac{\left[\left(\omega_i\right)_G + \left(\omega_{i+1}\right)_G\right] \Delta\tau_i}{2 \sum_{i=1}^{N} \Delta\tau_i} \tag{1}$$

$$\overline{\omega}_B = \sum_{i=1}^{N} \frac{\left[\left(\omega_i\right)_B + \left(\omega_{i+1}\right)_B\right] \Delta\tau_i}{2 \sum_{i=1}^{N} \Delta\tau_i} \tag{2}$$

$$\overline{\omega^2}_G = \sum_{i=1}^{N} \frac{\left[\left(\omega_i\right)^2_G + \left(\omega_{i+1}\right)^2_G\right] \Delta\tau_i}{2 \sum_{i=1}^{N} \Delta\tau_i} \tag{3}$$

$$\overline{\omega^2}_B = \sum_{i=1}^{N} \frac{\left[\left(\omega_i\right)^2_B + \left(\omega_{i+1}\right)^2_B\right] \Delta\tau_i}{2 \sum_{i=1}^{N} \Delta\tau_i} \tag{4}$$

$$\overline{\omega_G}\overline{\omega_B} = \sum_{i=1}^{N} \frac{\left[\left(\omega_i\right)_G + \left(\omega_{i+1}\right)_G\right] \times \left[\left(\omega_i\right)_B + \left(\omega_{i+1}\right)_B\right] \Delta\tau_i}{2 \sum_{i=1}^{N} \Delta\tau_i} \tag{5}$$

where $\Delta\tau_i$ is the time between data points and ω is the frequency. The subscripts G and B refer to the frequencies measured by the green and blue beams respectively. The equations relating the mean and the correlations of the various velocity components are

$$\bar{u} = \left(\bar{\omega}_G - FS_G\right) \kappa_G , \quad \bar{v} = \left(\bar{\omega}_B - FS_B\right) \kappa_B \tag{6}$$

$$\overline{u^2} = \left(\overline{\omega^2}_G - 2\bar{\omega}\, FS_G + FS^2_G\right) \kappa^2_G \tag{7}$$

$$\overline{v^2} = \left(\overline{\omega^2}_B - 2\bar{\omega}_B\, FS_B + FS^2_B\right) \kappa^2_B \tag{8}$$

$$\overline{uv} = \left(\bar{\omega}_G\bar{\omega}_B - \bar{\omega}_G FS_B - \bar{\omega}_B FS_G + FS_G FS_B\right) \kappa_B \times \kappa_G \tag{9}$$

where FS_G and FS_B are frequency shift of green and blue channel respectively. κ is the frequency to velocity conversion factor.

Rms fluctuations and shear stress values can be obtained using the following relationships:

$$\bar{u}' = \sqrt{\overline{u^2} - \bar{u}^2} \tag{10}$$

$$\bar{v}' = \sqrt{\overline{v^2} - \bar{v}^2} \tag{11}$$

$$\overline{u'v'} = \overline{uv} - \overline{u}\,\overline{v} \qquad (12)$$

No corrections were made to the data presented in this study.

References

Ball, J.W. 1957 "Hydraulic characteristics of gate slots." *Proc. ASCE, J. Hydraulics Division*, **85**, HY10 .

Browand, F.K. 1966 "An experimental investigation of the instability of an incompressible, separated shear layer." *J. Fluid Mech.*, **26**, p. 281.

Brown, G.L. and Roshko, A. 1974 "Density effects and large structure in turbulent mixing layers." *J. Fluid Mech.*, **64**, pp. 775-816.

Charwat, A,F,, Roos, J.N., Dewey, F.C. and Hits, J.A. 1961 "An investigation of separated flows. Part 1. The pressure field." *J. Aerospace Sciences*, **28**, no. 6, pp. 457-470.

Dewey, C.F., Jr. 1976 "Qualitative and quantitative flow field visualization utilizing laser-induced fluorescence." AGARD-CP-193, pp. 17-1, 17-7.

East, L.F. 1966 "Aerodynamic induced resonance in rectangular cavities." *J. Sound and Vibration*, **3**, no. 3, pp. 277-287.

Elder, S.A. 1978 "Self-excited depth mode resonance for a wall-mounted cavity in turbulent flow." *J. Acoustical Society of American*, **64**, no. 3, pp. 877-890.

Ethembabaoglu, S. 1973 "On the fluctuating flow characteristics in the vicinity of gate slots." *Div. Hydraulic Eng.*, University of Trondheim, Norwegian Institute of Technology.

Fox, J. 1968 "A criterion for the transition between flow regimes in turbulent cavity flow." *AIAA J.*, **4**, no. 2, p. 364.

Fox, J. 1964 "Surface pressure and turbulent air flow in transverse rectangular notches." *NASA TN D-2051.*

Freymuth, P. 1966 "On transition in a separated laminar boundary layer." *J. Fluid Mech.*, **25**, p. 683.

Goree, J.A., Dimotakis, P.E. and Koochesfahani, M.M. 1980 "Measurements of two velocity components in the two dimensional mixing layer." *Private communication.*

Heller, H.H. and Bliss, D.B. 1975 "The physical mechanism of flow-induced pressure fluctuations in cavities and concepts for their suppression." *AIAA Paper 75-471* Presented at 2nd AIAA Aeroacoustics Conference, Hampton, VA. March 24-26.

Ho, C.H. and Huang, L.S. 1982 "Subharmonics and vortex merging in mixing layers." *J. Fluid Mech.* **119**, pp. 443-473.

Hussain, A.K.M.F. 1981 "Coherent structures and studies of perturbed and unperturbed jets." *Lecture Notes in Physics*, **136**, Springer-Verlag, Berlin.

Johannesen, N.H. 1955 "Experiments on supersonic flow past bodies of revolution with annular gaps of rectangular section." *Phil. Mag. Ser.* **7**, 46, pp. 31-39.

Karamcheti, K. 1956 "Sound radiated from surface cutouts in high-speed flows." Ph.D. Thesis, California Institute of Technology, Pasadena, CA.

Kendall, J.M. 1967 "Supersonic boundary layer stability experiments." *Proc. of Boundary Layer Transition Study Group Meeting*, **II**, Aerospace Corp, San Bernardino, CA.

Kistler, A.L. and Tan, F.C. 1967 "Some properties of turbulent separated flows." *Phys. Fluids*, Supplement, p. 165.

Knisely, C.W. 1980 "An experimental investigation of low frequency self-modulation of incompressible impinging cavity shear layers." Ph.D. Dissertation, Lehigh University, Bethlehem, PA.

Koenig, K. 1978 "Interference effects on the drag of bluff bodies in tandem." Ph.D. Thesis, California Institute of Technology, Pasadena, CA.

Laufer, J. and Monkewitz, P. 1980 "On turbulent jet flows in a new perspective." *AIAA Paper No. 80-0962.*

Liepmann, H.W. 1943 "Investigation of boundary layer transition on curved boundaries." NACA Rep. 3H30.

Liepmann, H.W., Brown, G.L. and Nosenchuck, D.M. 1982 "Control of laminar-instability waves using a new technique." *J. Fluid Mech.*, **118**, pp. 187-200.

Liepmann, H.W. and Laufer, J. 1947 "Investigations of free turbulent mixing." *NACA Tech. Note No. 1257.*

Liepmann, H.W. and Nosenchuck, D.M. 1982 "Active control of laminar-turbulent transition." *J. Fluid Mech.*, **118**, pp. 201-204.

Mair, W.A. 1965 "The effect of a rear-mounted disc on the drag of a blunt-based body of revolution." *Aeronaut. Quart.* Nov., pp. 350-360.

Maul, D.J. and East, L.F. 1963 "Three-dimensional flow in cavities." *J. Fluid Mech.*, **16**, pp. 620-632.

McGregor, D.W. and White, R.A. 1970 "Drag of rectangular cavities in supersonic and transonic flow including the effect of cavity resonance." *AIAA J.* **8**, pp. 1959-1964.

Michalke, A. 1965 "On spatially growing disturbances in an inviscid shear layer." *J. Fluid Mech.* **23**, pp. 521-544.

Miksad, R.W. 1973 "Experiments on nonlinear interactions in the transition of a free shear layer." *J. Fluid Mech.*, **65**, p. 695.

Miksad, R.W. 1972 "Experiments on the nonlinear stages of free shear layer transition." *J. Fluid Mech.*, **56**, p. 695.

Oster, D. and Wygnanski, I. 1982 "The forced mixing layer between parallel streams." *J. Fluid Mech.* **123**, pp. 91-130.

Plumblee, H.E., Gibson, J.S., and Lassiter, L.W. 1962 "A theoretical experimental investigation of acoustic response of cavities in an aerodynamic flow." *WADD-TR-61-75.*

Rockwell, D. and Knisely, C. 1980b "Vortex-edge interaction: mechanisms for generating low frequency components." *Phys. Fluids*, **23**, pp. 239-240.

Rockwell, D. and Knisely, C. 1979 "The organized nature of flow impingement upon a corner." *J. Fluid Mech.* **93**, p. 413.

Rockwell, D. and Naudascher, E. 1978 "Review self-sustaining oscillations of flow past cavities." *J. Fluid Eng., Trans. ASME*, **100**, pp. 152-165.

Rockwell, D. and Schachenmann, A. 1982 "Self-generation of organized waves in an impinging tubulent jet at low Mach number." *J. Fluid Mech.*, **117**, pp. 425- .

Roshko, A. 1955 "Some measurements of flow in a rectangular cutout." *NACA Tech. Note No. 3488.*

Roshko, A. and Koenig, K. 1978 "Interaction effects on the drag of bluff bodies in tandem." Proc. of a Symposium held at the General Motors Research Laboratories, Warren Michigan, Sept. 1976, pp. 253-273.

Rossiter, J.E. 1964 "Wind tunnel experiments on the flow over rectangular cavities at subsonic and transonic speeds." *R&M No. 3438*,. Replaces R.A.E. Tech. Rep. No. 64037-A.R.C. 26621.

Sarohia, V. 1975 "Experimental and analytical investigation of oscillations in flows over cavities." Ph.D. Thesis, California Institute of Technology, Pasadena, CA.

Sarohia, V. and Massier, P.E. 1976 "Control of cavity noise." *AIAA Paper No. 76-528.* Presented at 3rd AIAA Aero-Acoustics Conference, Palo Alto, CA., July 20-23. 1976.

Sato, H. 1970 "An experimental study of non-linear interaction of velocity fluctuations in the transition region of a two-dimensional wake." *J. Fluid Mech.*, **44**, Part 4, pp. 741-765.

Schubauer, G.B. and Skramstad, H.K. 1947 "Laminar boundary-layer oscillations and stability of laminar flow." *J. Aero. Sci.* **14**, pp. 68-78.

Stuart, J.T. 1967 "On finite amplitude oscillations in laminar mixing layers." *J. Fluid Mech.*, **29**, pp. 417- .

Tam, C.K.W. and Block, P.J.W. 1978 "On tones and pressure oscillations induced by flow over rectangular cavities." *J. Fluid Mech.*, **89**, pp. 373-399.

Tani, I., Iuchi, M. and Komoda, H. 1961 "Experimental investigation of flow separation associated with a step or a groove." Aero. Research Institute, Univ. of Tokyo Rep. No. 364.

Werle, H. 1974 "Le tunnel hydrodynamique au service de la recherche aerospatiale." Publ. No. 156, ONERA, France.

White, R.A. 1971 "Some results on the heat transfer within resonant cavities at subsonic and supersonic Mach numbers." *J. Basic Eng., Trans. ASME, Series D.* **93**, pp. 537-542.

Winant, C.D. and Browand, F.K. 1974 "Vortex pairing: the mechanism of turbulent mixing layer growth at moderate Reynolds number." *J. Fluid Mech.* **63**, pp. 273-255.

Wygnanski, I. and Fiedler, H.E. 1970 "The two-dimensional mixing region." *J. Fluid Mech.* **41**, p. 327 - .

Zdravkovich, M.M. and Pridden, D.L. 1977 "Interference between two circular cylinders; Series of unexpected discontinuities." *J. of Ind. Aerodynamics*, **2**, pp. 255-270.

Ziada, S. and Rockwell, D. 1981 "Generation of higher harmonics in a self-oscillating mixing layer edge system." *AIAA J.*, **20**, no. 2, p. 196.

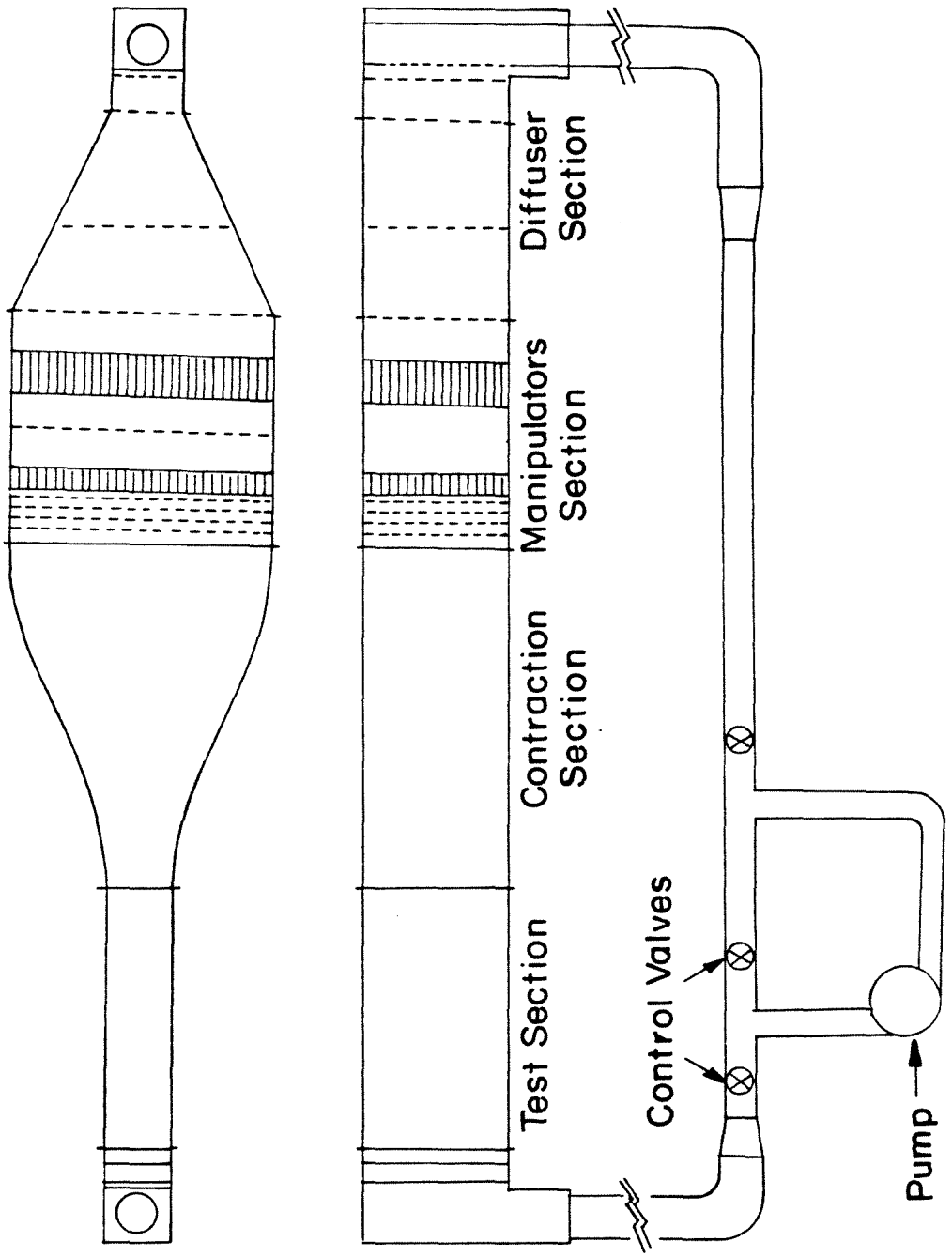

Fig. 1 Water tunnel schematic.

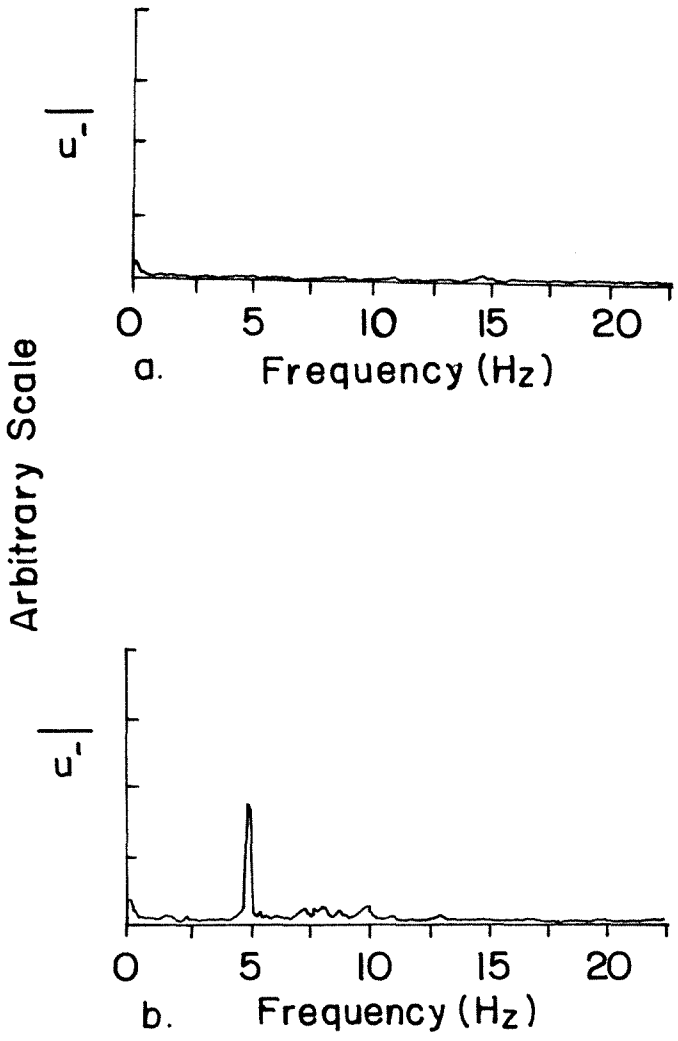

Fig. 2 Power spectrum of the velocity fluctuations.
(a) In the absence of the model.
(b) Typical cavity flow oscillation.

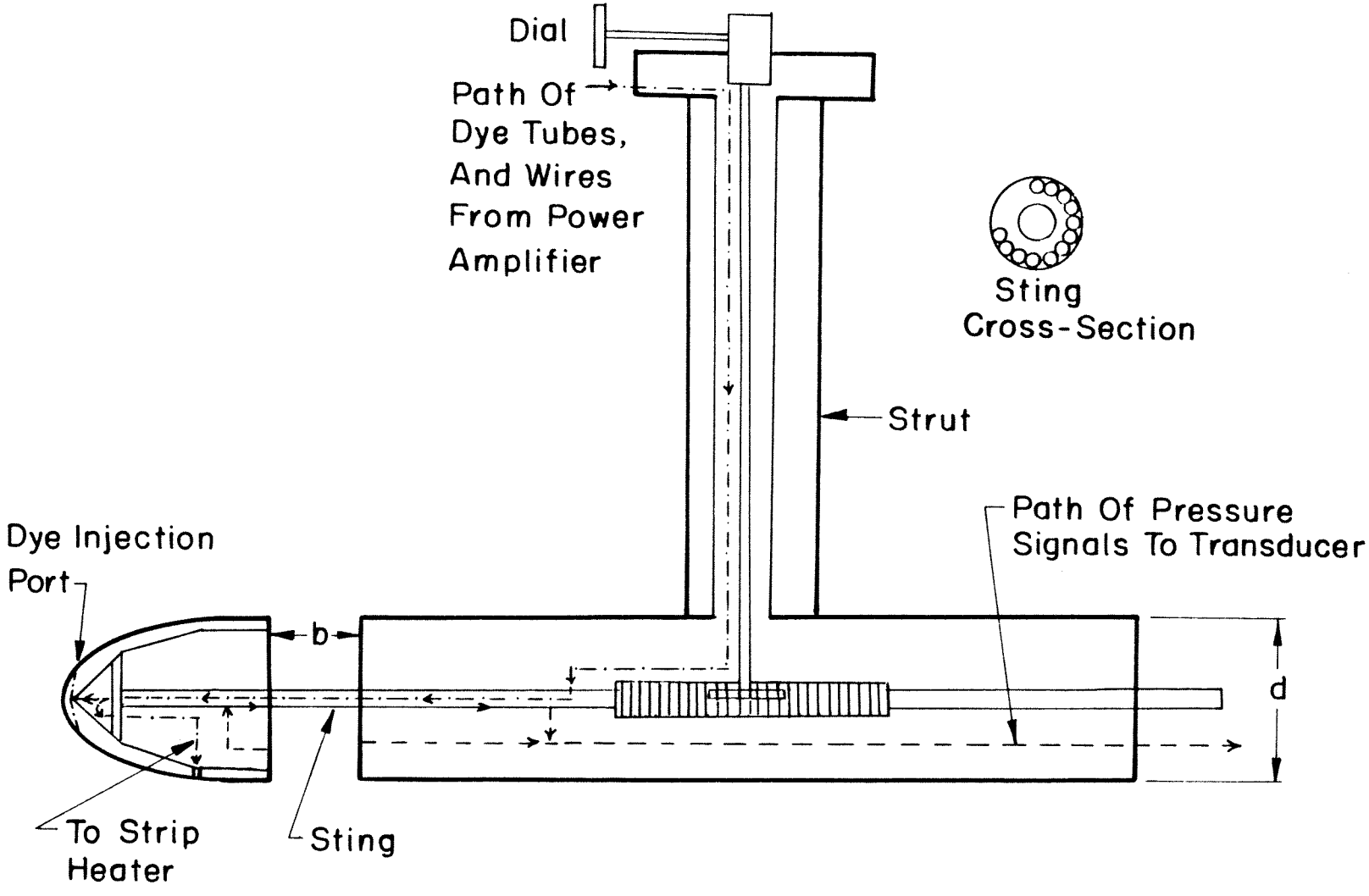

Fig. 3 Schematic of the experimental model.

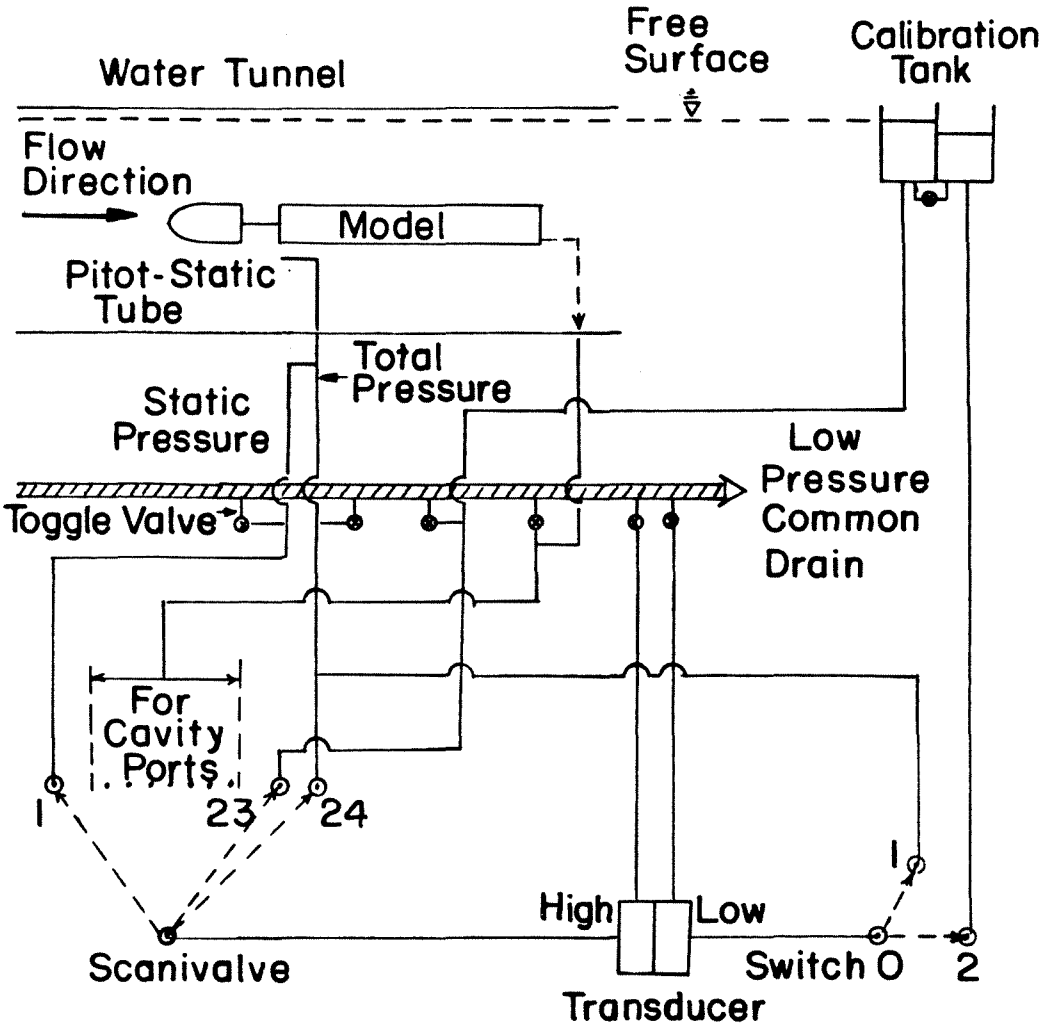

Table 1

Position of Switch 0	Position of Scanivalve	Type of Operation
1	24	Null Check
2	23	Calibration
1	1	Dynamic Pressure P_T-P_s
1	Any other Position	P_T-P_c

Fig. 4 Schematic of the pressure sensing set-up and operational table of the valves (Table 1)

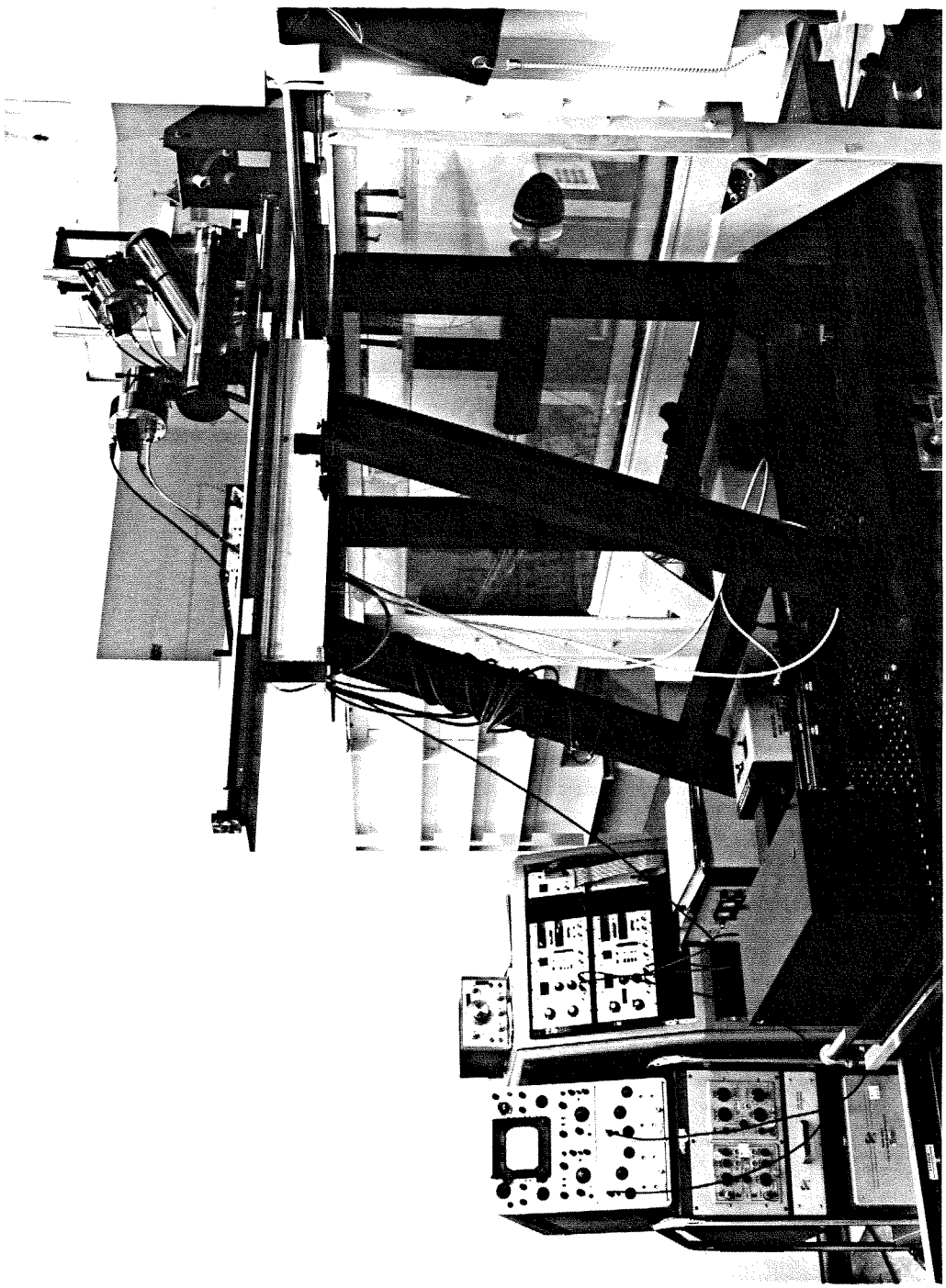

Fig. 5 Photograph of the laser Doppler velocimeter set-up and the test section.

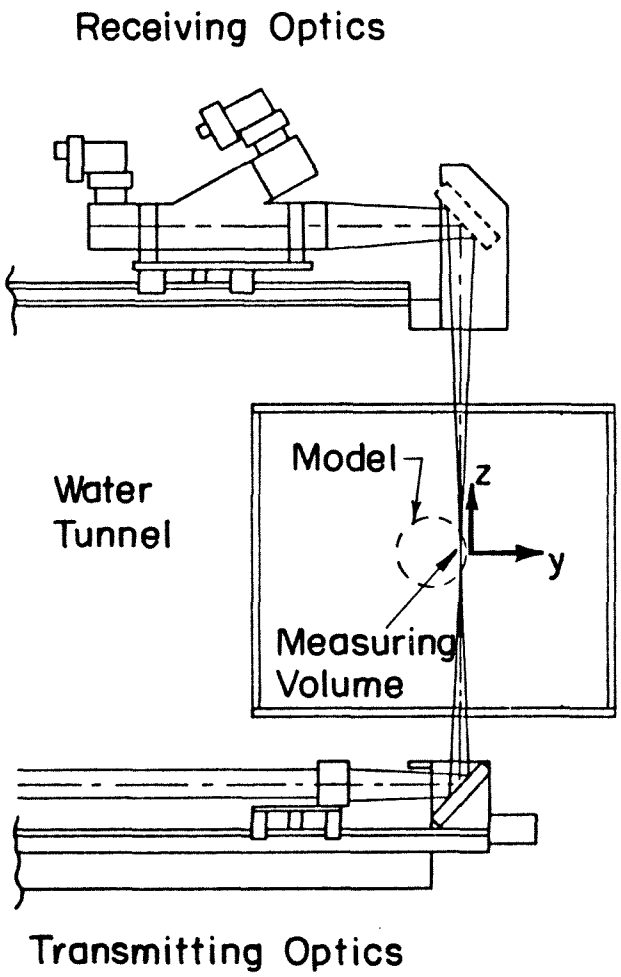

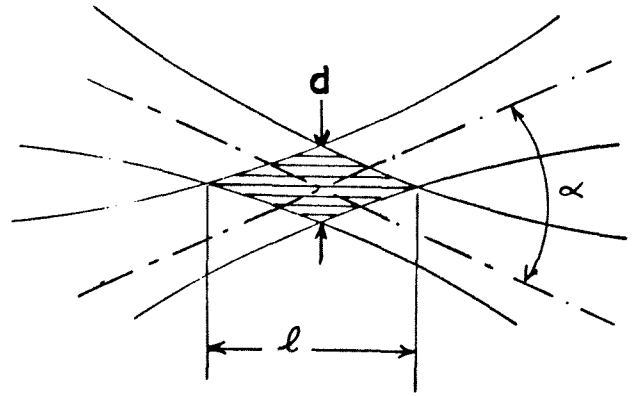

Table 2

Lens focal length, f	= 598 mm
Beams crossing angle, α	= 4.72°
Beams diameter, D_e-2	= 1.3 mm
Focal volume length*, ℓ	= 7.3 mm
Focal volume width*, d	= 0.3 mm
Fringe spacing*, d_f	= 6.1 μm
Number of fringes, N_{fr}	= 48

Fig. 6 Relative location of the LDV with respect to the model and characteristics of the measuring volume (Table 2).

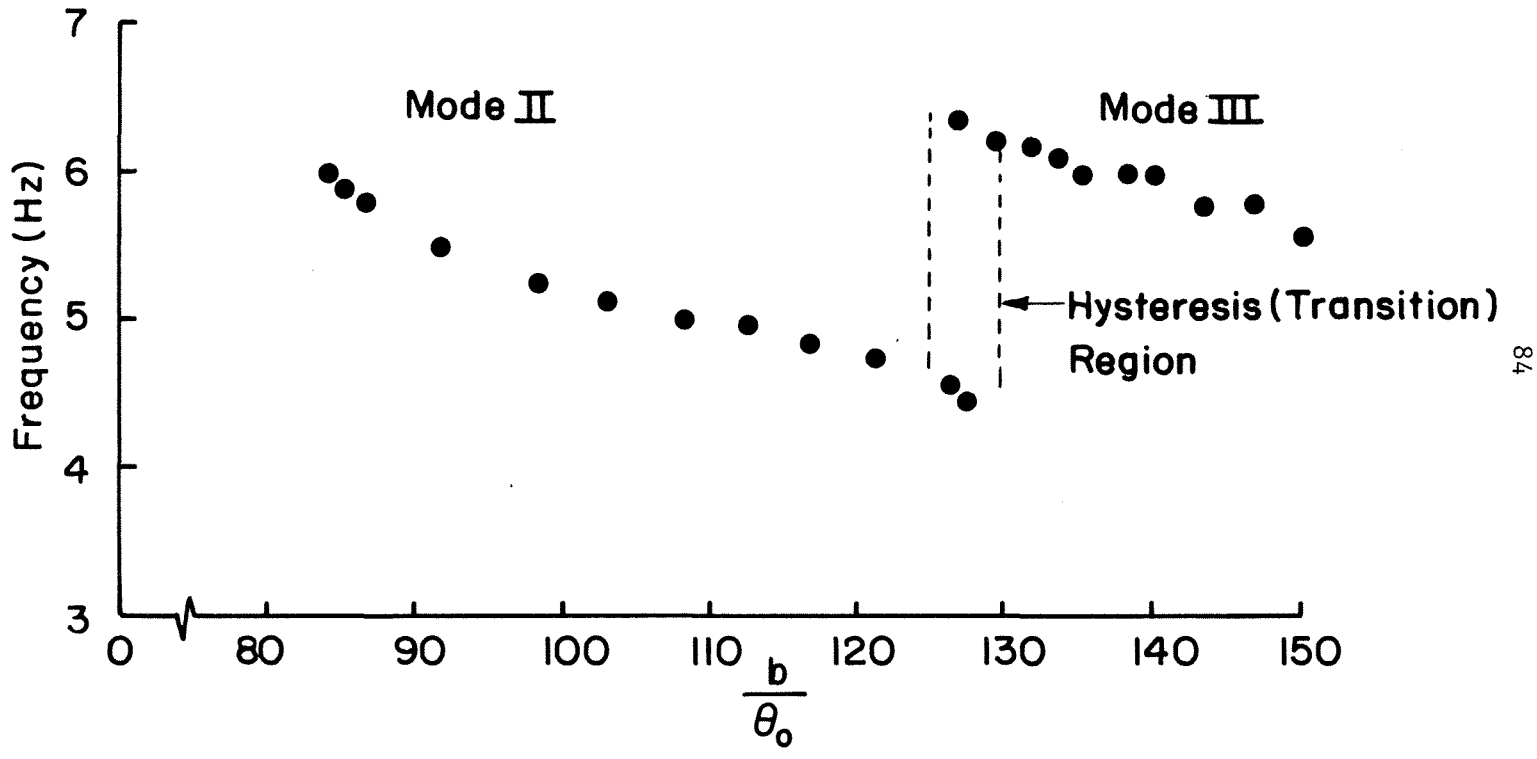

Fig. 7 Frequency variation of cavity shear layer with varying cavity width, constant free stream velocity.

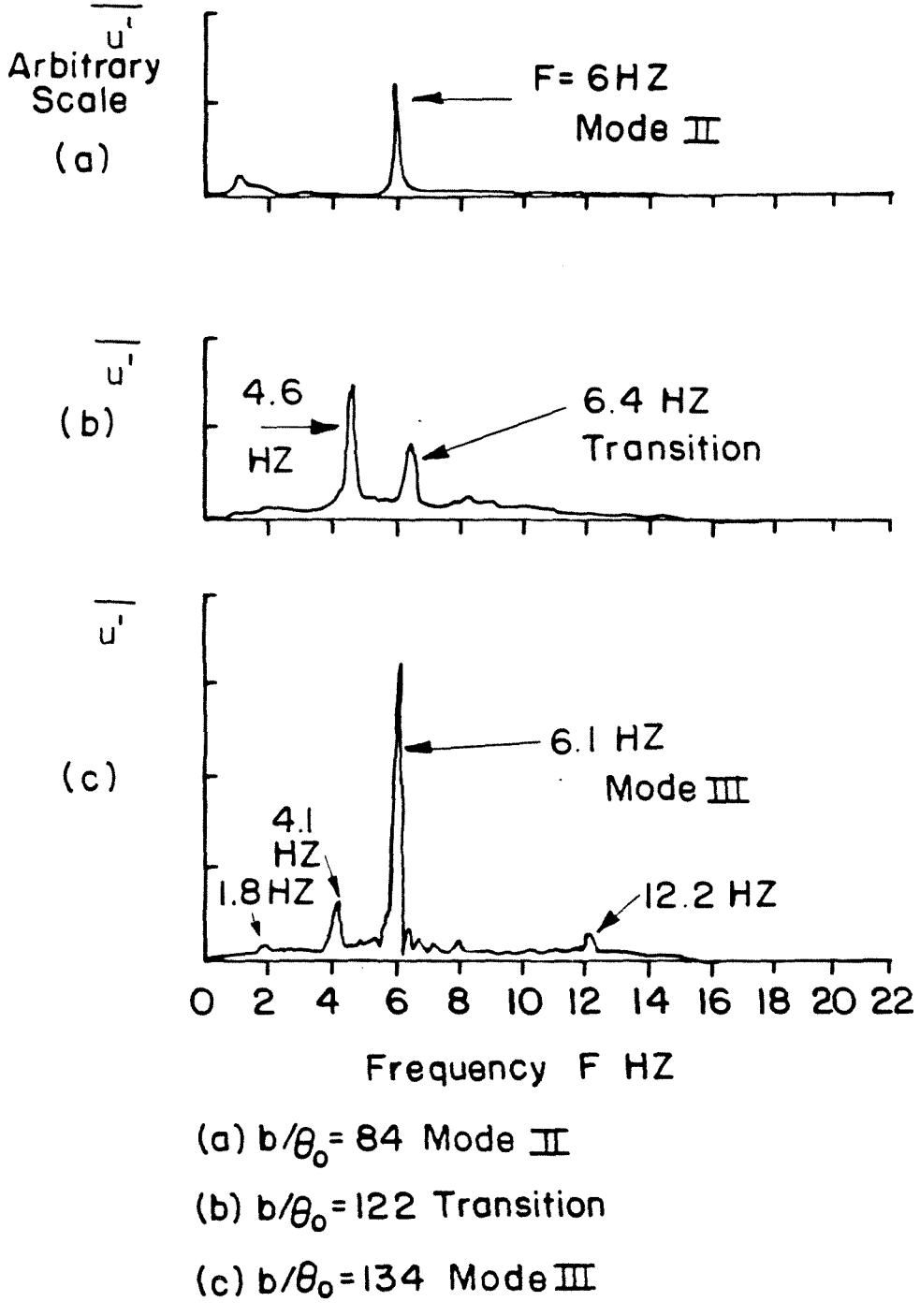

Fig. 8 Velocity fluctuation spectra for increasing cavity width from Mode II to Mode III.

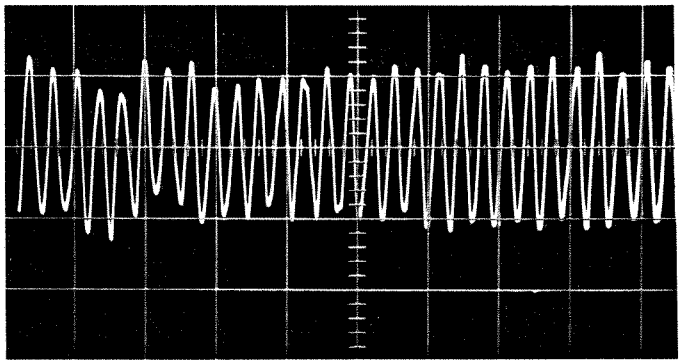

(a) Mode II, F = 6 Hz, vertical scale .02 volt/div

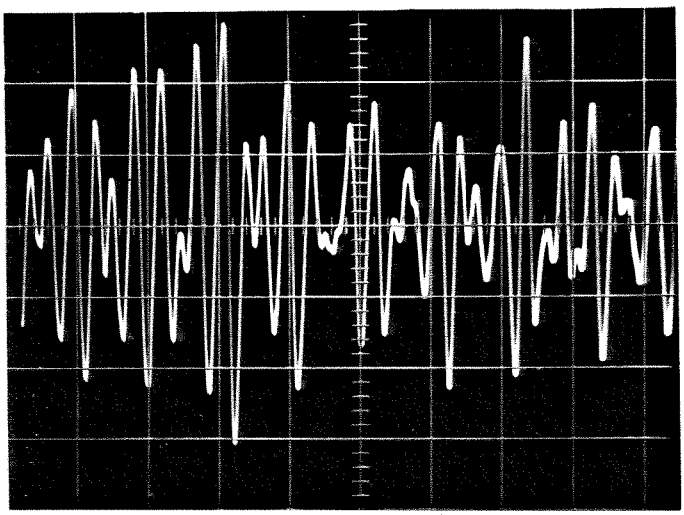

(b) Transition F = 4.6 Hz Mode II
F = 6.4 Hz Mode III, Vertical scale .02 volt/div

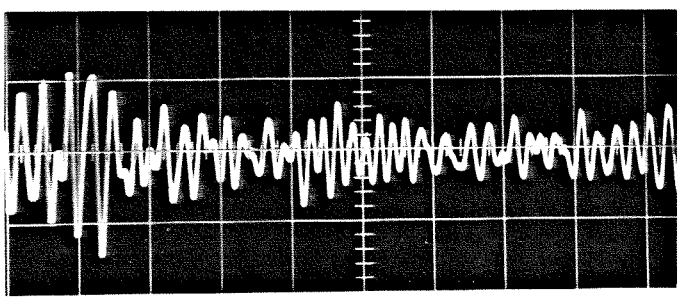

(c) Mode III F = 6 Hz vertical scale .04 volt/div

Fig. 9 Oscilloscope traces of cavity shear layer oscillations.

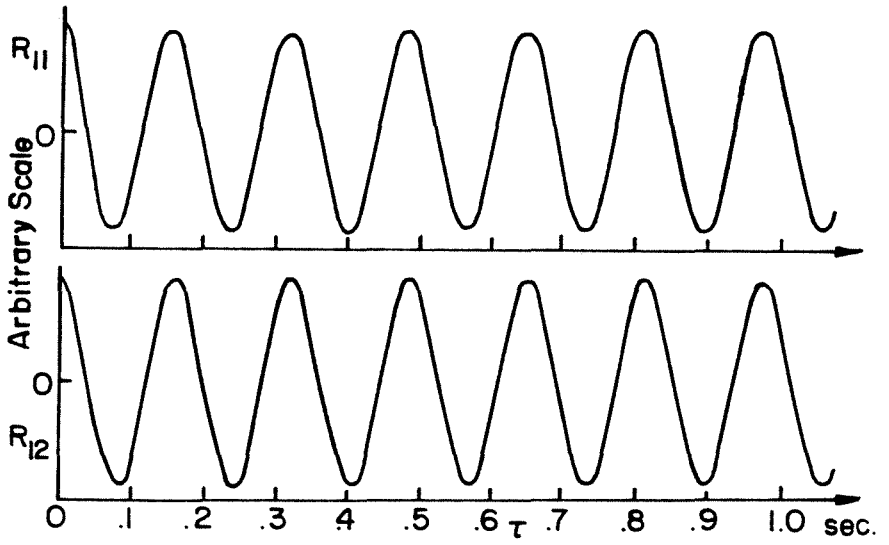

Fig. 10 Correlation test.

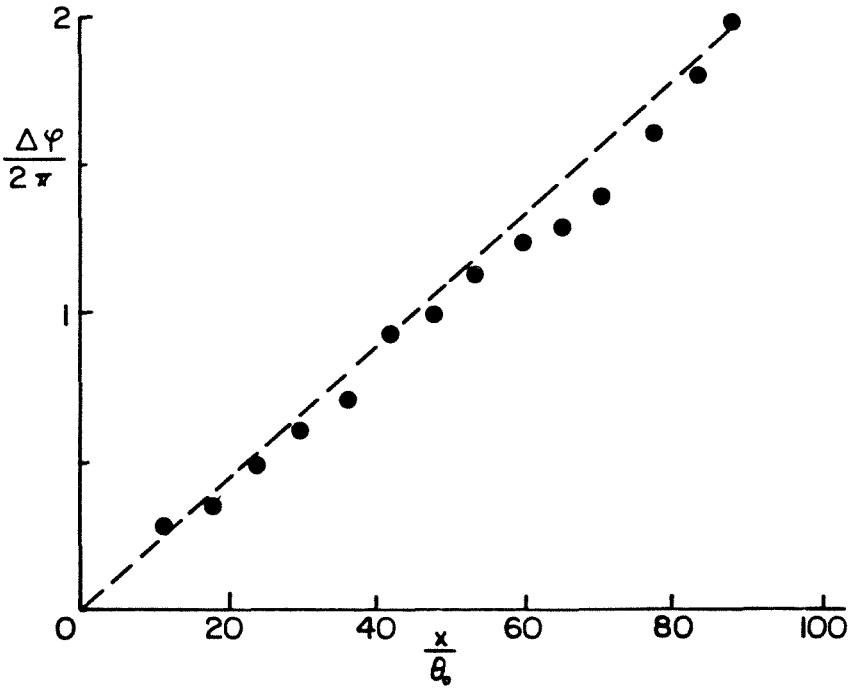

Fig.11 Phase angle of various downstream locations for Mode II of the oscillations at $b/\theta_0 = 85$, $F = 5.9$ Hz, $U_e = 23$ cm/sec.

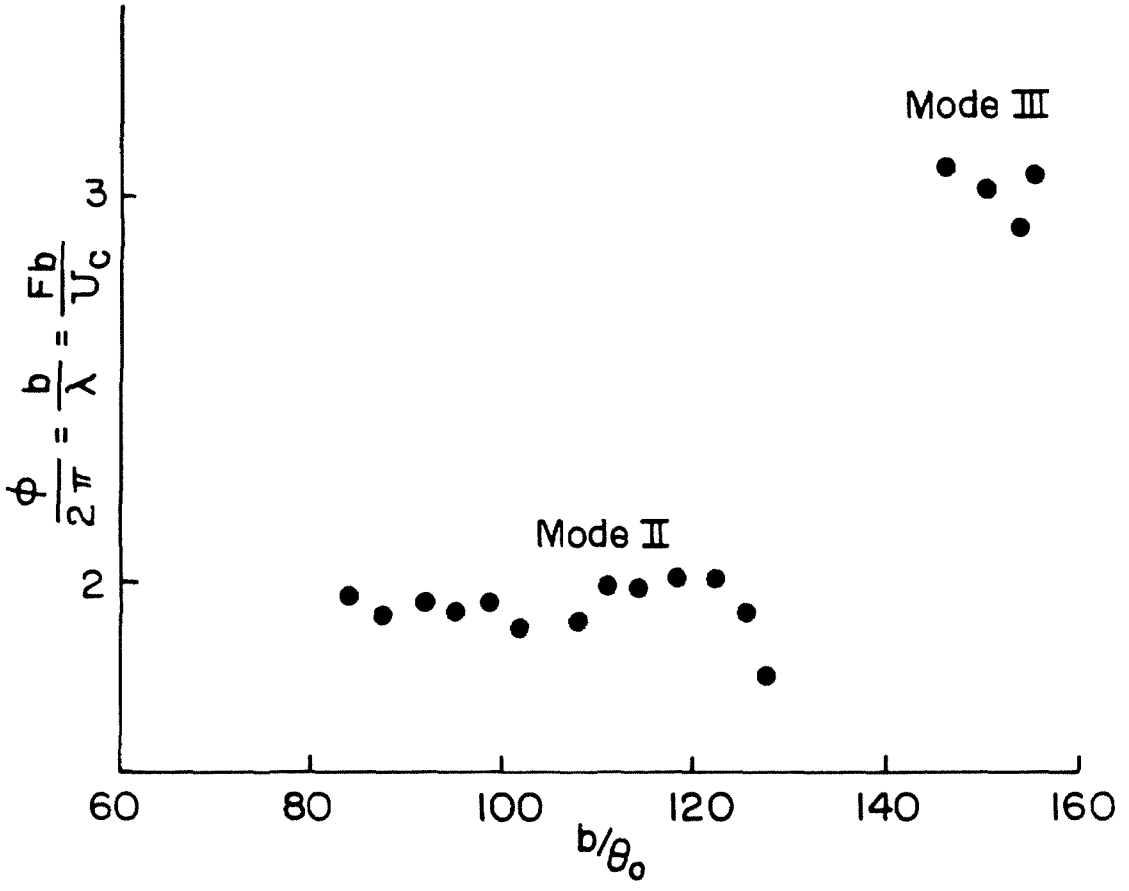

Fig. 12 Overall phase difference between two corners of the cavity for Mode II and III of the cavity flow oscillations.

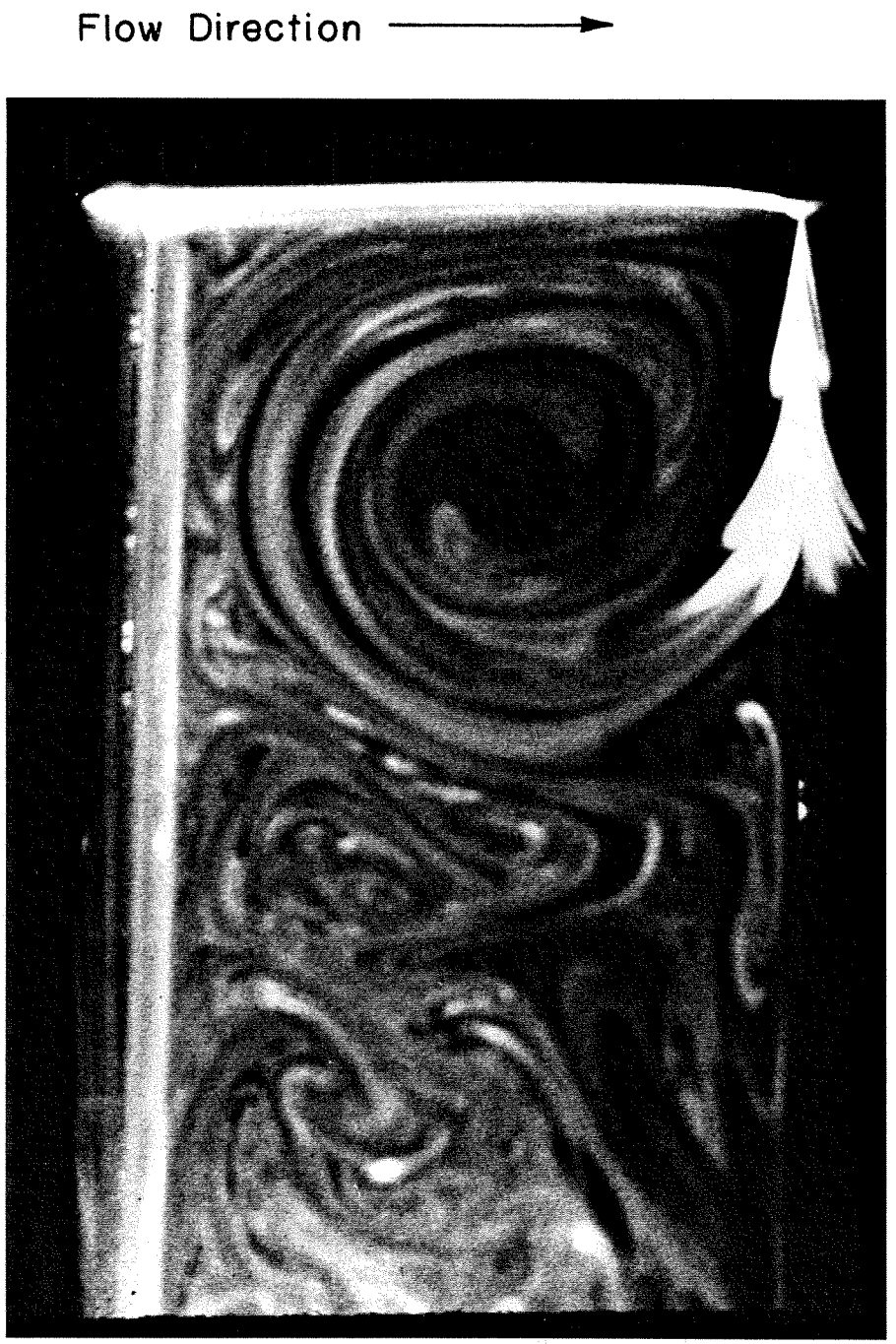

Fig. 13 Flow visualization of the cavity flow in non-oscillating mode; $b/\theta_0 = 66$.

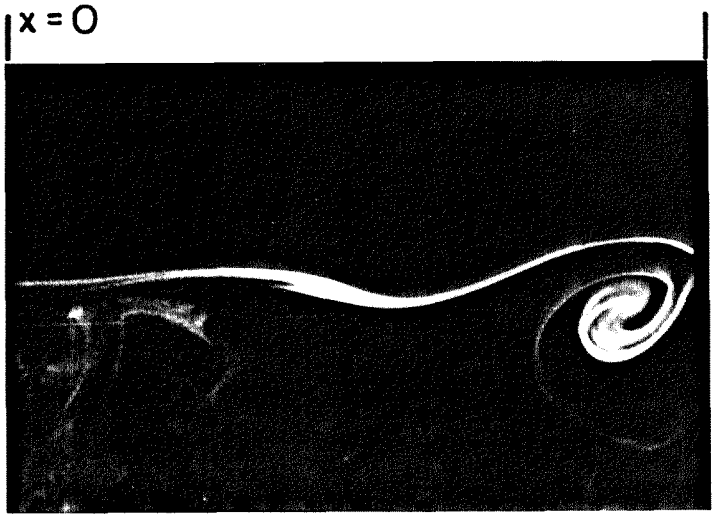

(a) Mode II $b/\lambda = \frac{Fb}{U_c} = 2$

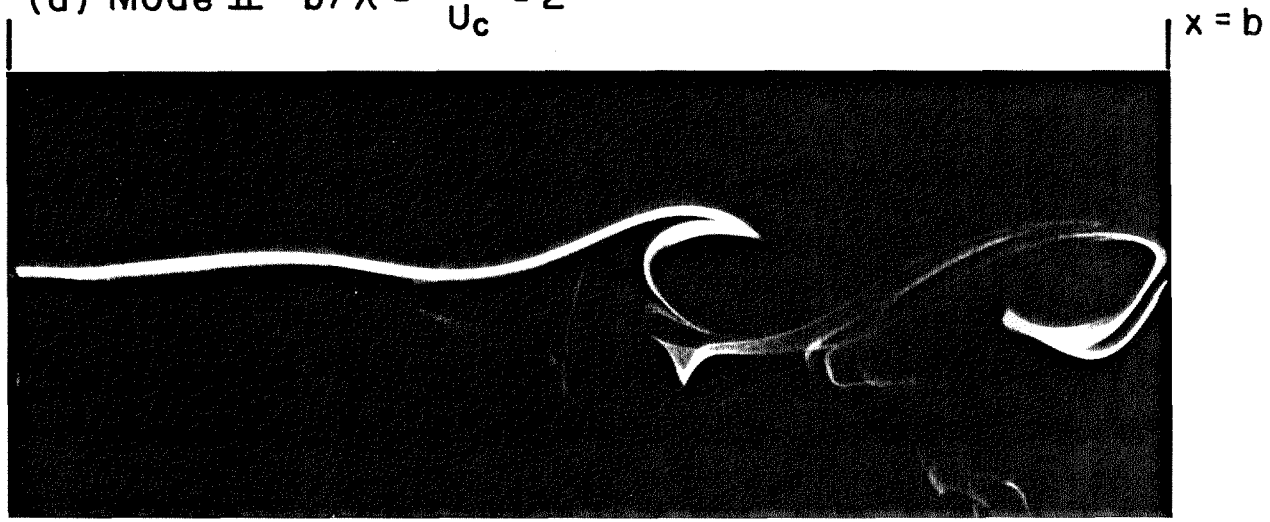

(b) Mode III $b/\lambda = \frac{Fb}{U_c} = 3$

Fig. 14 Flow visualization of the cavity shear layer; flow is frozen at 1/1000 sec.

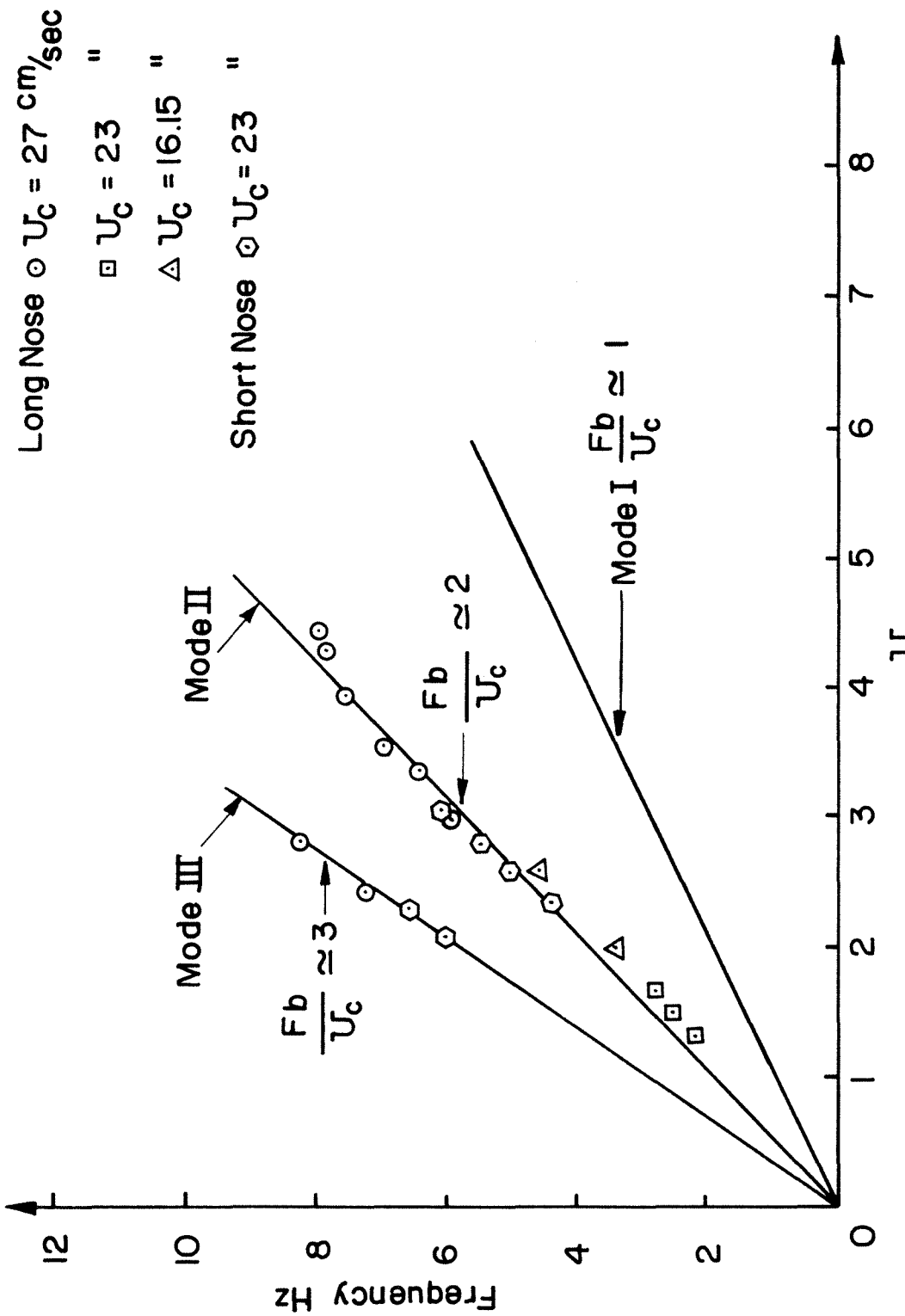

Fig. 15 Frequency variation of the cavity shear layer with $\frac{U_c}{b}$, for different cavity geometries and free stream velocities.

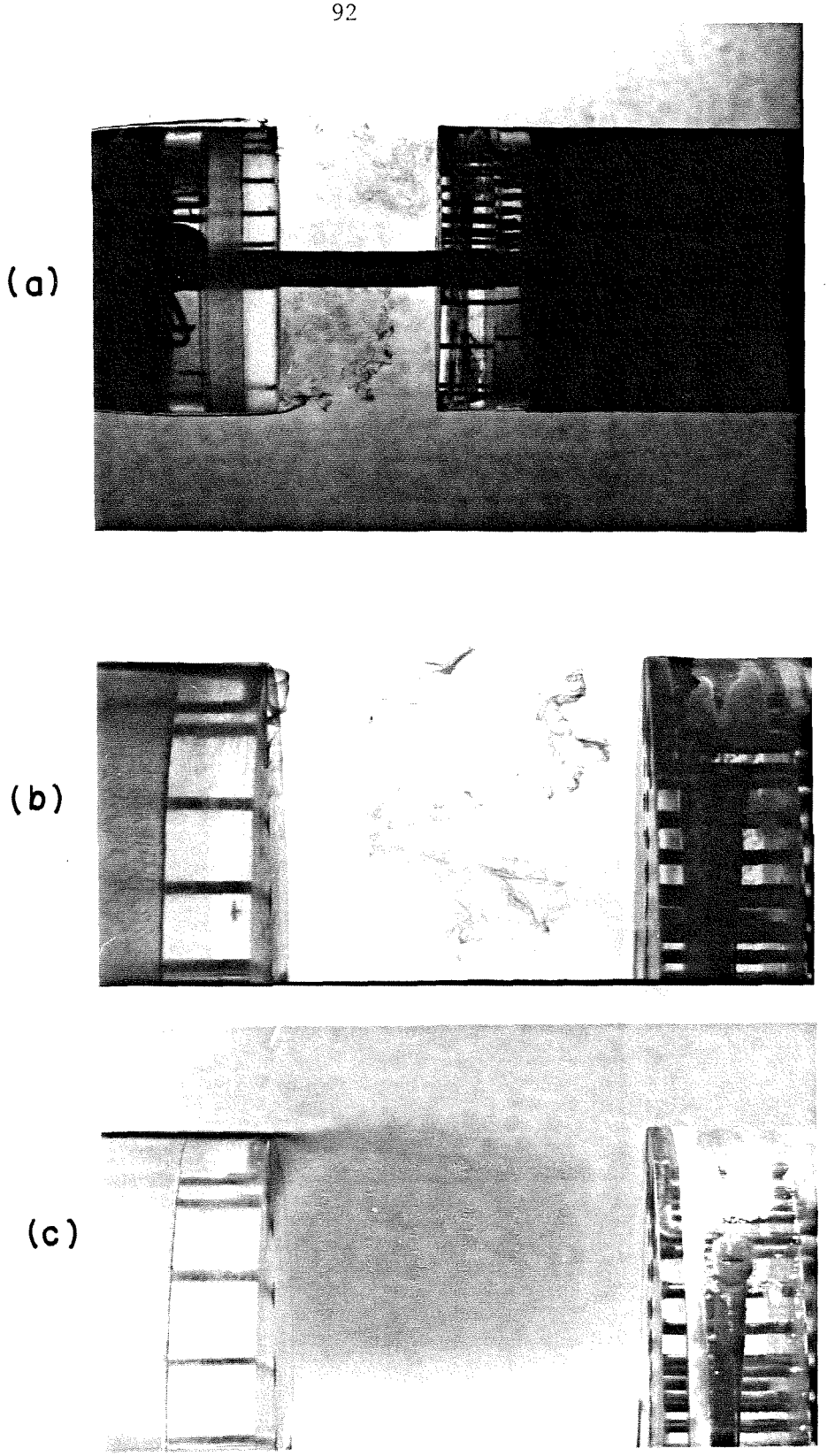

Fig. 16 Flow visualization of the cavity flow; b/θ_0 = 170 wake mode; (a) and (b) 1/1000 sec; (c) 5 sec exposure.

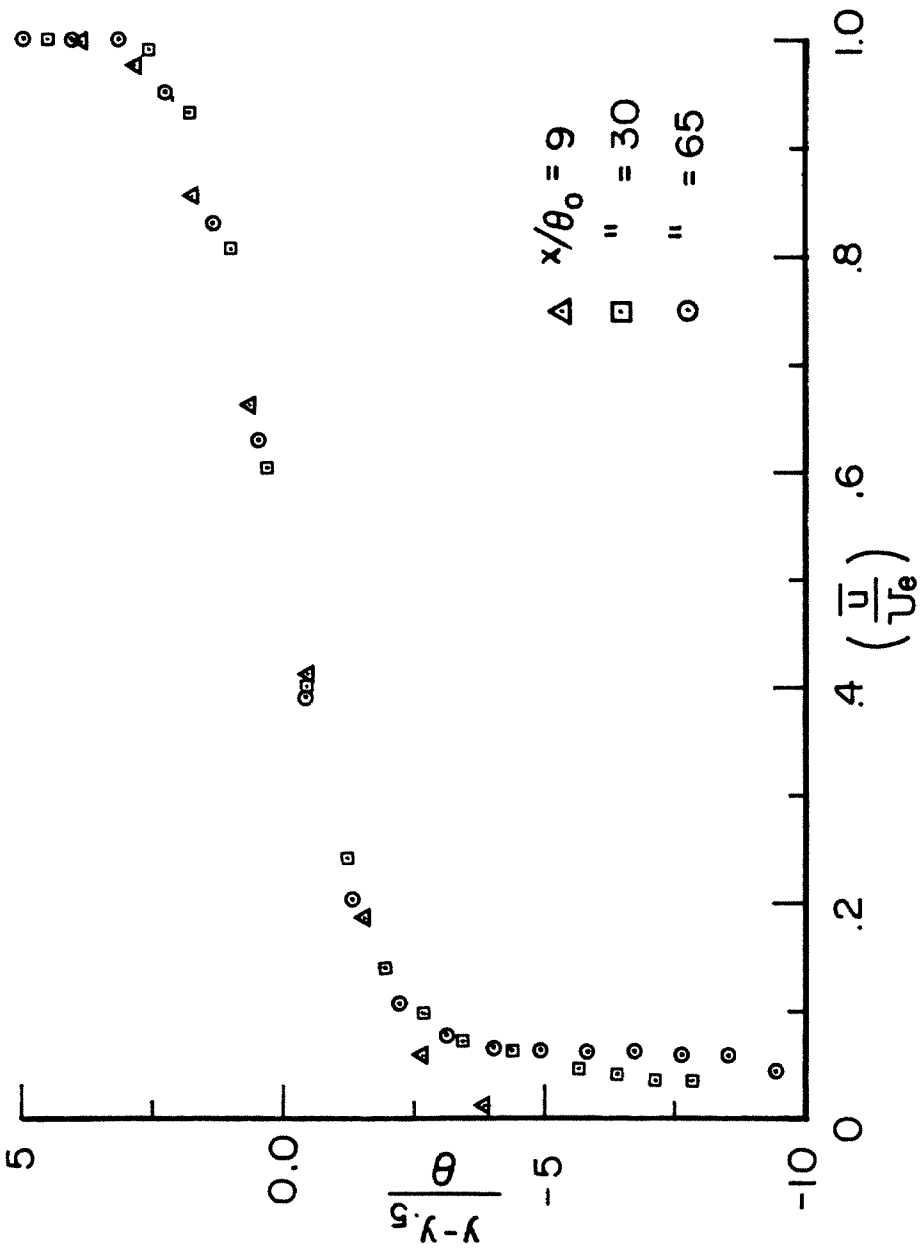

Fig. 17 Non-dimensional mean streamwise velocity profiles; $b/\theta_0 = 85$, F = 5.9 Hz, Mode II.

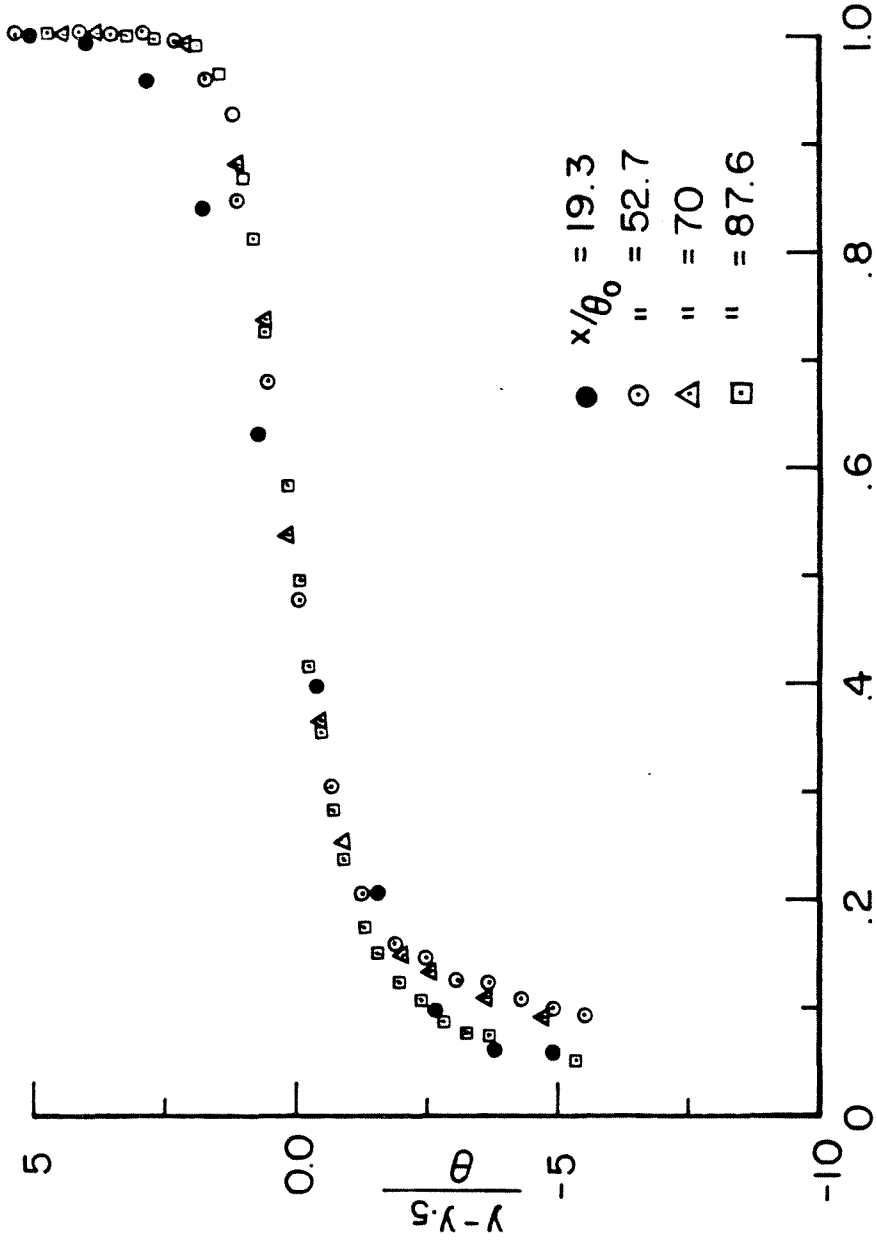

Fig. 18 Non-dimensional mean streamwise velocity profiles; $b/\theta_0 = 103$, F = 5.1 Hz, Mode II.

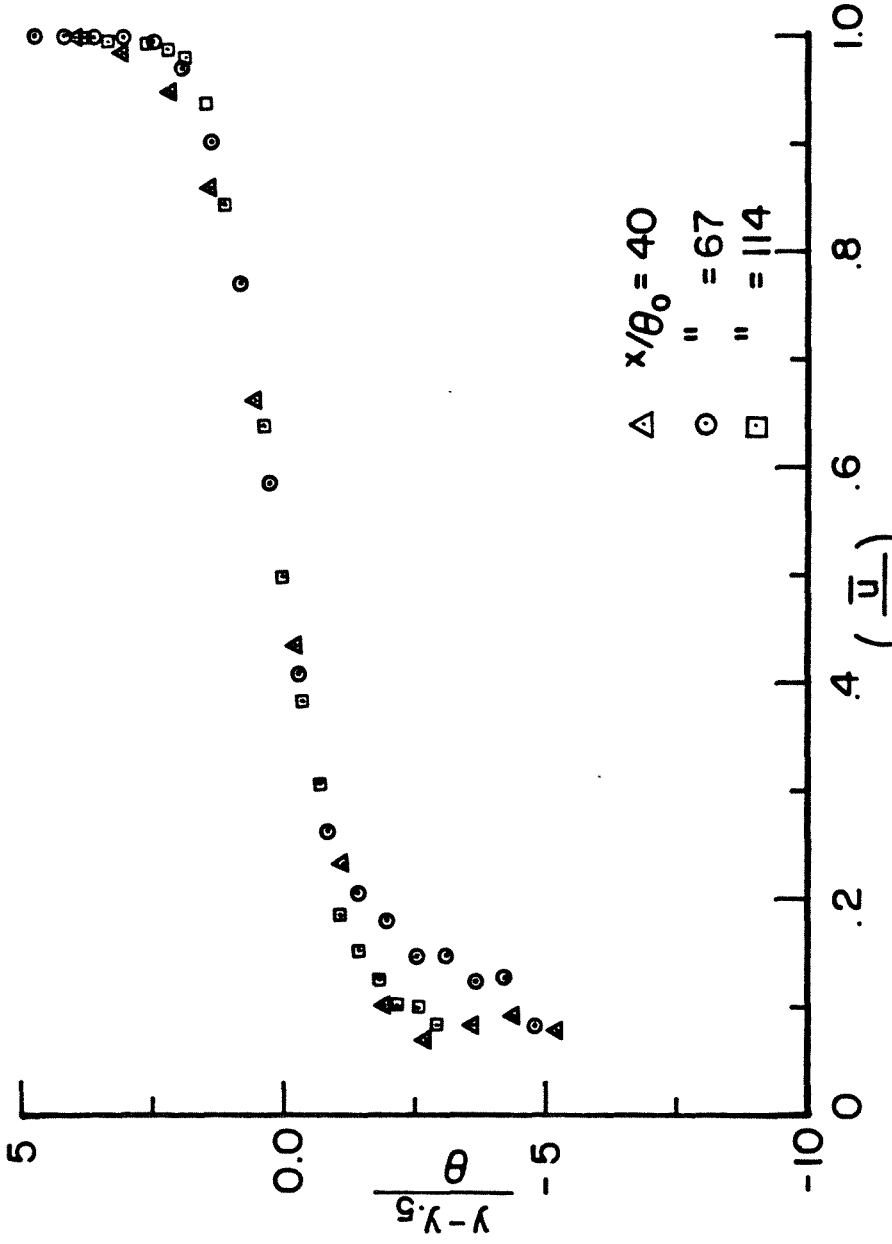

Fig. 19 Non-dimensional mean streamwise velocity profiles; $b/\theta_0 = 130$, F = 6 Hz, Mode III.

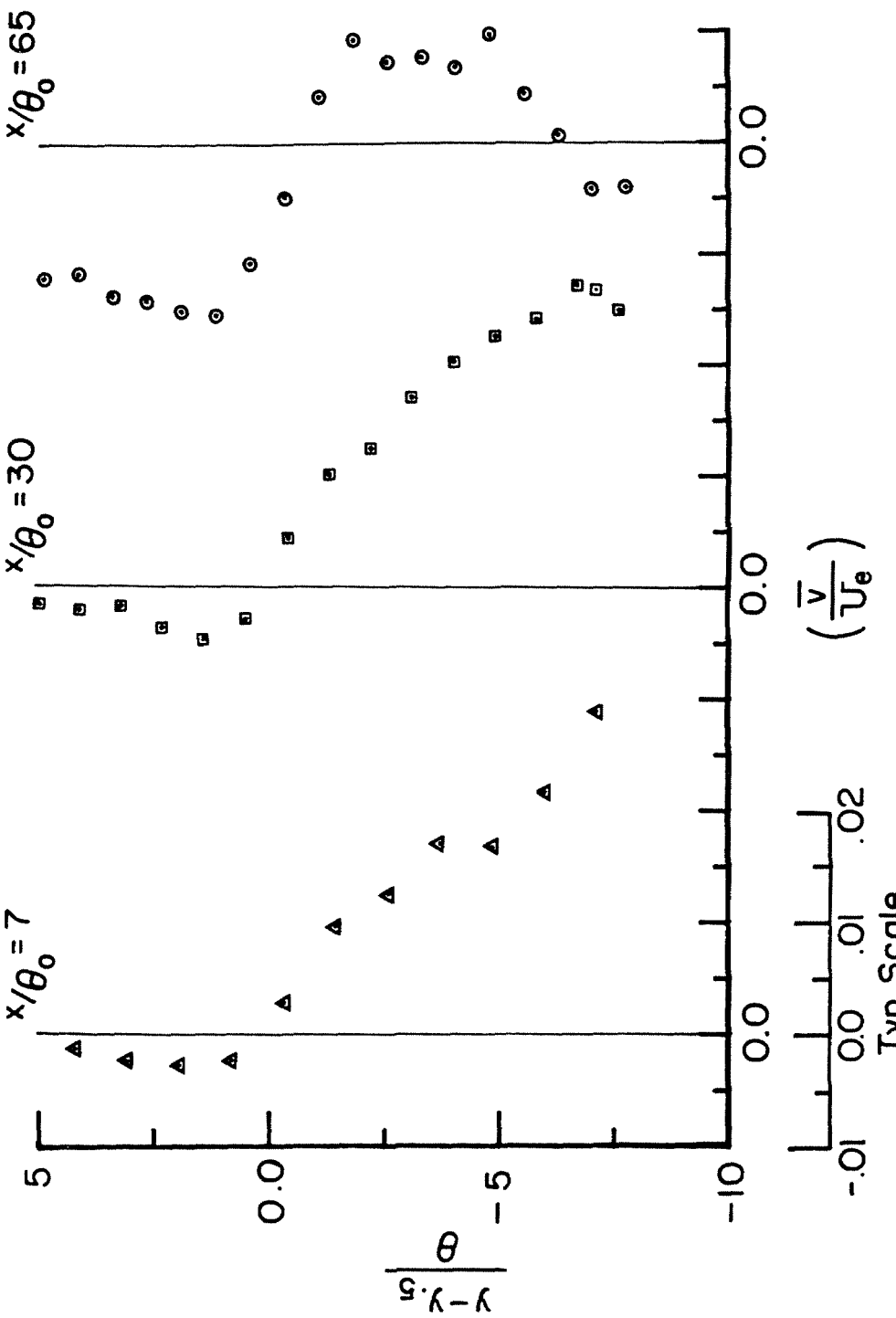

Fig. 20 Non-dimensional mean transverse velocity profiles; $b/\theta_0 = 85$, F = 5.9 Hz, Mode II.

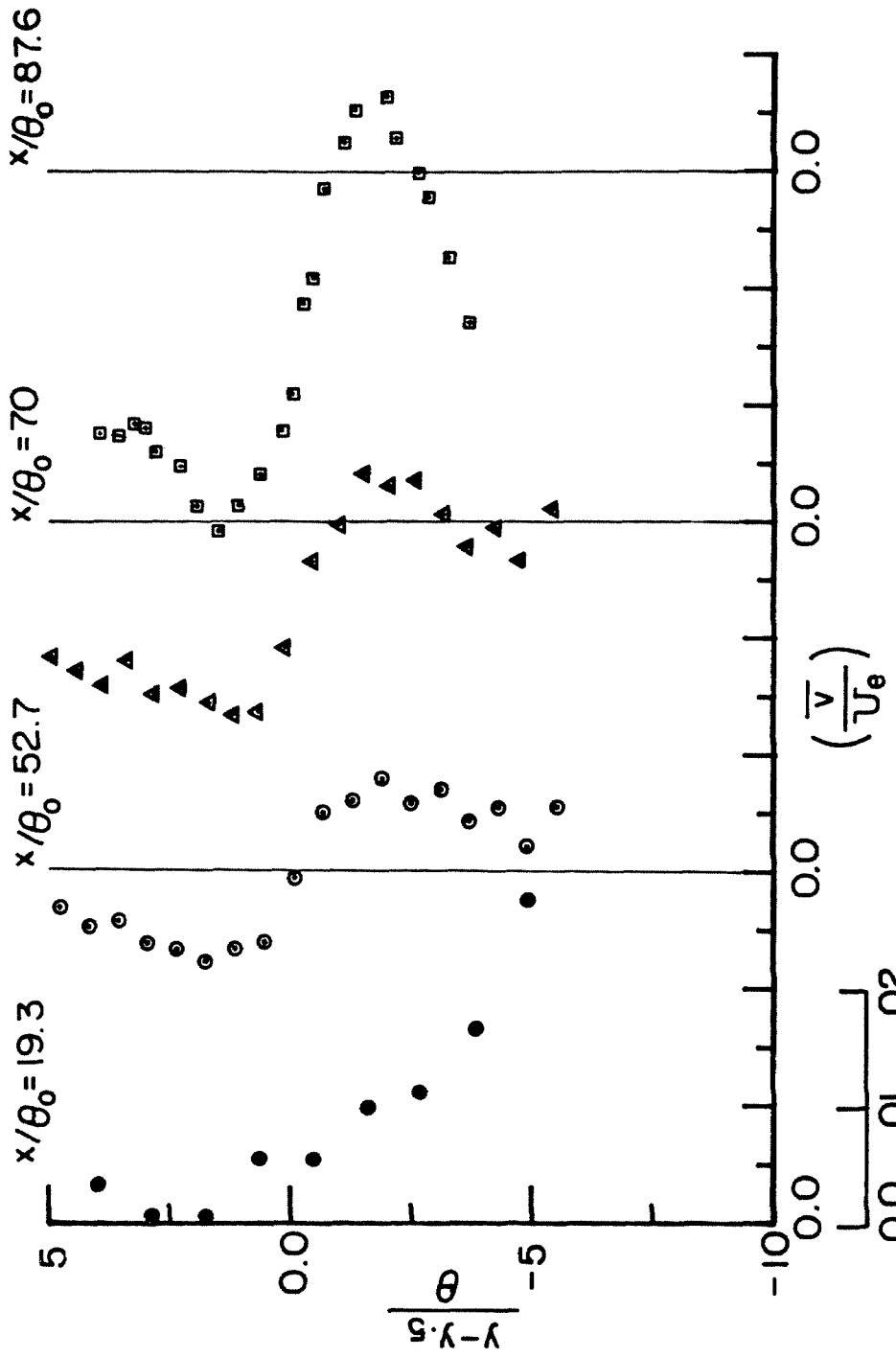

Fig. 21 Non-dimensional mean transverse velocity profiles; $b/\theta_0 = 103$, F = 5.1 Hz, Mode II.

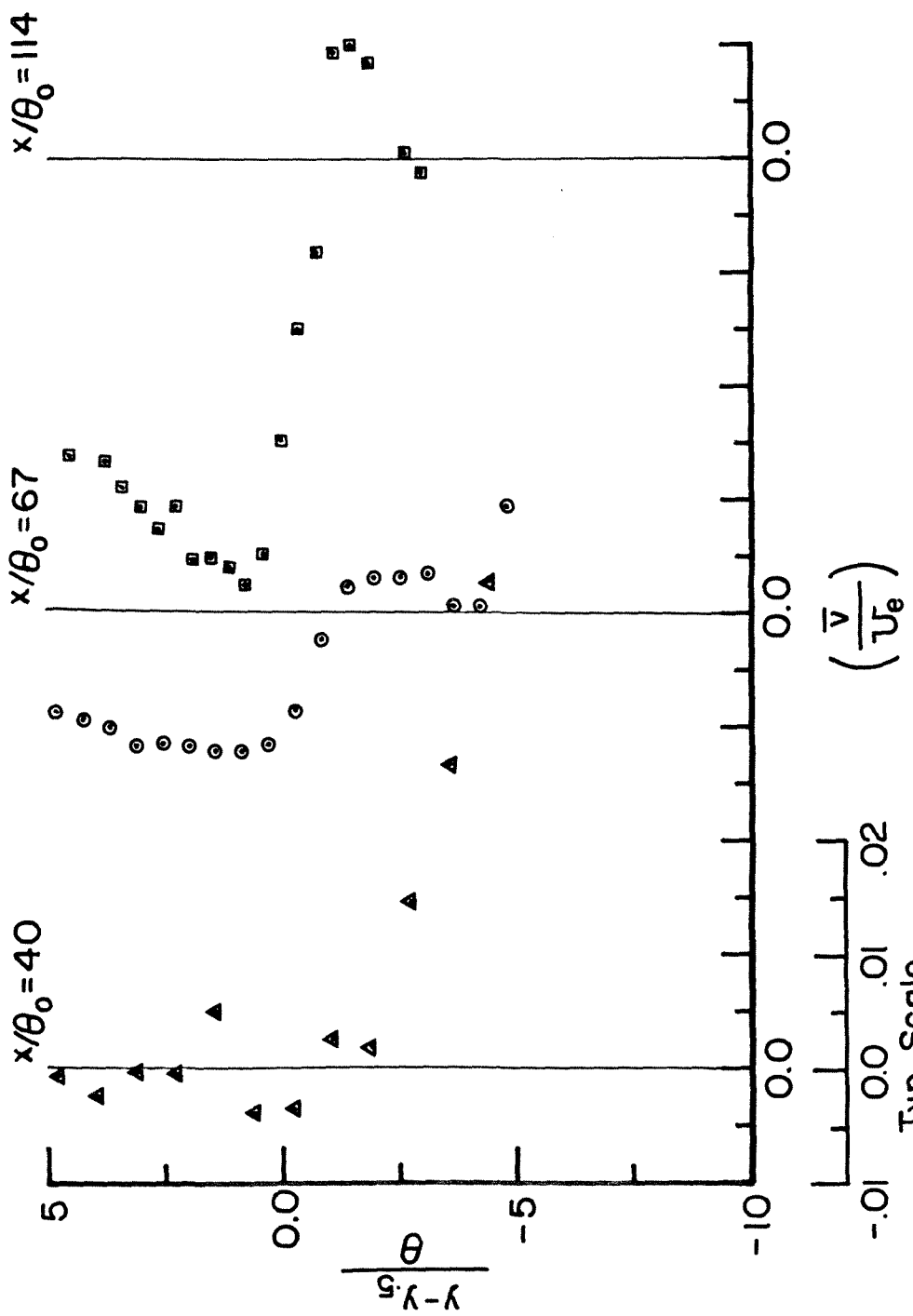

Fig. 22 Non-dimensional mean transverse velocity profiles; b/θ_0 = 130, F = 6 Hz, Mode III.

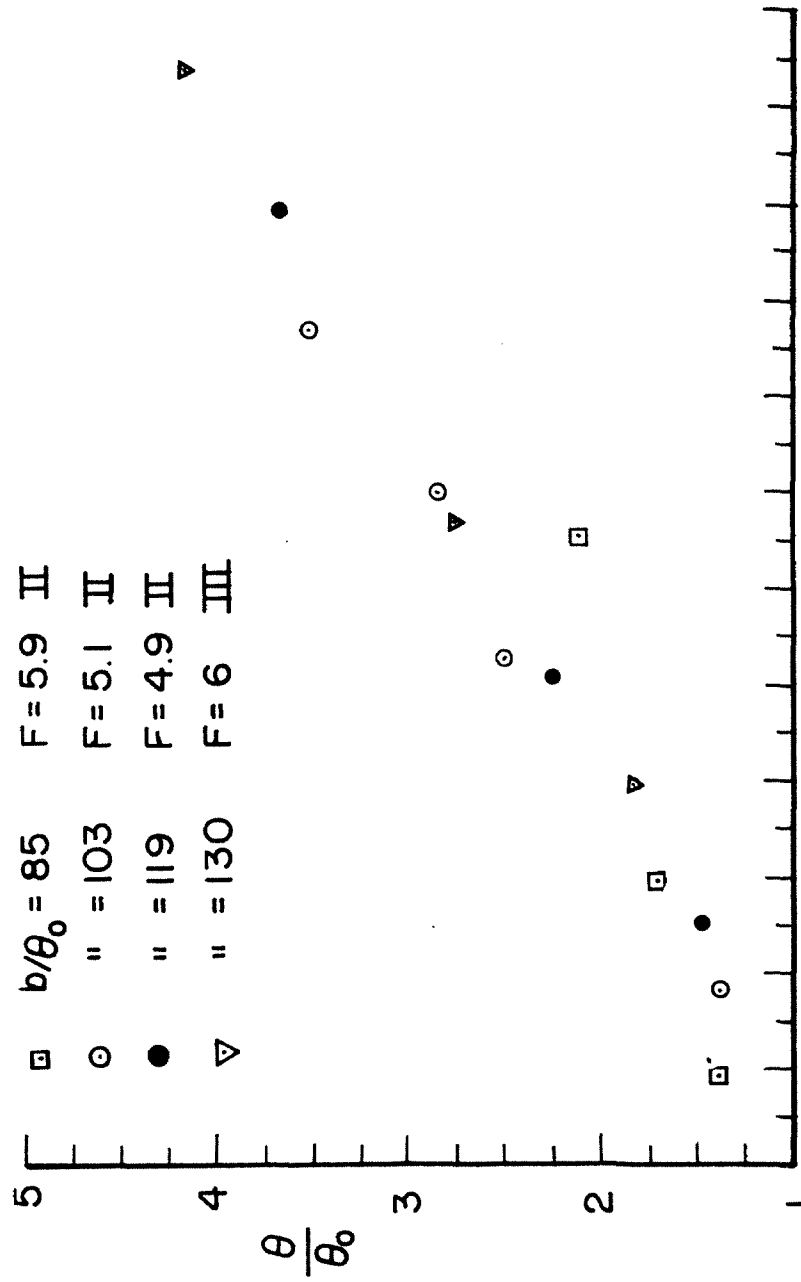

Fig. 23 Non-dimensional momentum thickness growth with streamwise distance.

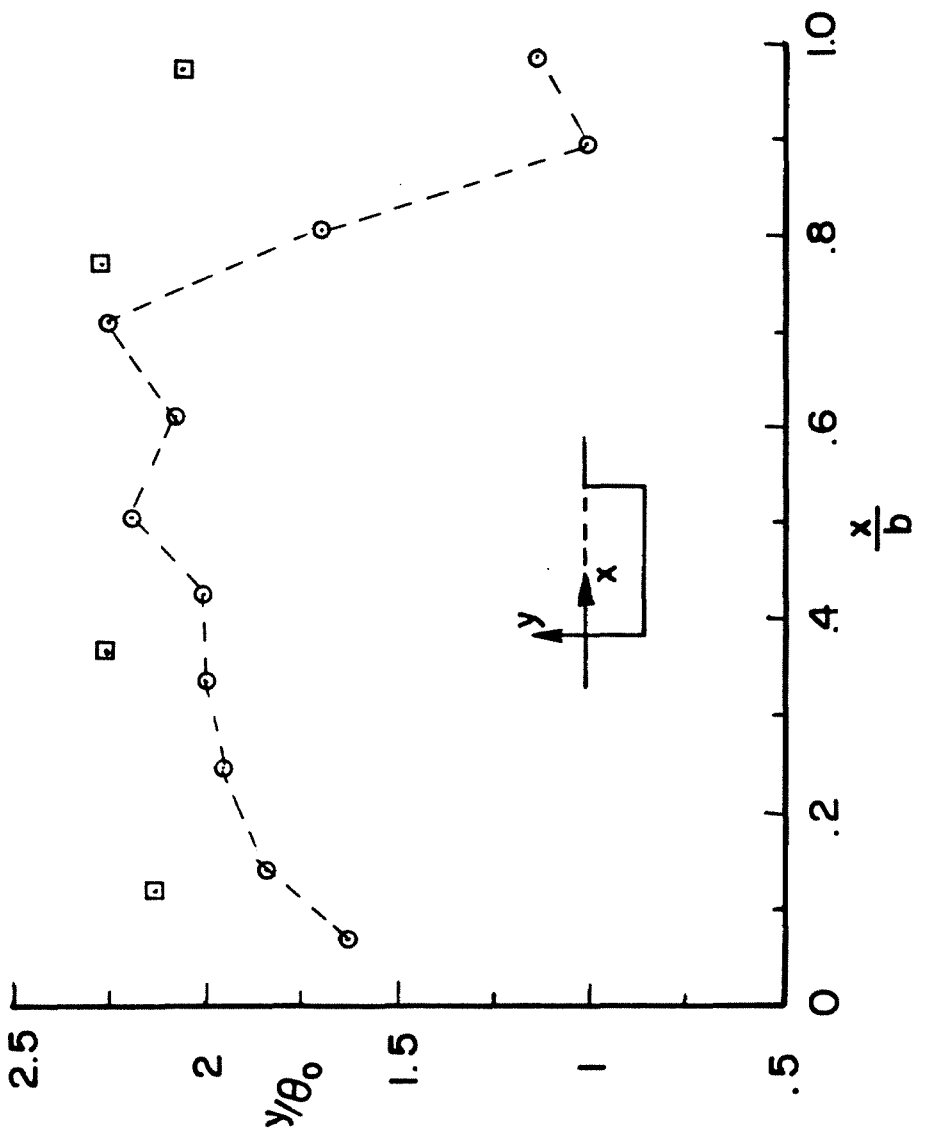

Fig. 24 Locus of points $(y_{.5})$ where $\bar{u}/U_e = .5$; ⊡ $b/\theta_0 = 85$, ⊙ $b/\theta_0 = 103$.

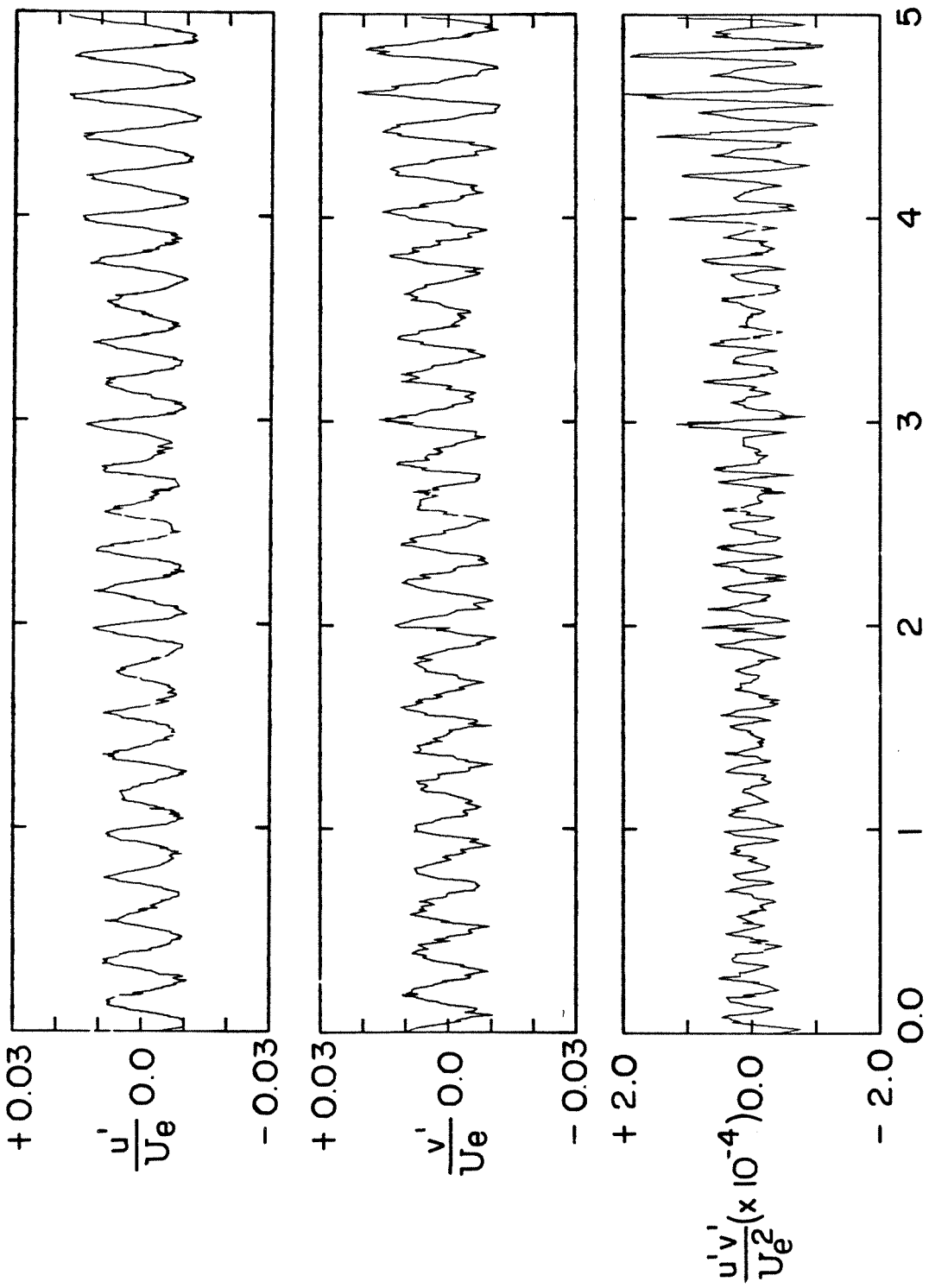

Fig. 25 Time traces of velocity fluctuations and their respective correlation.

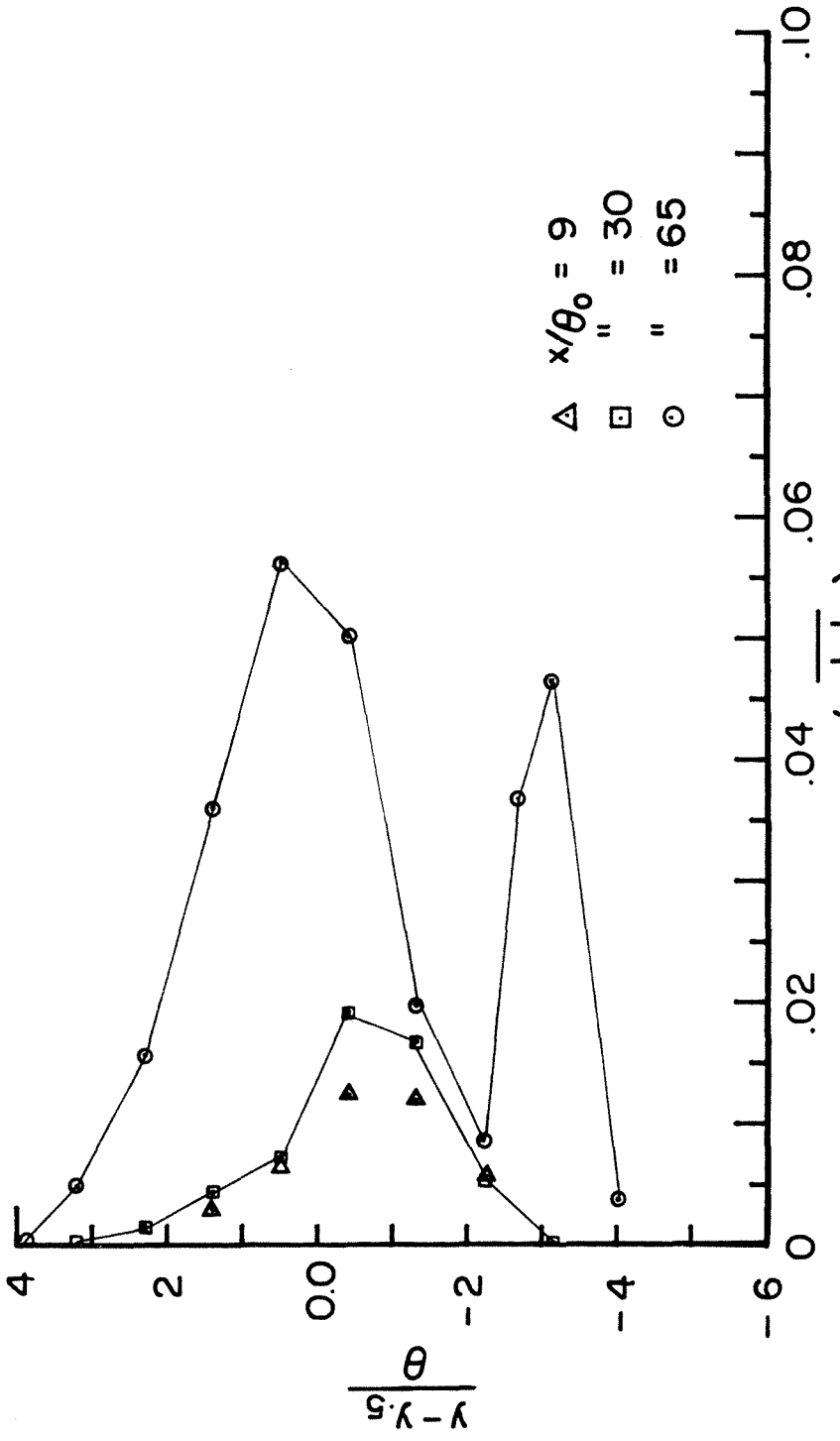

Fig. 26 Shear stress profiles; $b/\theta_0 = 85$, F = 5.9 Hz, Mode II.

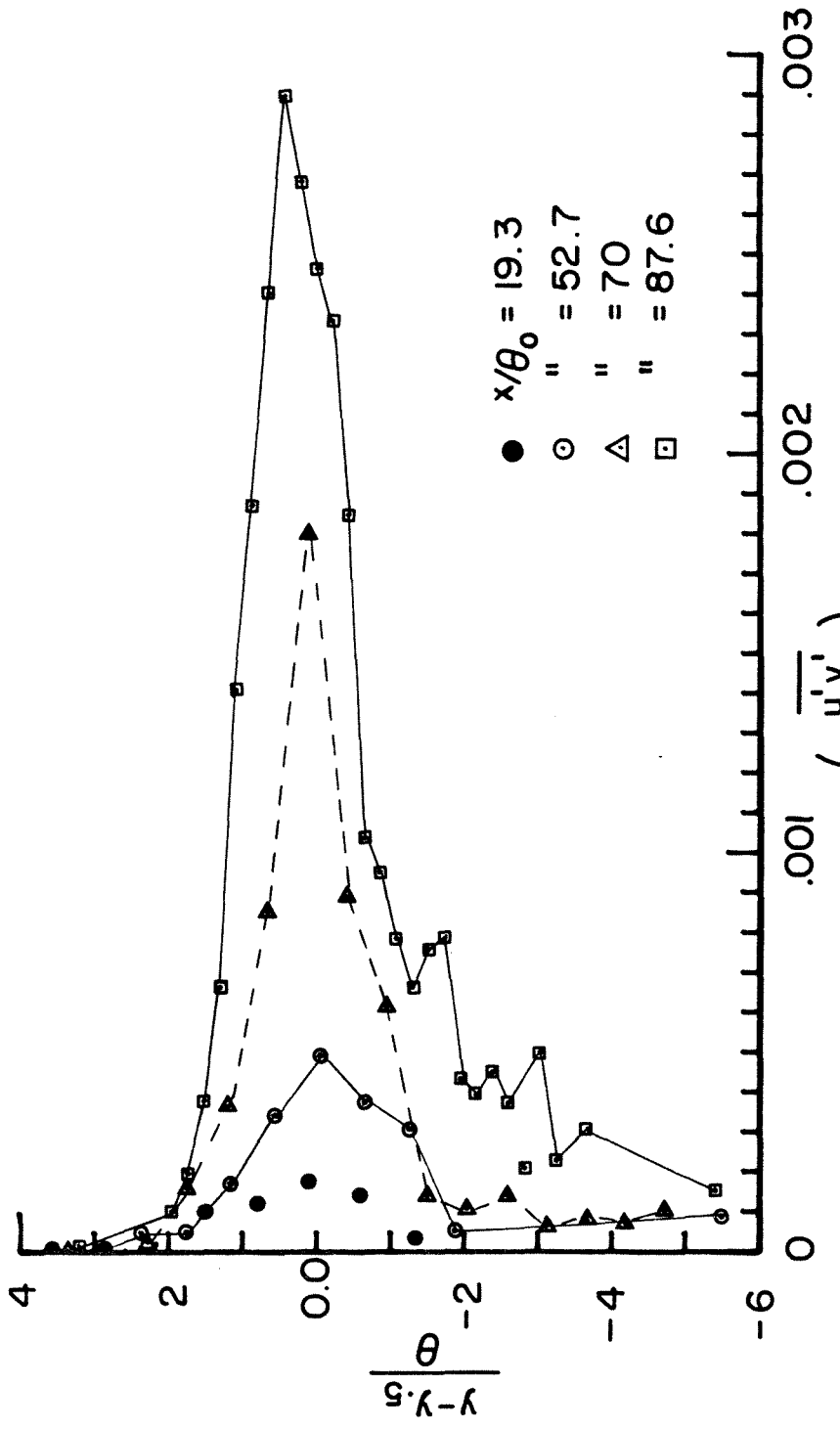

Fig. 27 Shear stress profiles; b/θ_0 103, F = 5.1 Hz, Mode II.

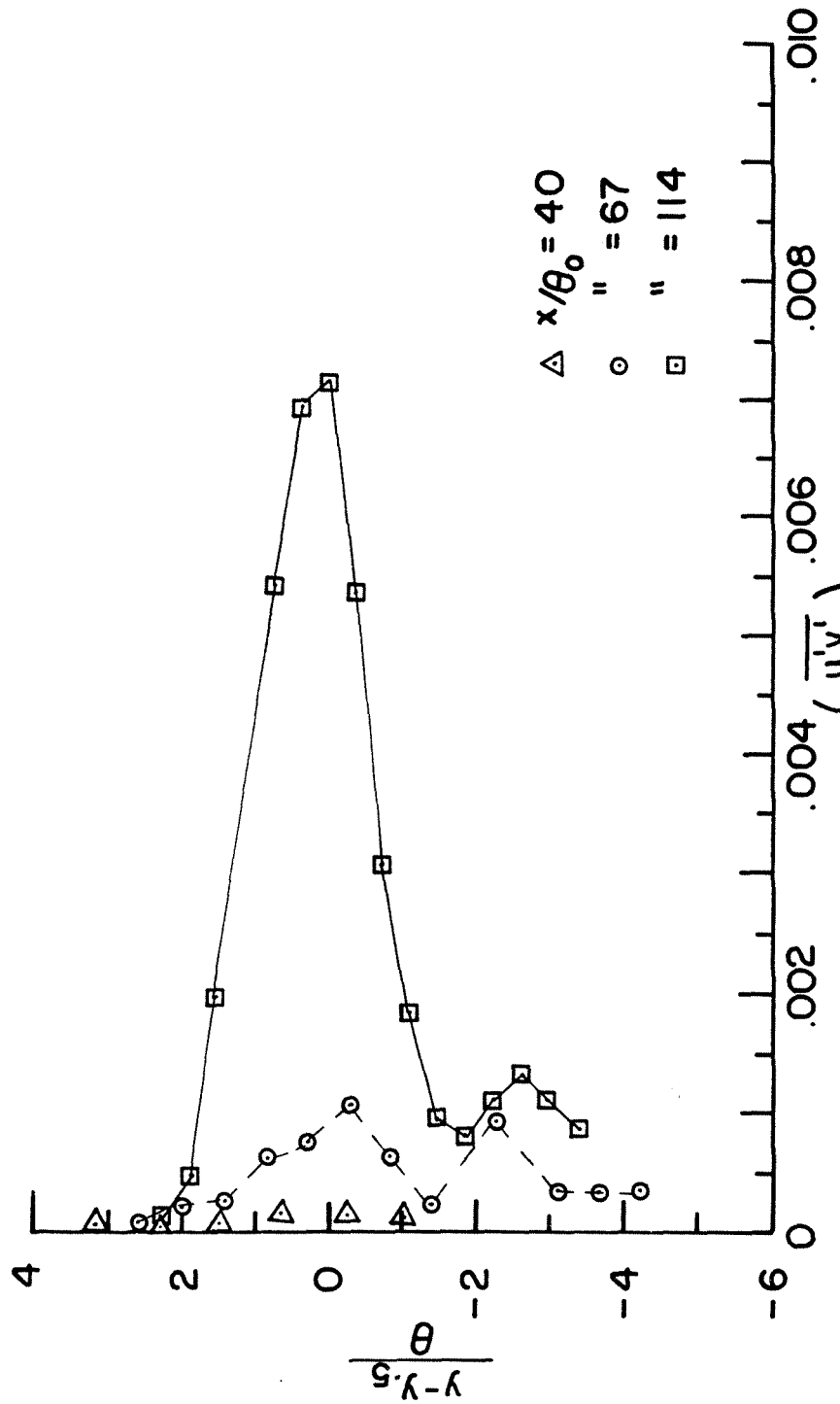

Fig. 28 Shear stress profiles; $b/\theta_0 = 130$, F = 6 Hz, Mode III.

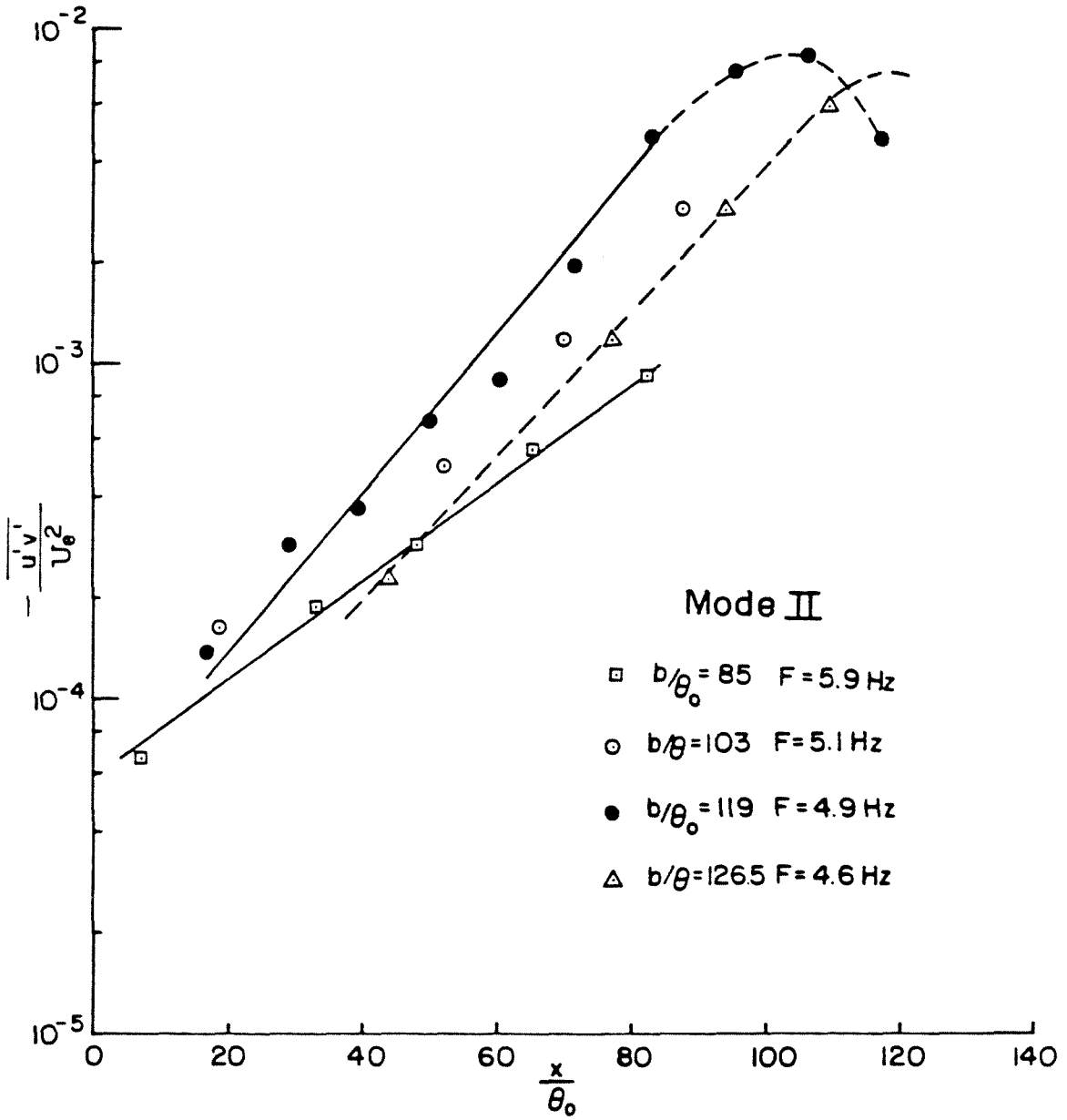

Fig. 29 Growth of the maximum shear stress in the cavity shear layer with downstream distance;
Mode II, $\frac{Fb}{U_c} \simeq 2$.

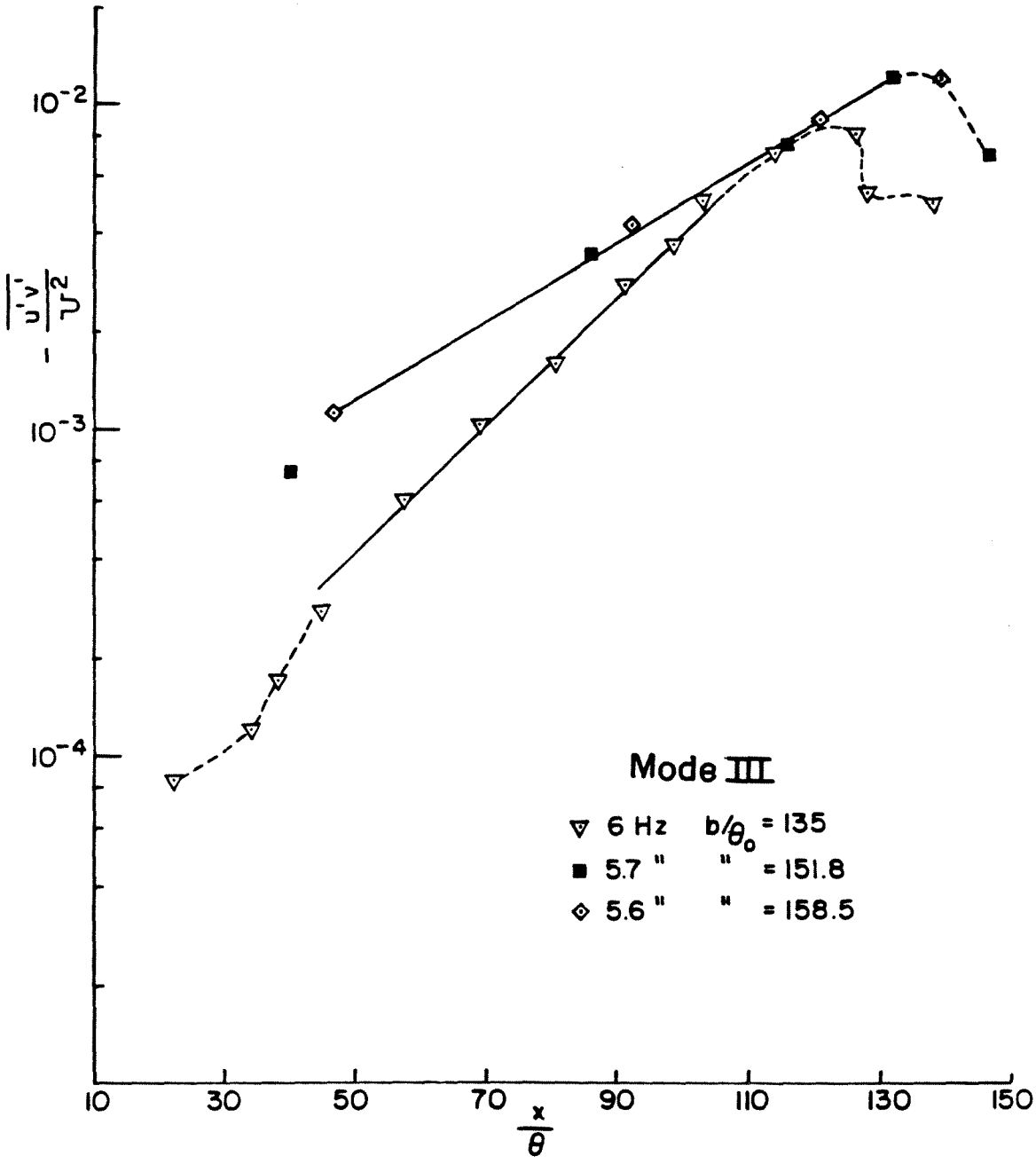

Fig. 30 Growth of the maximum shear stress in the cavity shear layer with downstream distance;
Mode III, $\frac{Fb}{U_c} \simeq 3$.

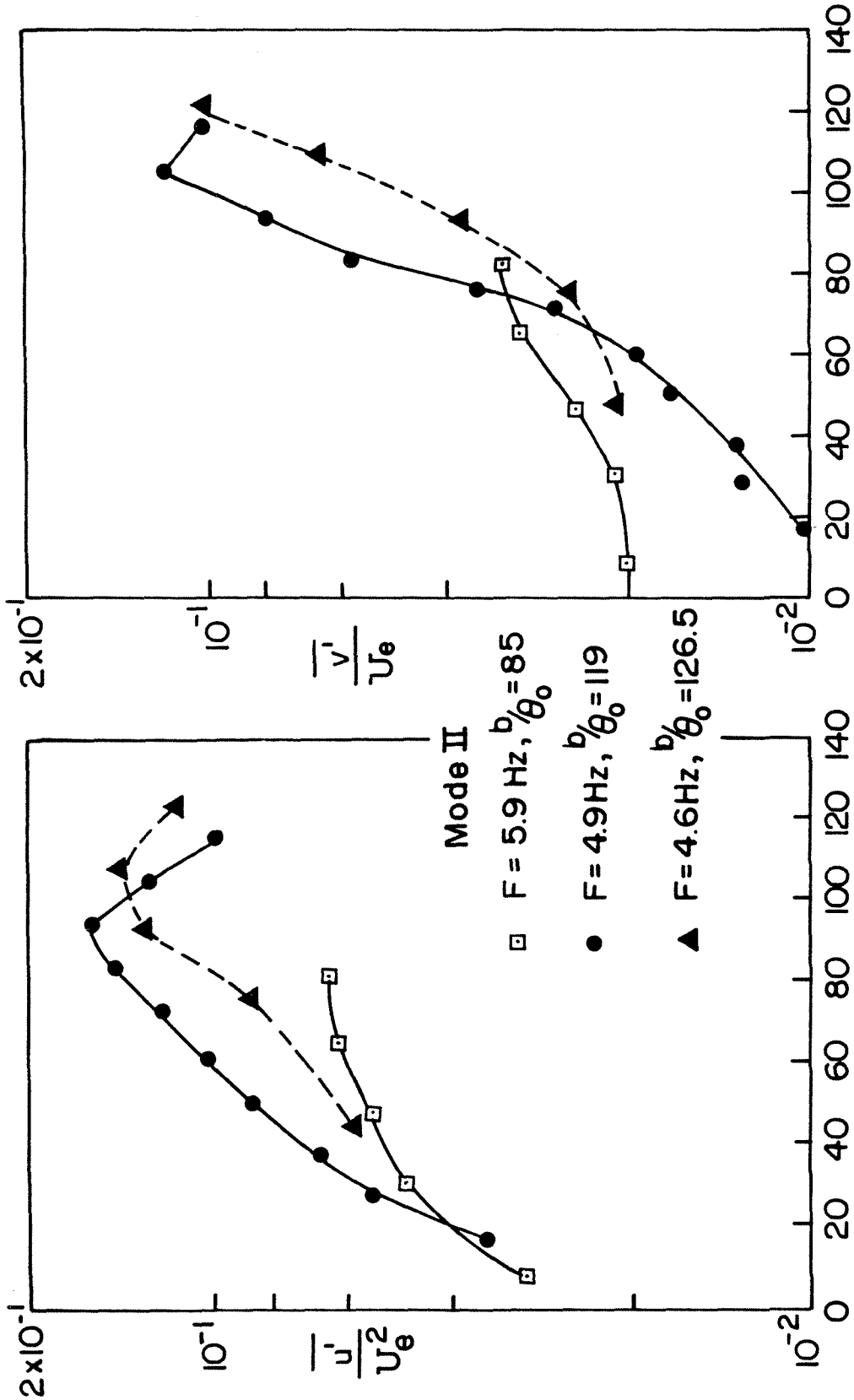

Fig. 31 Growth of the maximum streamwise and transverse rms velocity fluctuations in the cavity shear layer with downstream distance;

Mode II, $\frac{Fb}{U_c} \simeq 2$.

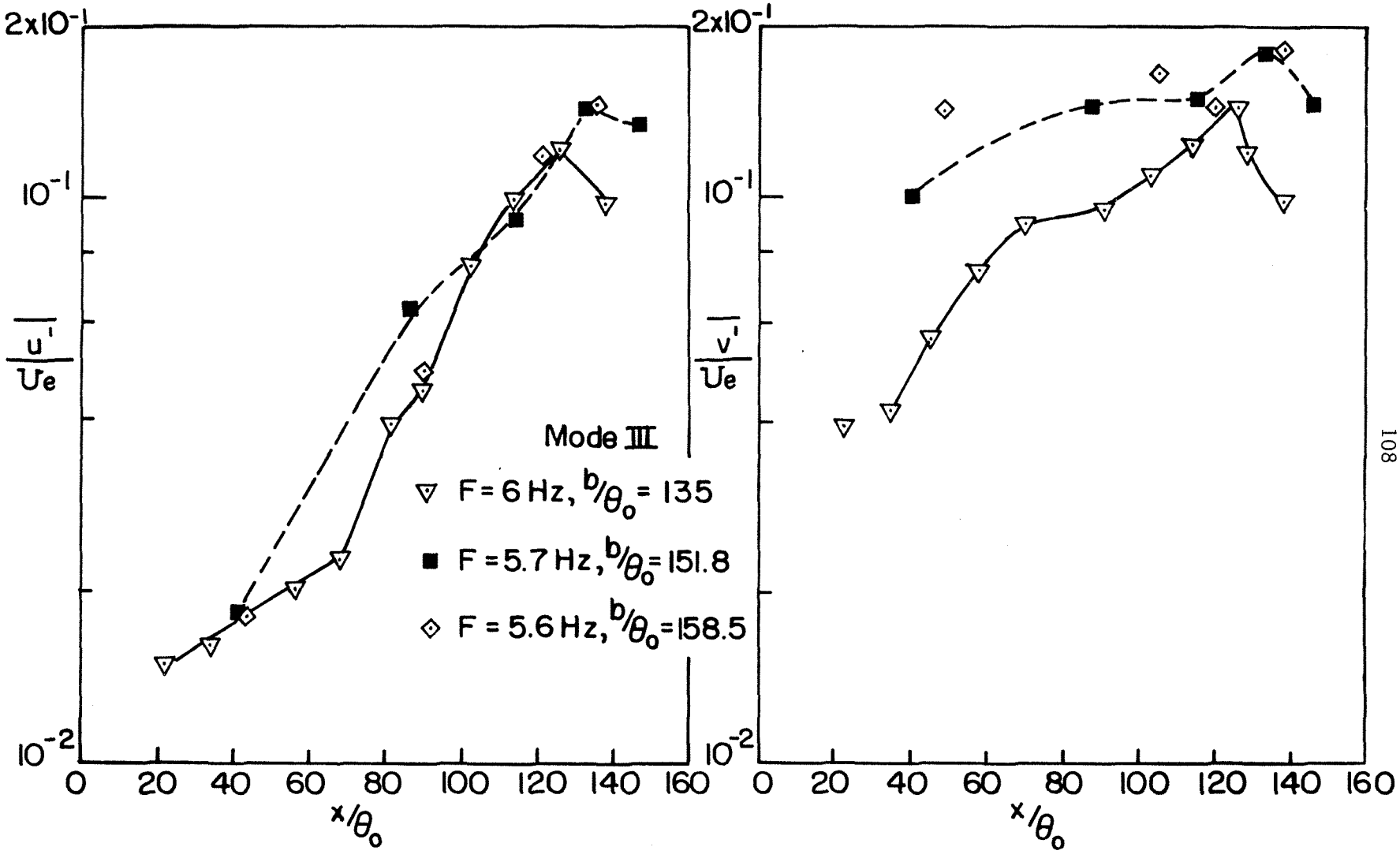

Fig. 32 Growth of the maximum streamwise and transverse rms velocity fluctuations in the cavity shear layer with downstream distance;

Mode III, $\frac{Fb}{U_c} \simeq 3$.

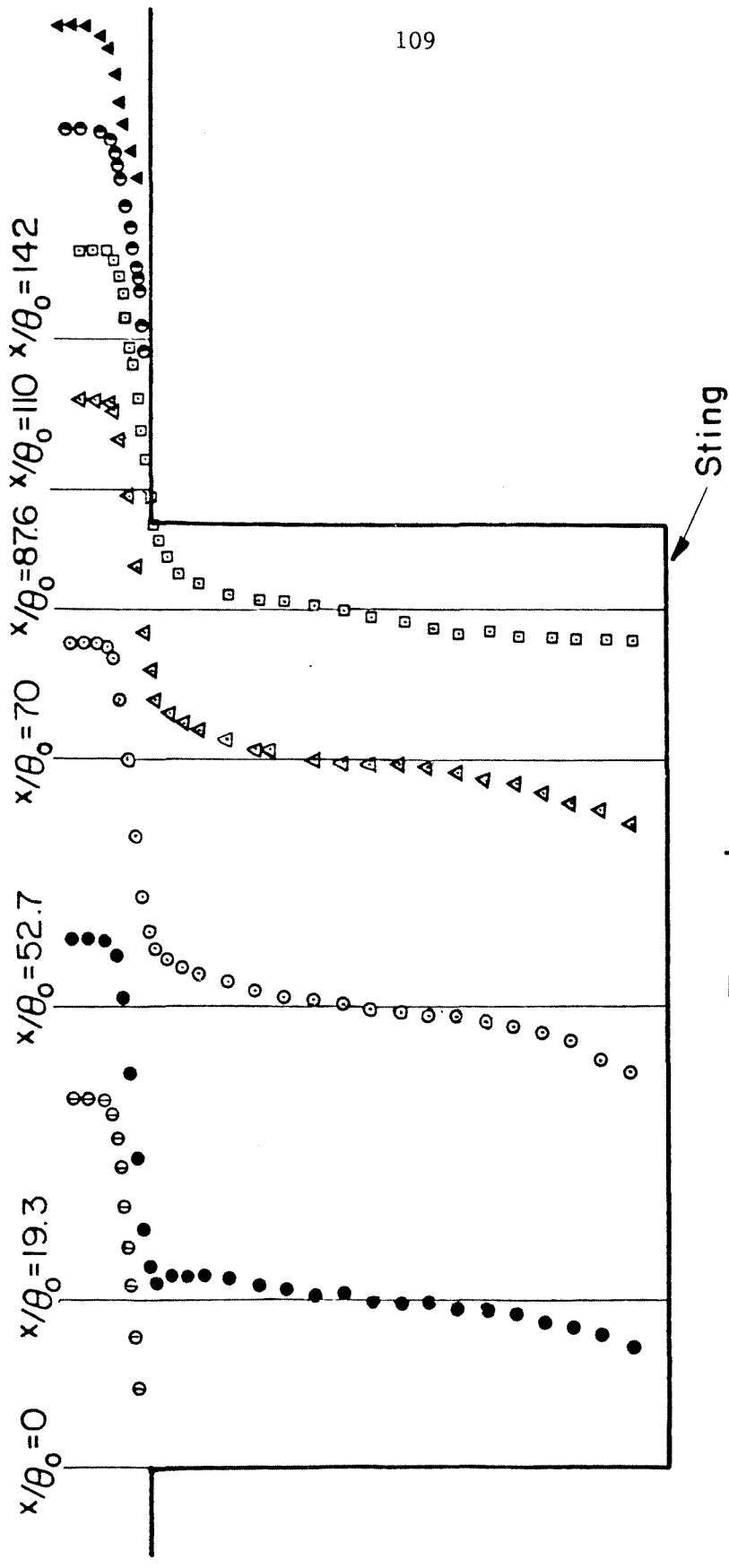

Fig. 33 Non-dimensional streamwise velocity profiles of the cavity flow; $b/\theta_0 = 103$, $F = 5.1$ Hz, Mode II $\frac{Fb}{U_c} \simeq 2$.

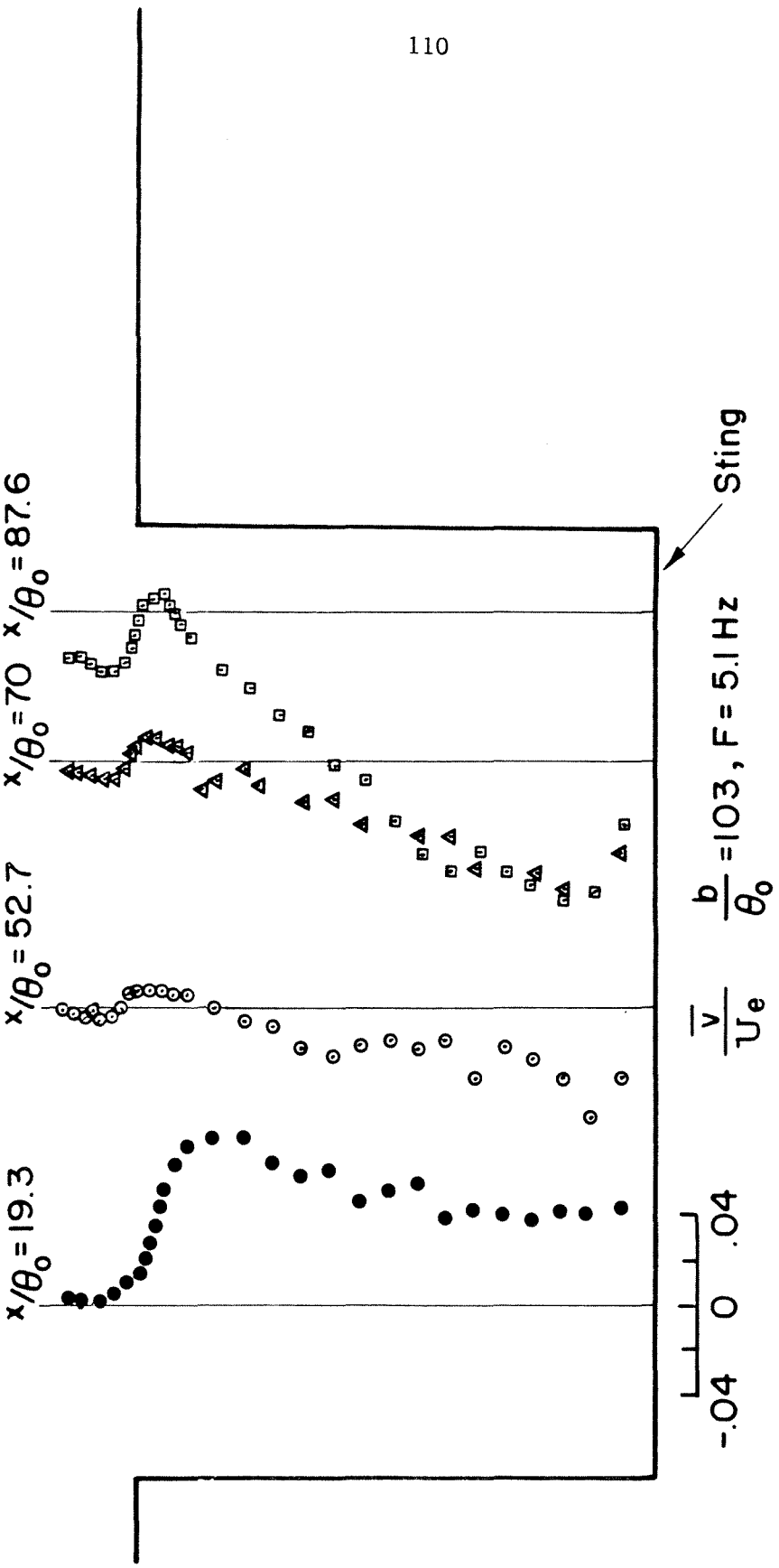

Fig.34 Non-dimensional transverse velocity profiles of the cavity flow; $b/\theta_0 = 103$, $F = 5.1$ Hz, Mode II $\frac{Fb}{U_c} \simeq 2$.

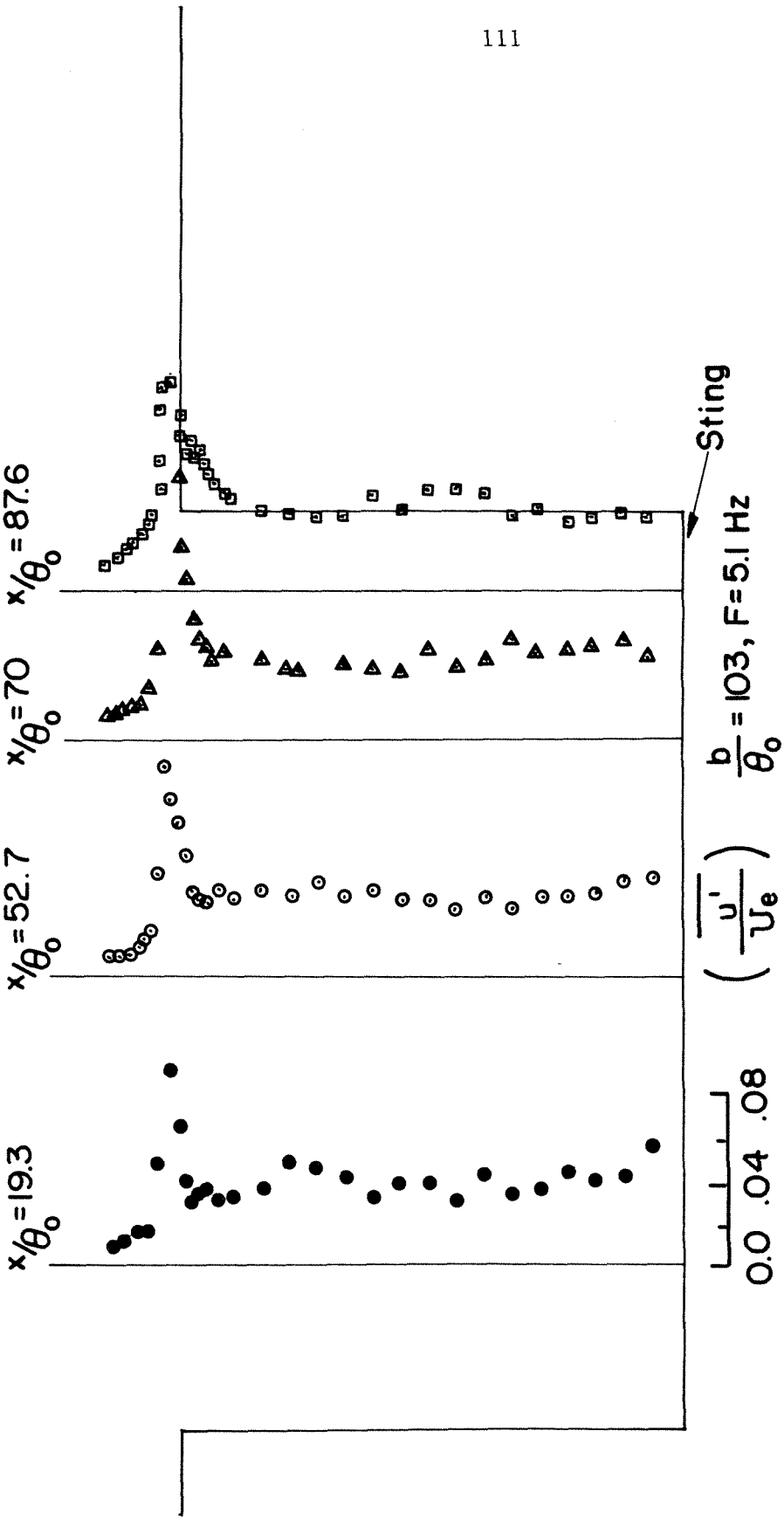

Fig. 35 Streamwise velocity fluctuation profiles of the cavity flow; $b/\theta_0 = 103$, F = 5.1 Hz, Mode III $\frac{Fb}{U_c} \simeq 2$.

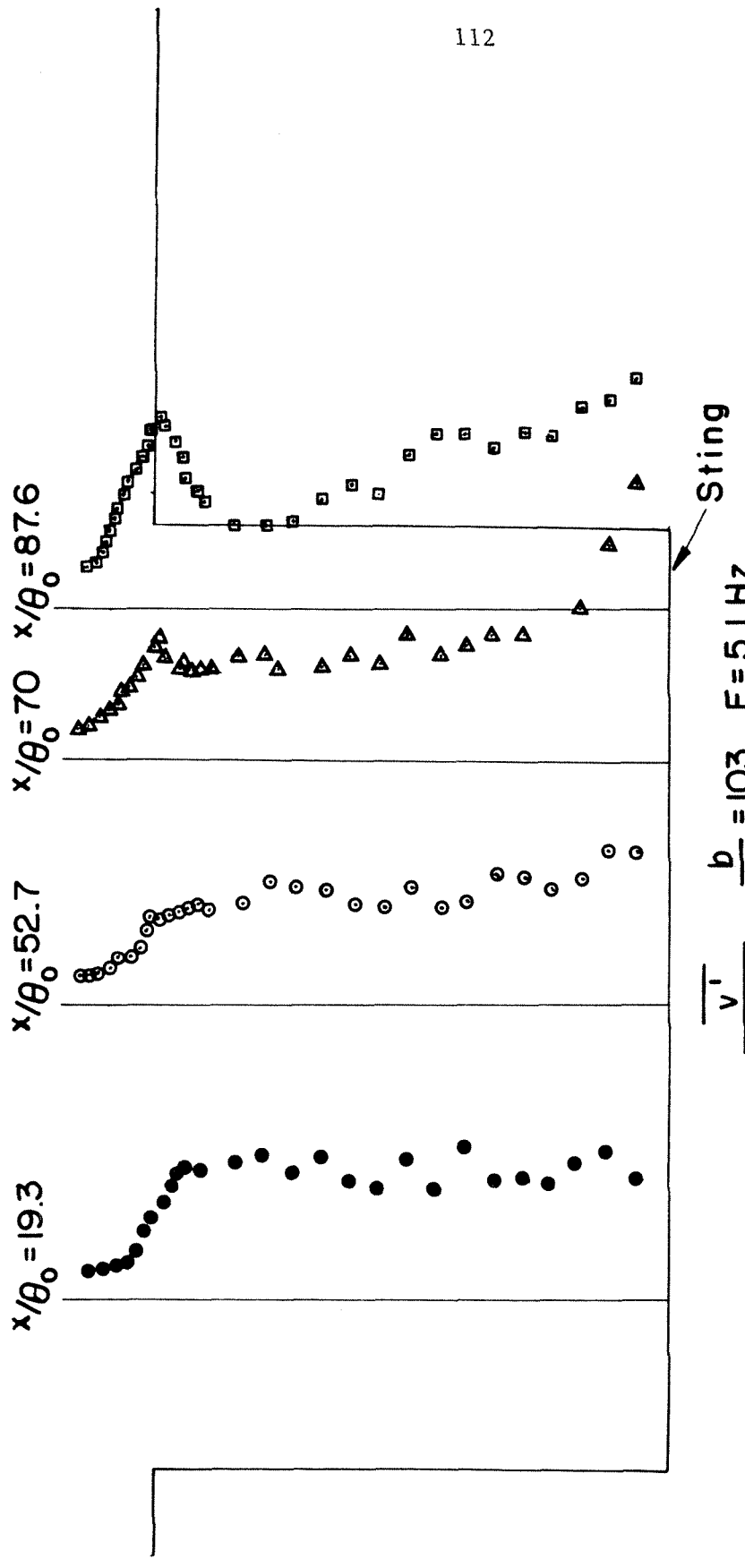

Fig. 36 Non-dimensional transverse velocity fluctuation profiles of the cavity flow; $b/\theta_0 = 103$, F = 5.1 Hz, Mode II $\frac{Fb}{U_c} \simeq 2$.

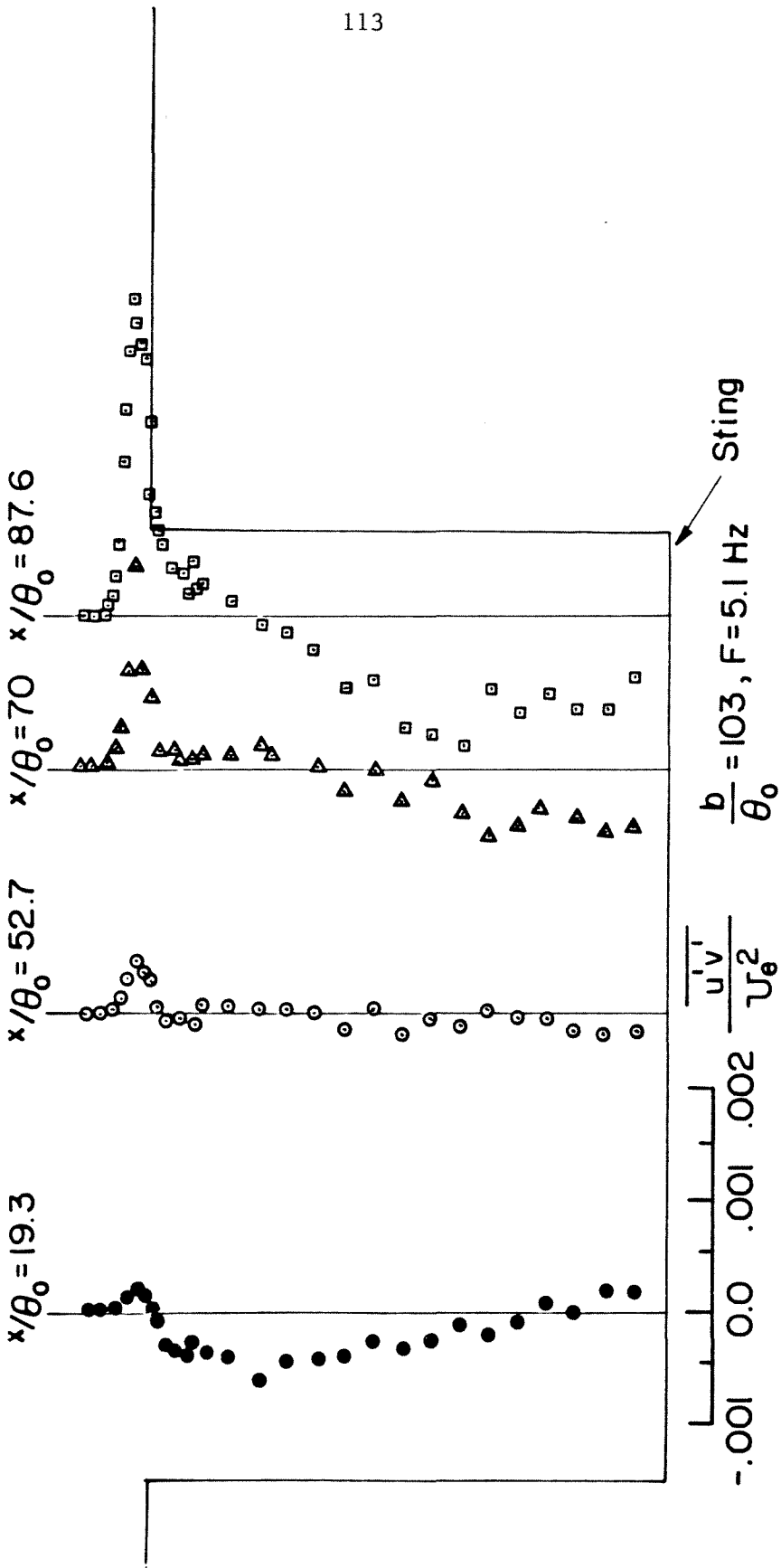

Fig. 37 Shear stress profiles of the cavity flow; $b/\theta_0 = 103$, F = 5.a Hz, Mode II, $\frac{Fb}{U_c} \approx 2.$

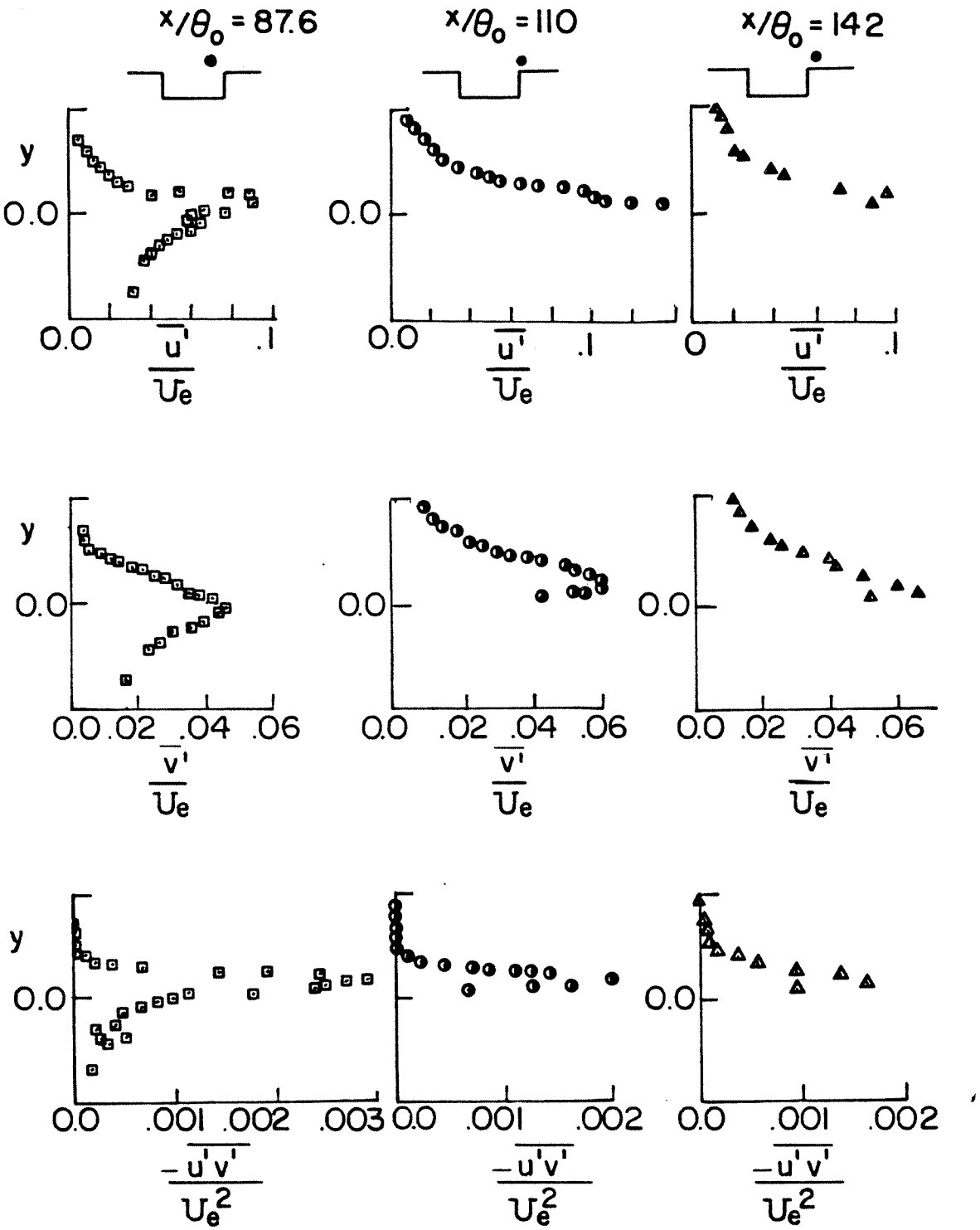

Fig. 38 Effect of the downstream corner on the velocity fluctuations and shear stress profiles of impinging cavity shear layer; $b/\theta_0 = 103$, F = 5.1 Hz, Mode II $\frac{Fb}{U_c} \simeq 2$.

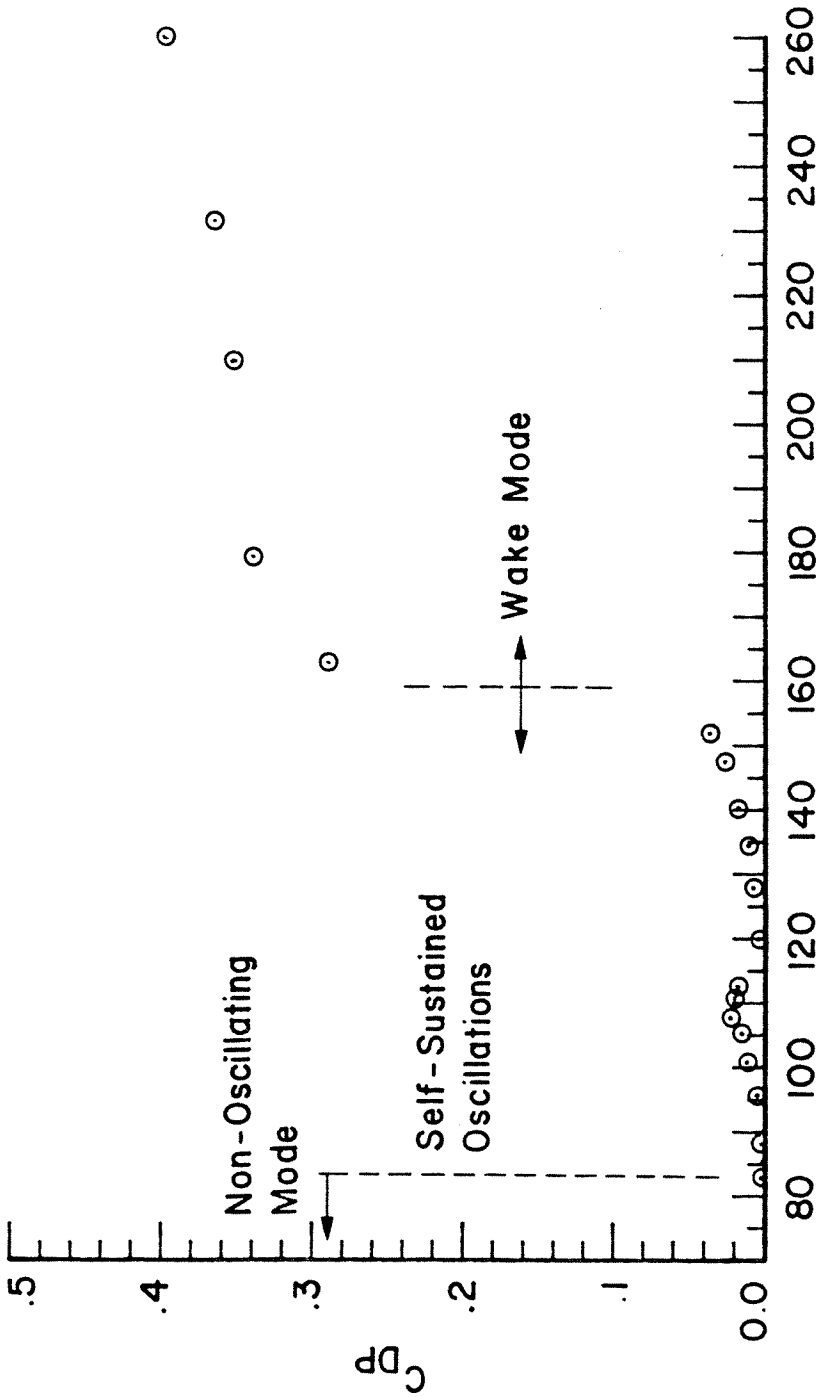

Fig. 39 Variation of the axisymmetric cavity drag coefficient with non-dimensional cavity width, b/θ_0 .

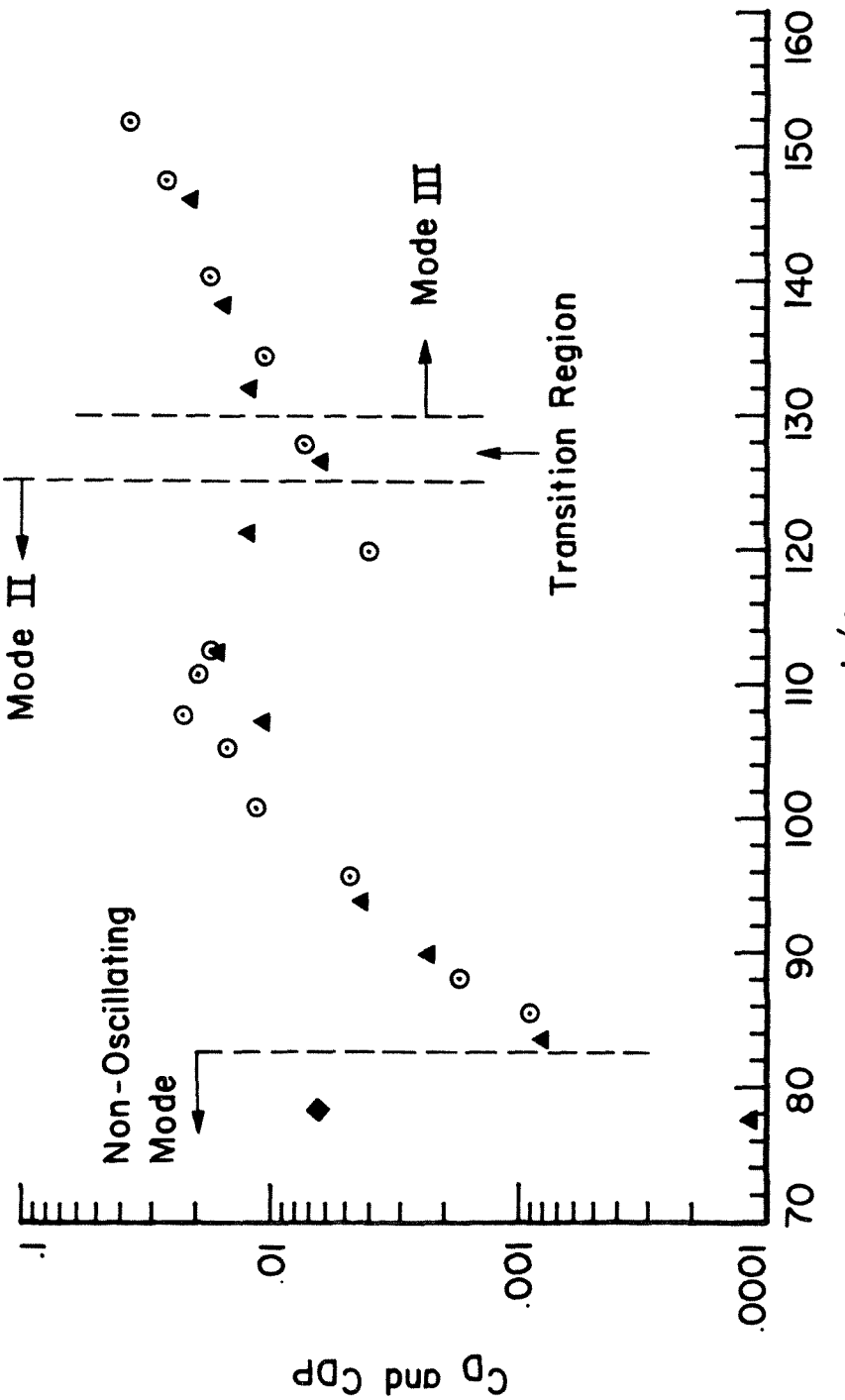

Fig. 40 Exponential dependence of the cavity drag coefficient on b/θ_0 . ⊙ C_{DP} ; ▲ C_D . ◆ - estimated C_D based on boundary layer friction in the absence of the cavity.

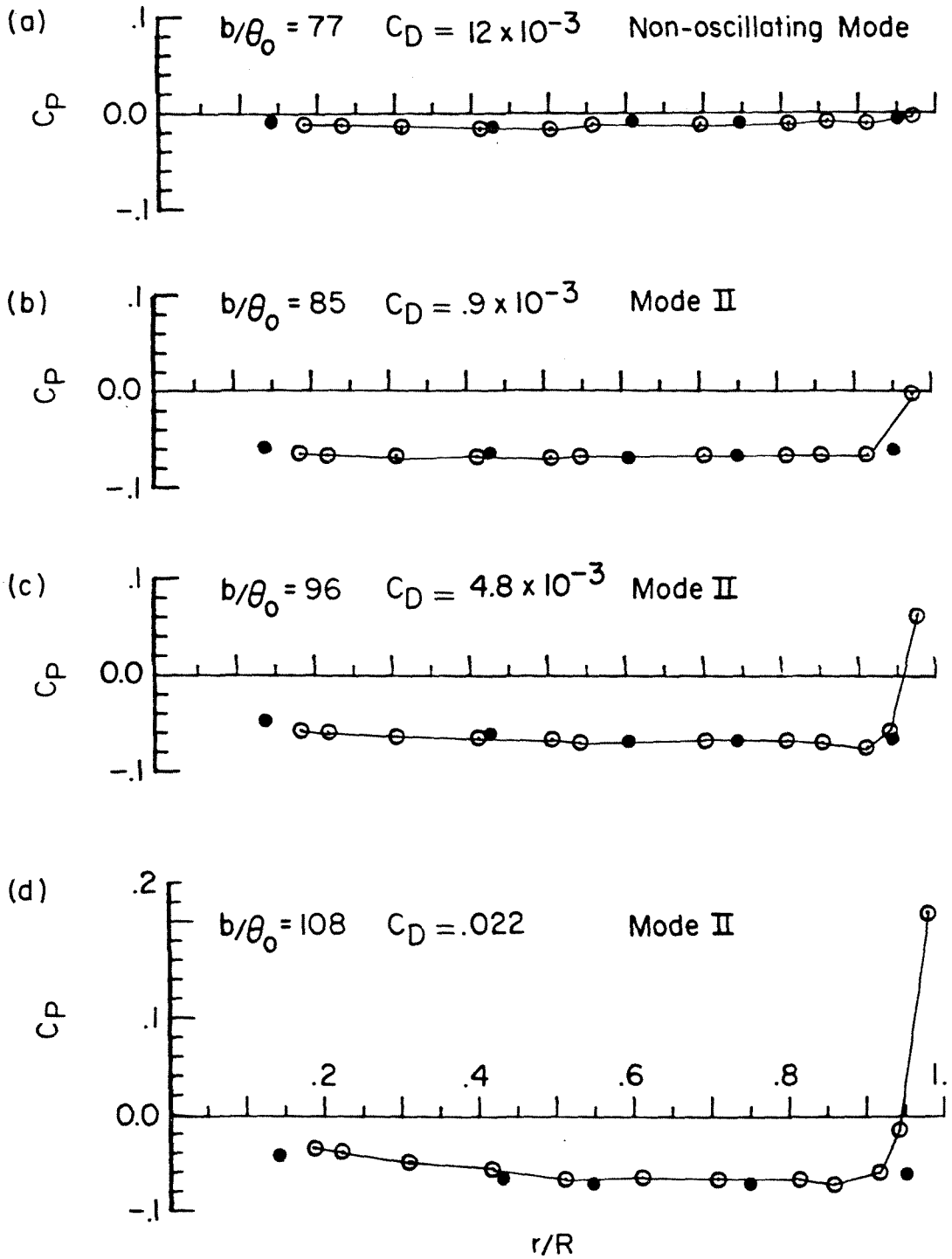

Fig. 41 Pressure coefficient distribution in Mode II of the oscillations.

● Upstream face pressure coefficient distribution.

⊙ Downstream face pressure coefficient distribution.

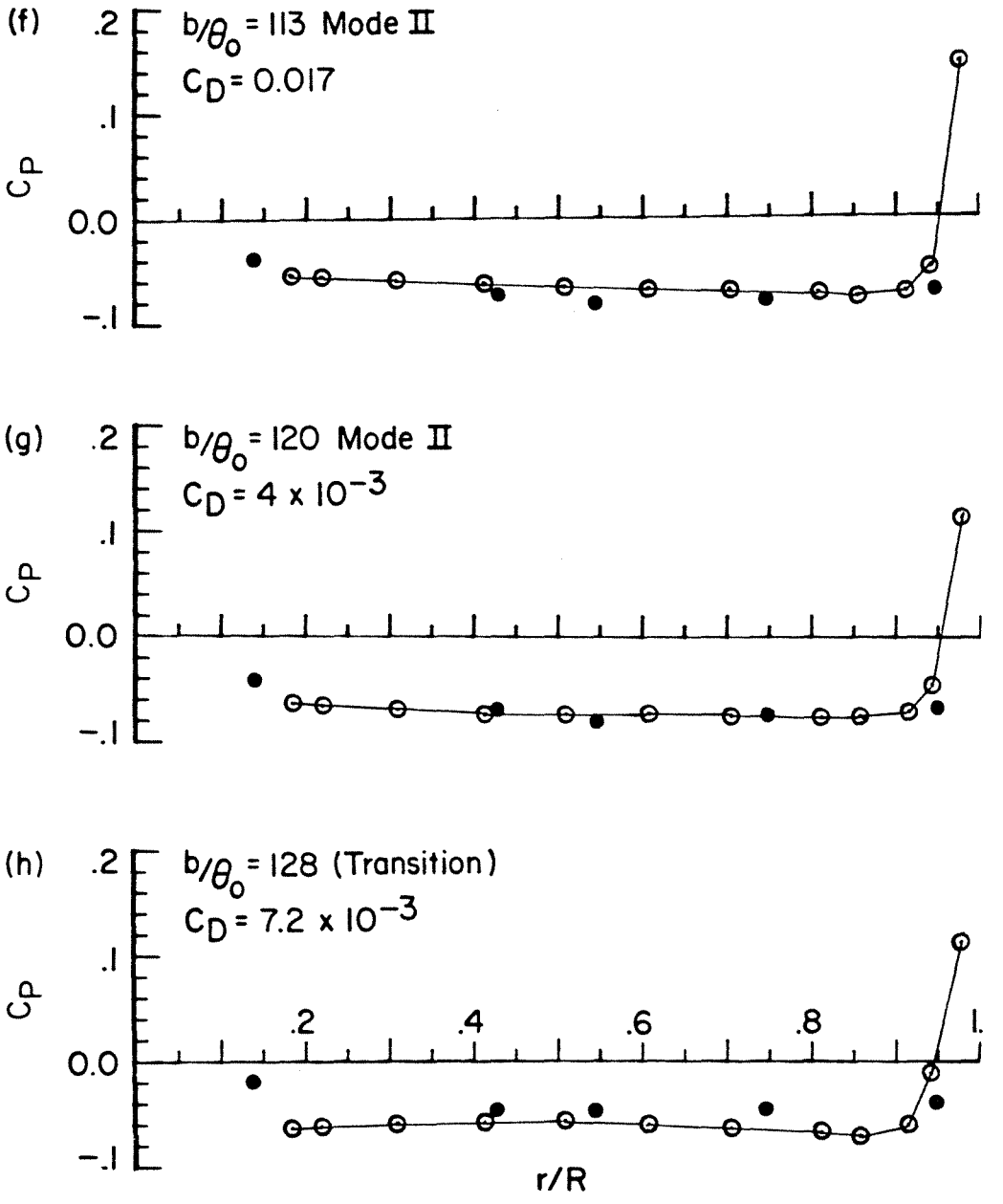

Fig. 41 Continued.

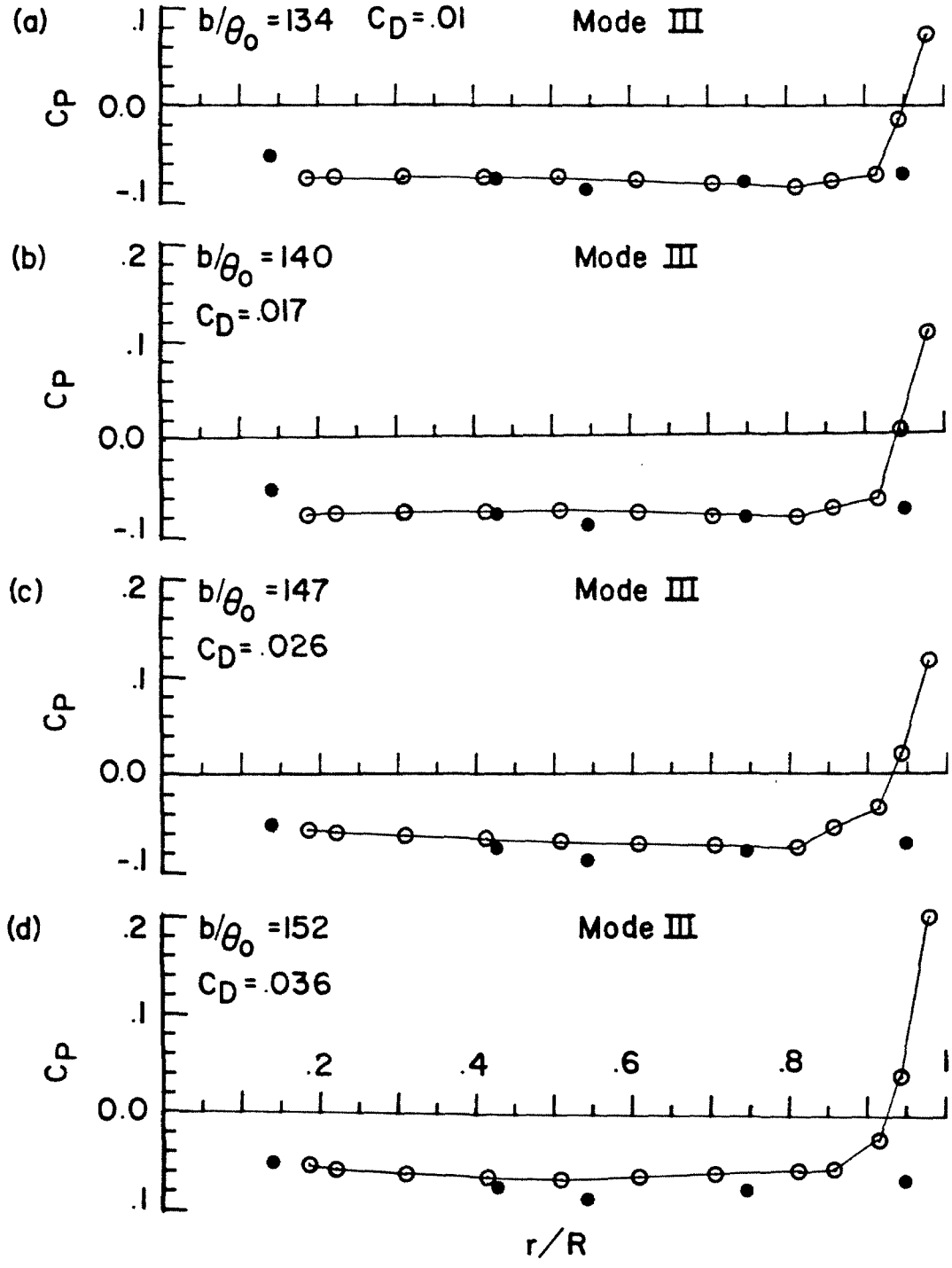

Fig. 42 Pressure coefficient distribution in Mode III of the oscillations.

● Upstream face pressure coefficient distribution.

○ Downstream face pressure coefficient distribution.

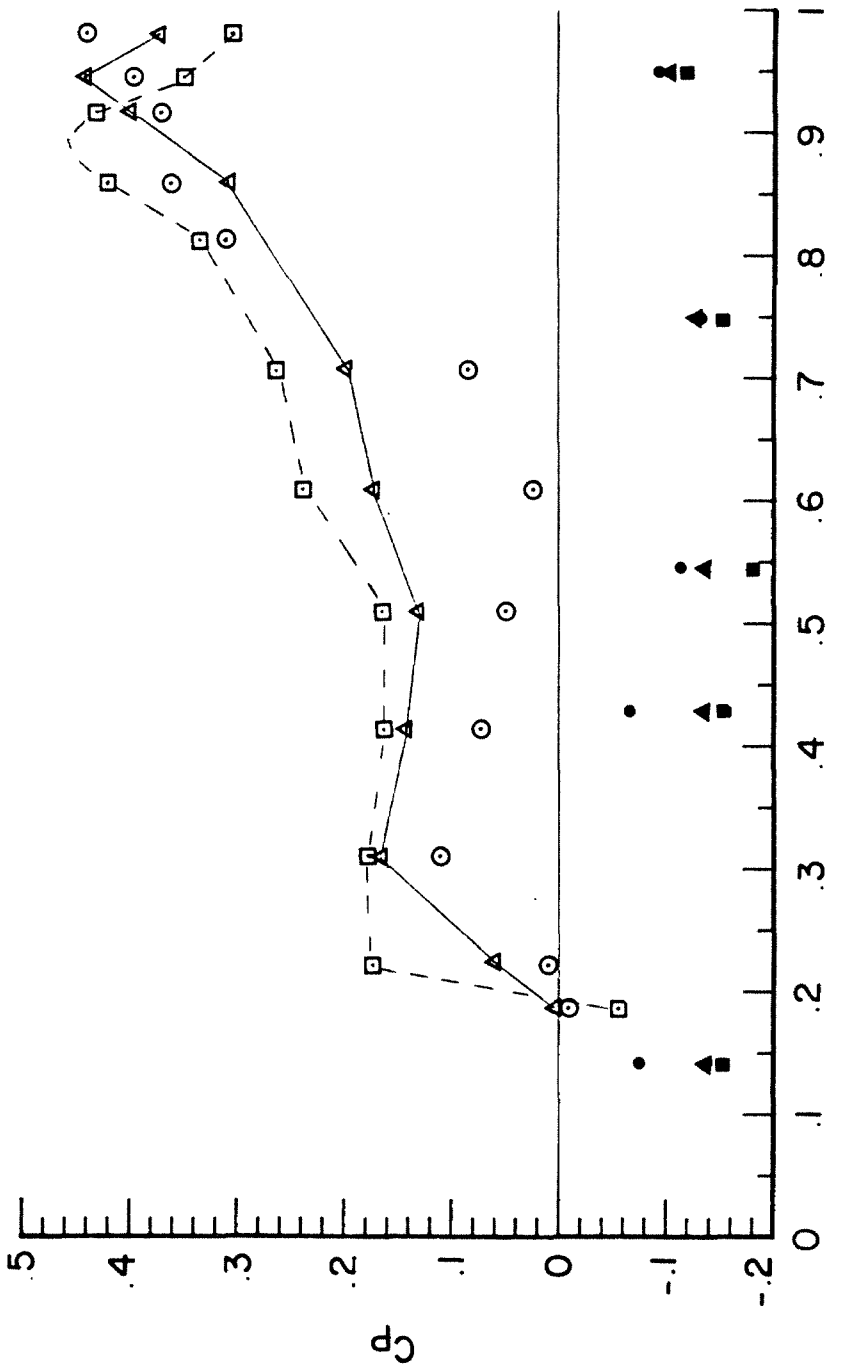

Fig.43 Cavity pressure coefficient distribution in the wake mode. ● ⊙ , b/θ_0 = 123; ▲ Δ , b/θ_0 = 165; ■ ⊡ , b/θ_0 = 203; solid and open symbols represent upstream and downstream face respectively.

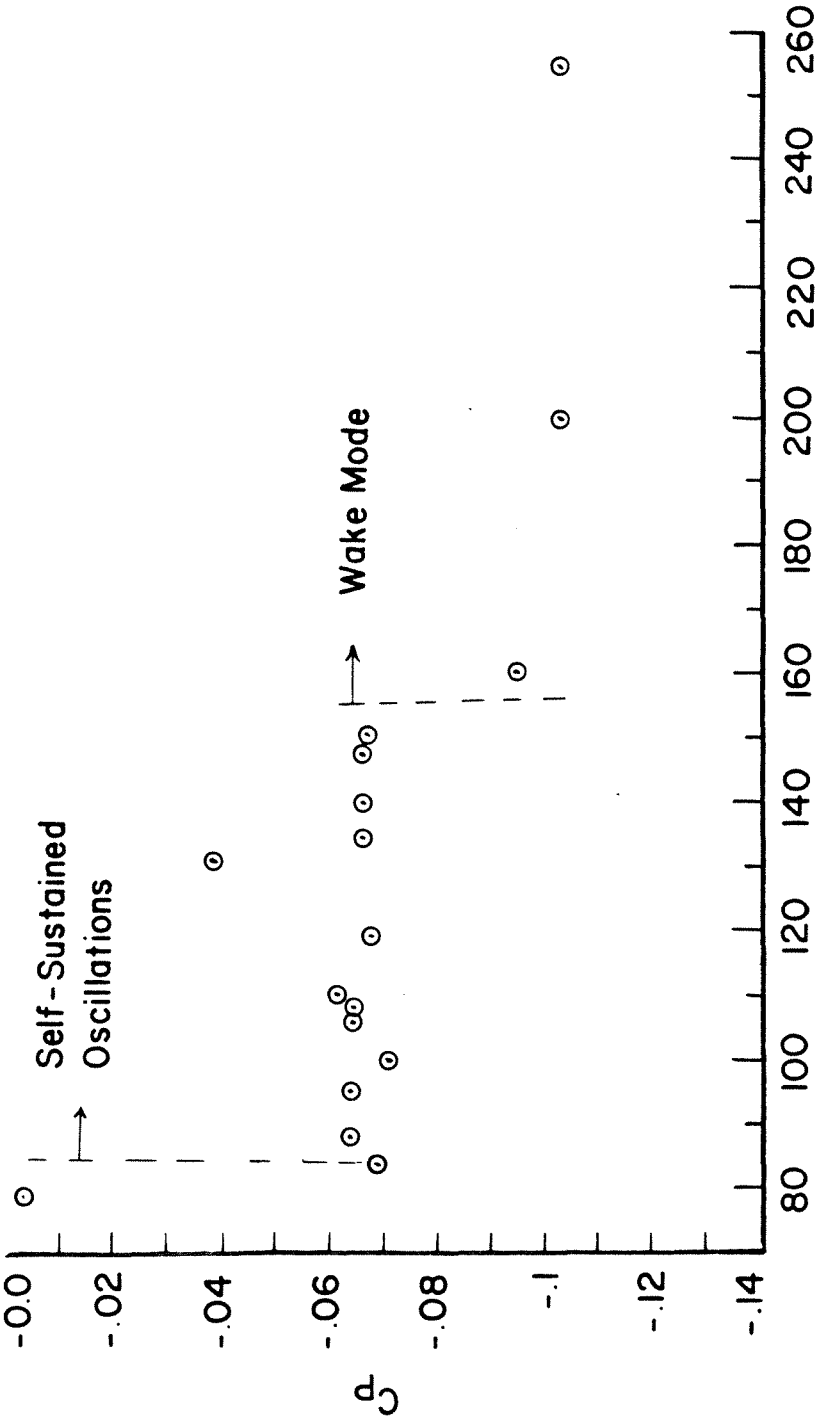

Fig. 44 Variation of the upstream corner pressure coefficient with b/θ_0.

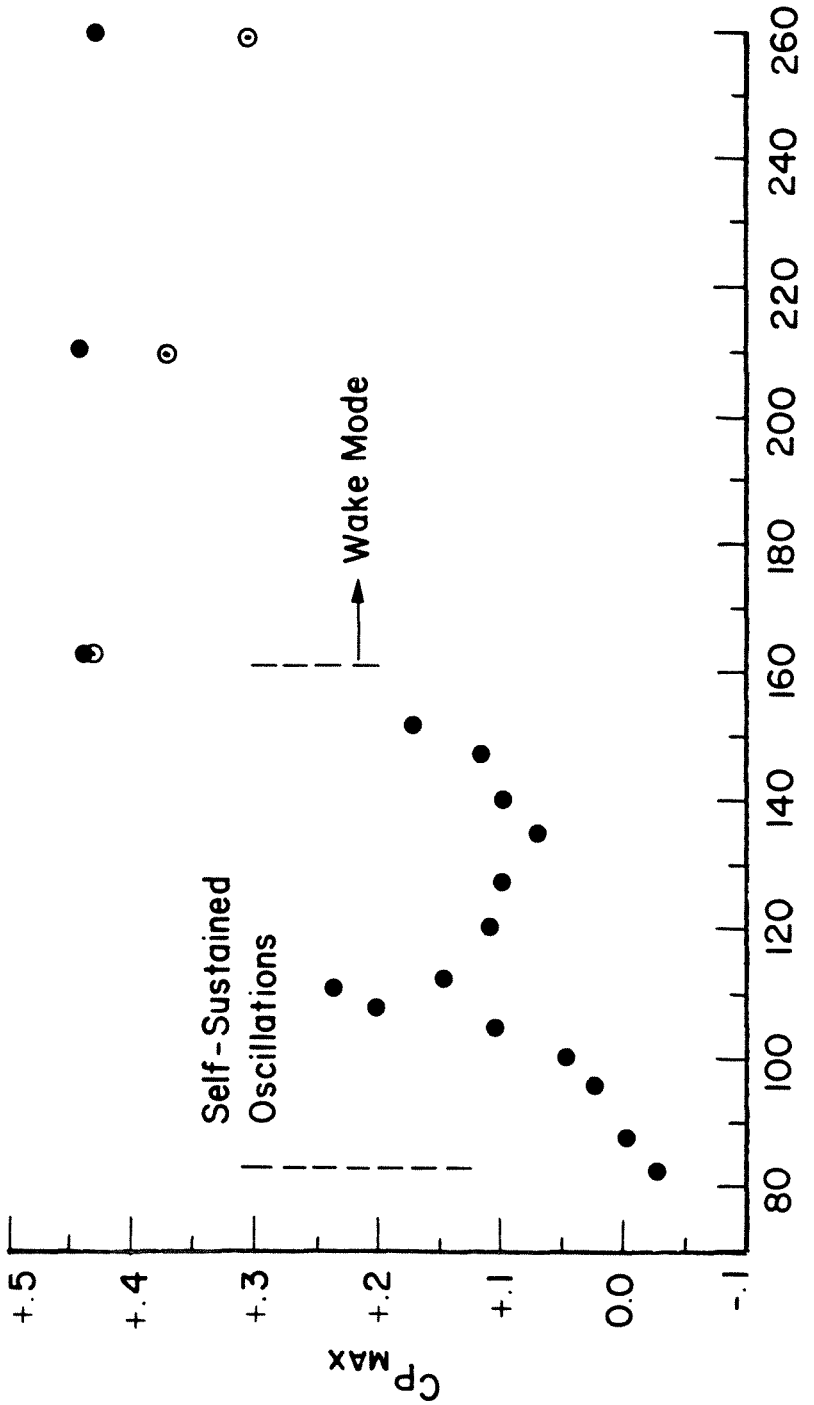

Fig. 45 Variation of maximum pressure coefficient with b/θ_0; ● maximum pressure coefficient; ⊙ pressure coefficient at the downstream corner.

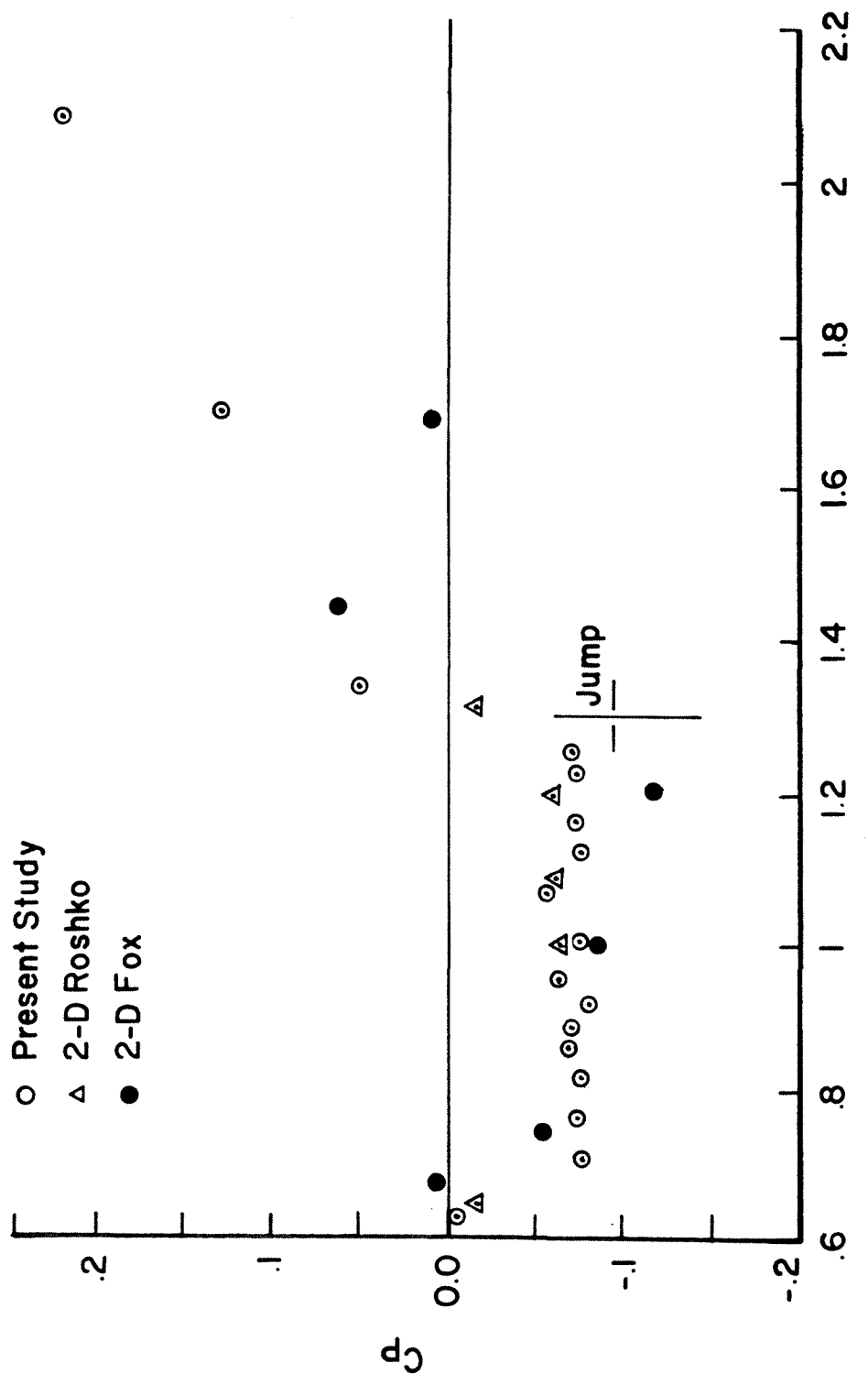

Fig. 46 Variation of pressure coefficient at the middle of the downstream face with b/θ_0 .

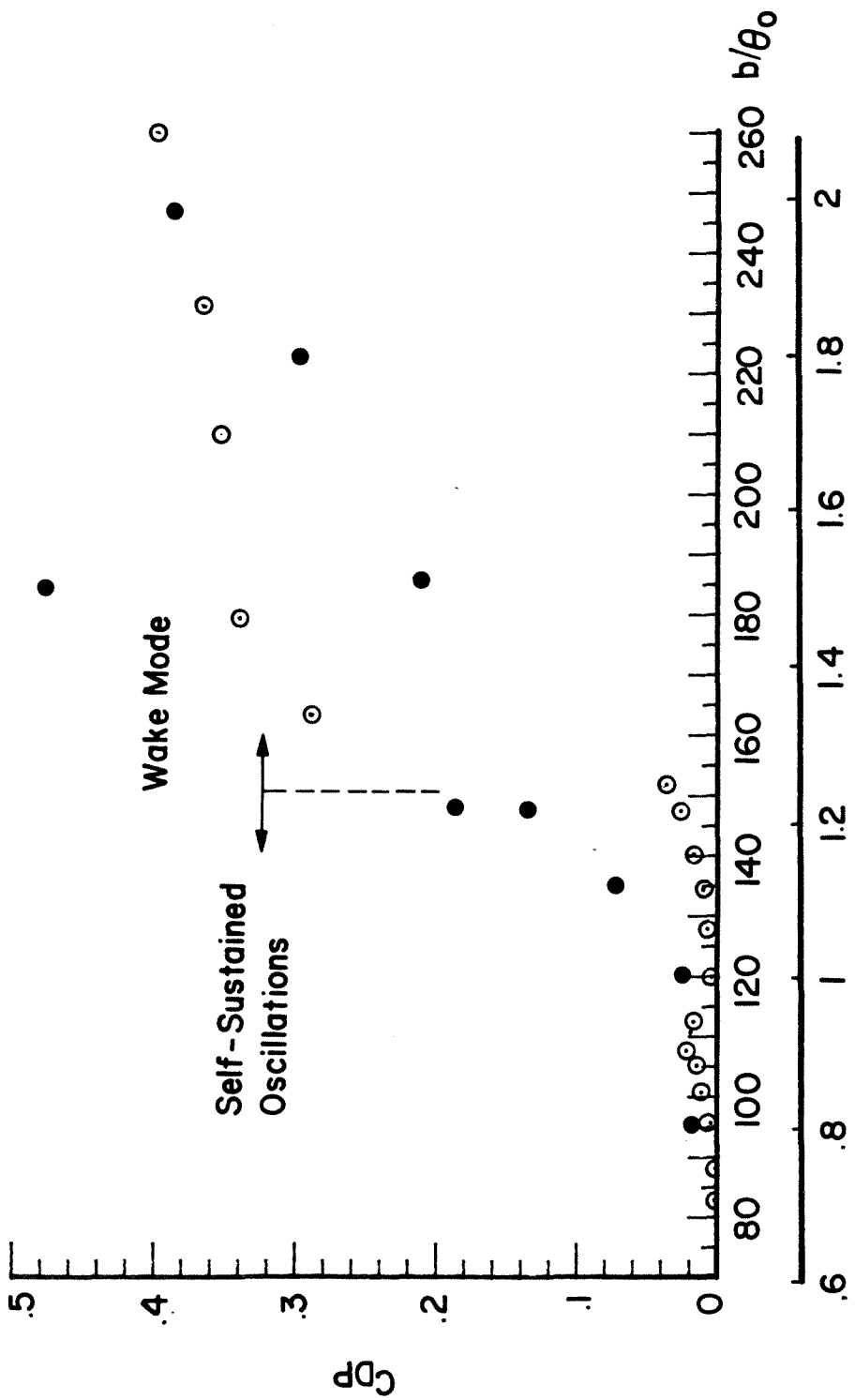

Fig. 47 Variation of the cavity drag coefficient with b/R; ⊙ present study; ● Koenig (1978) optimum drag coefficient of disk-cylinder combination.

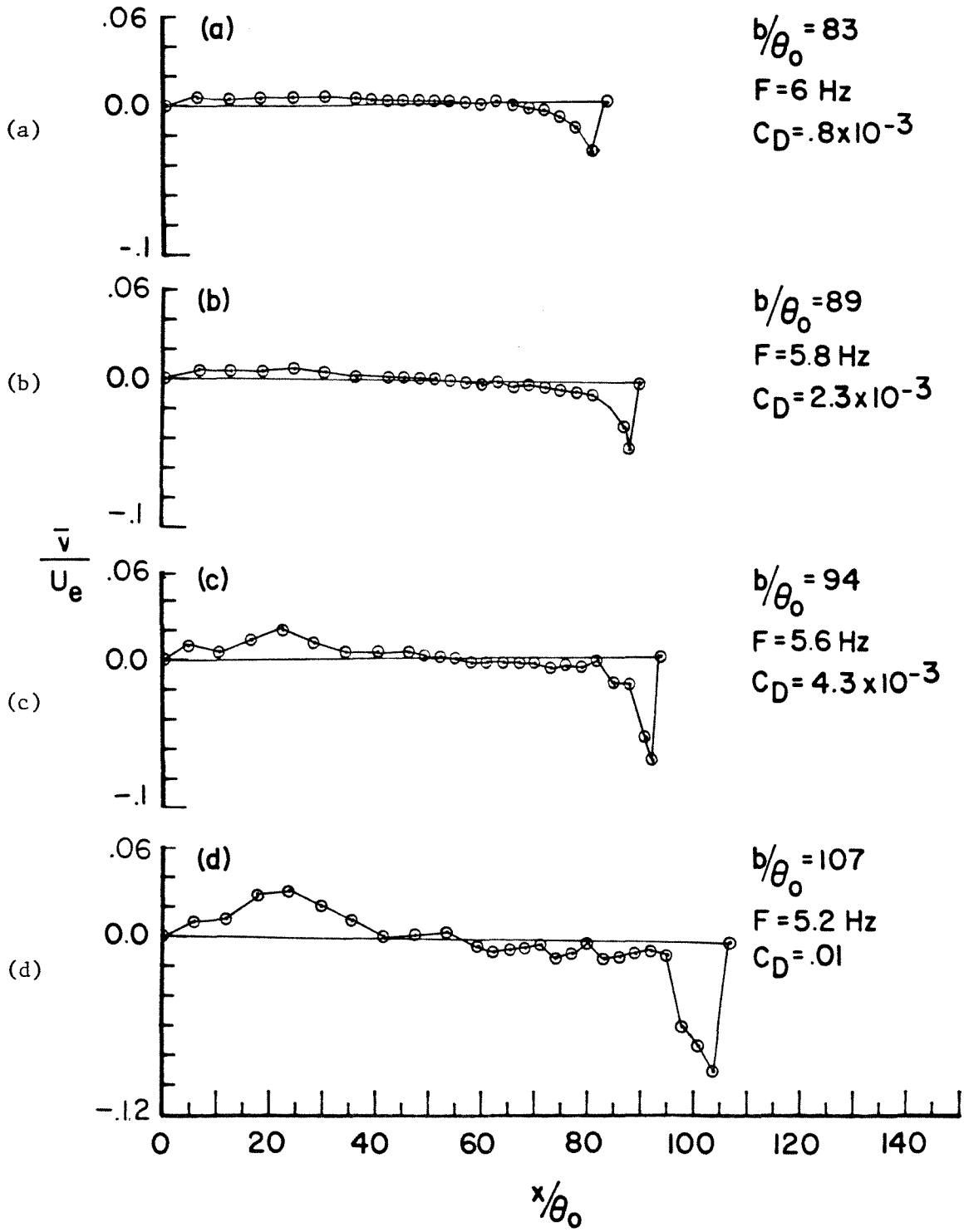

Fig. 48 Distribution of the mean transverse velocity $\frac{\bar{v}}{U_e}$ along y = 0 line in Mode II.

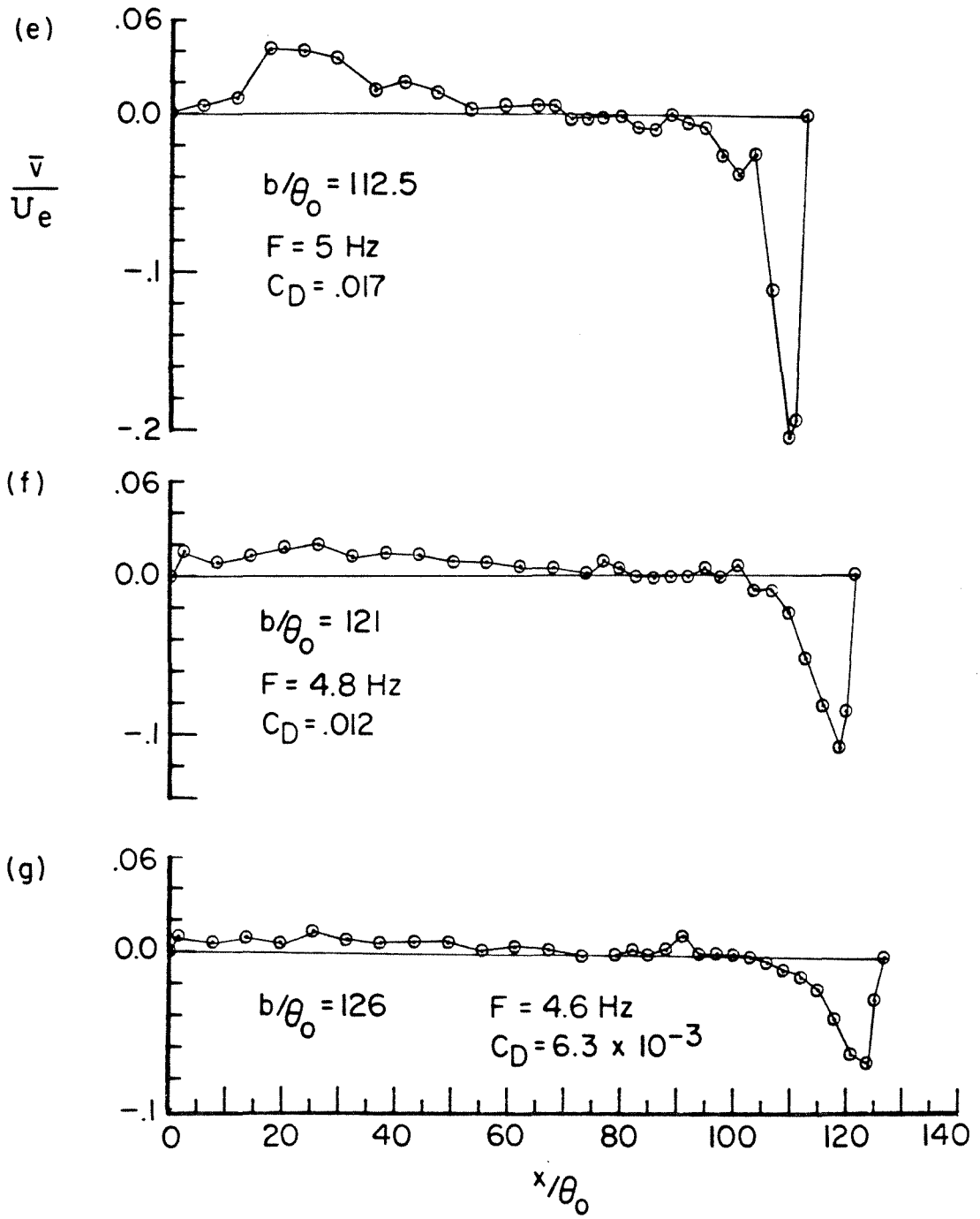

Fig. 48 Continued.

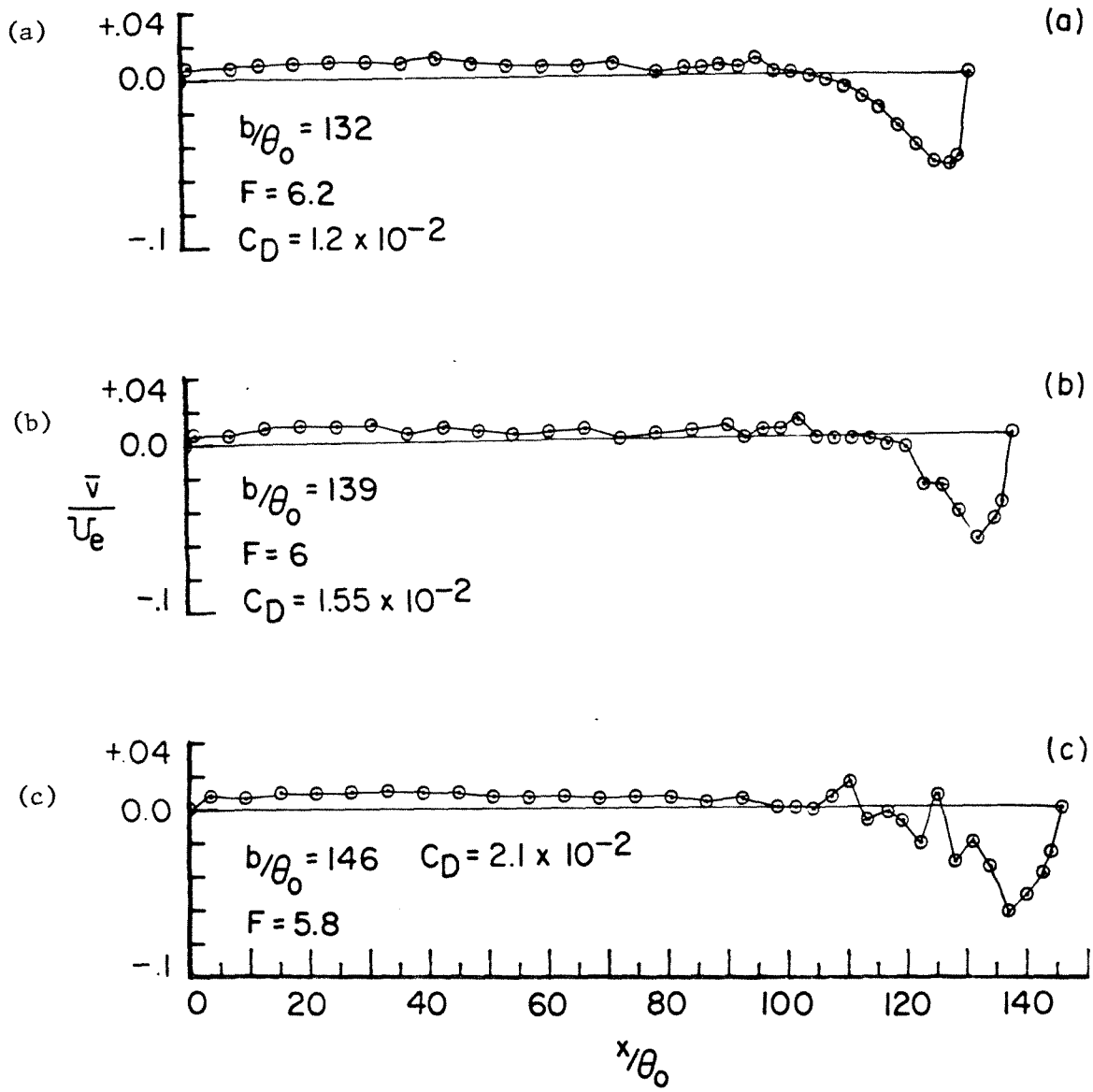

Fig. 49 Distribution of the mean transverse velocity $\frac{\bar{v}}{U_e}$, along y = 0 line in Mode III.

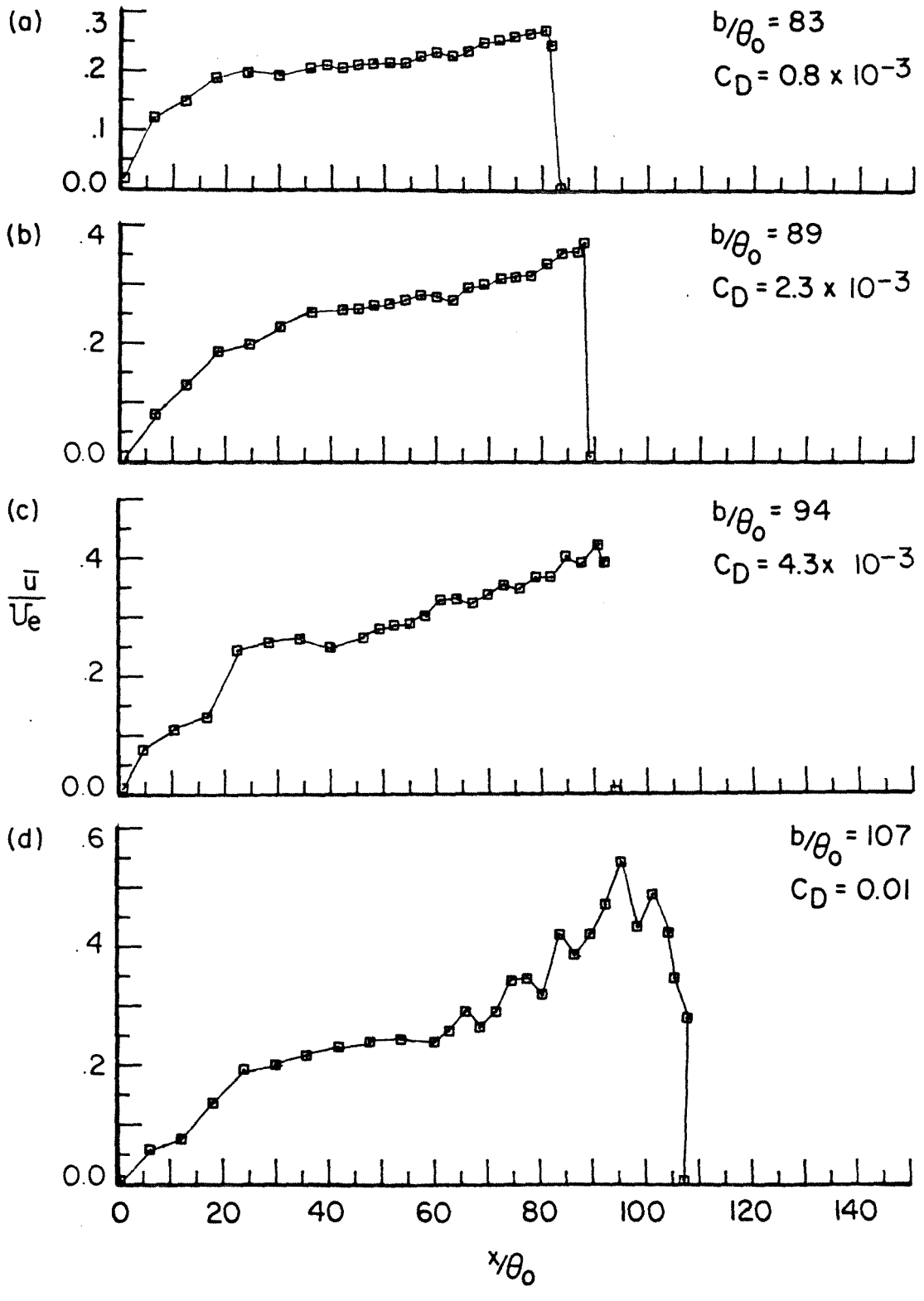

Fig. 50 Distribution of the mean streamwise velocity $\frac{\bar{u}}{U_e}$, along y = 0 line in Mode II.

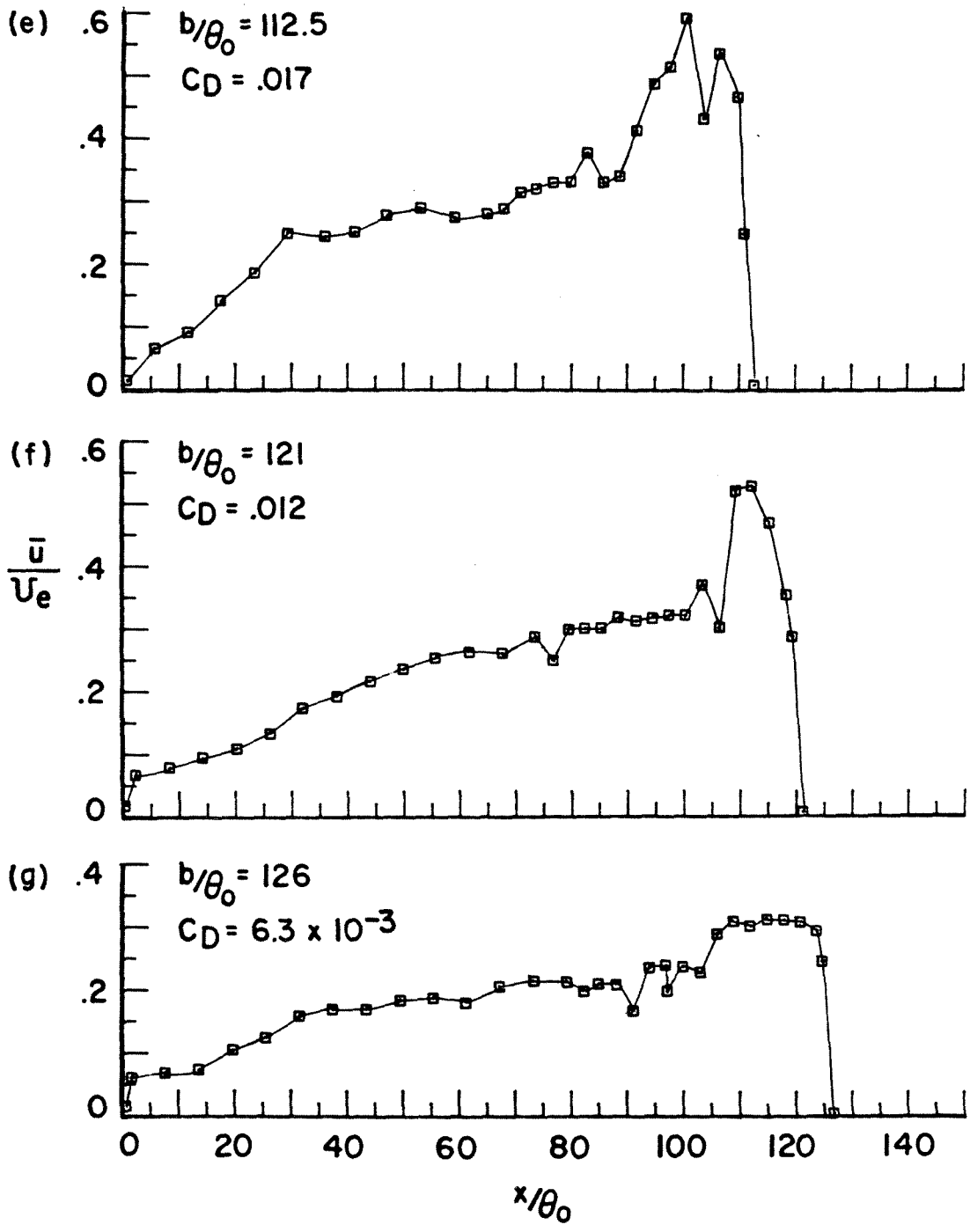

Fig. 50 Continued.

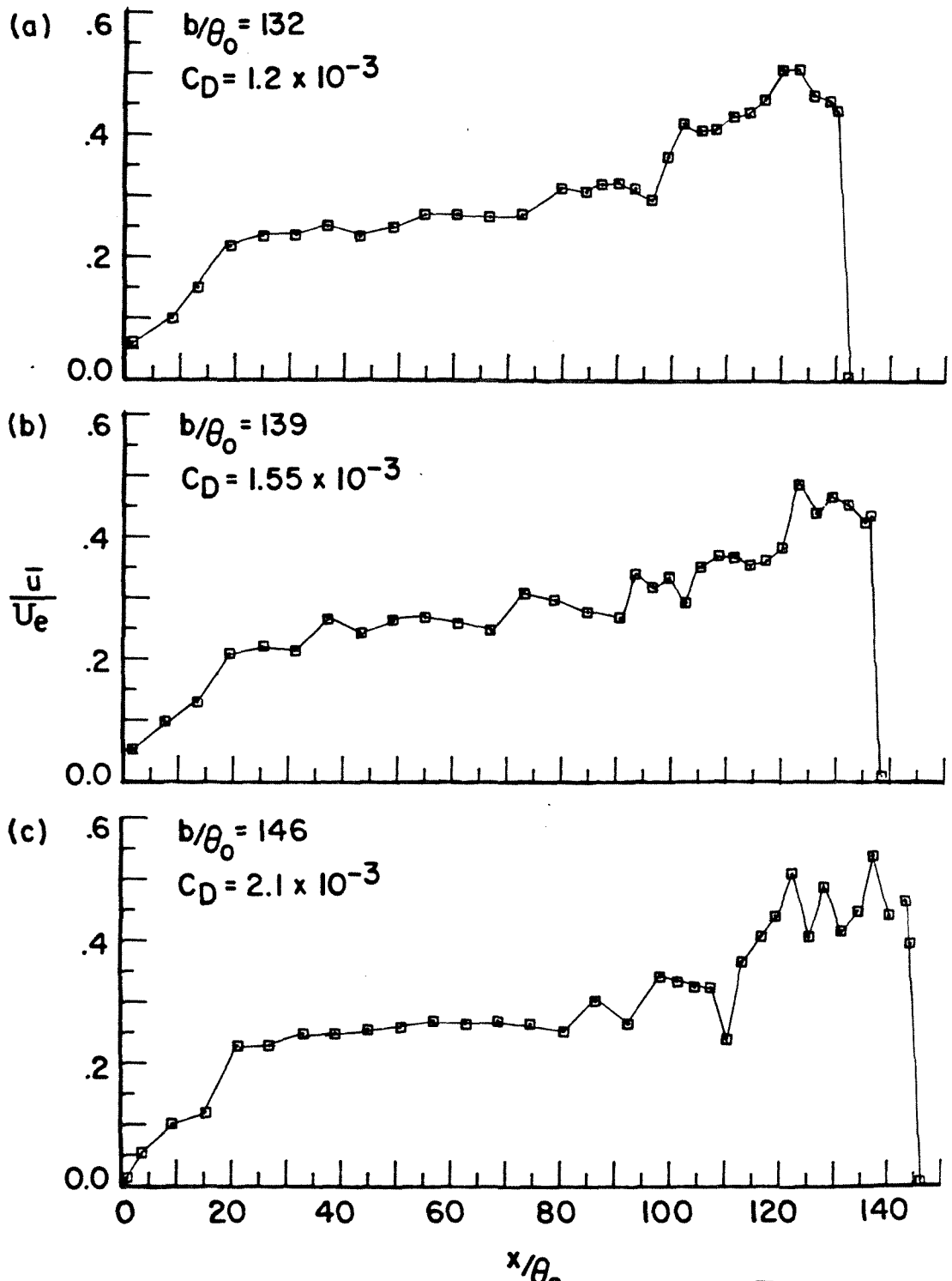

Fig. 51 Distribution of the mean streamwise velocity $\frac{\bar{u}}{U_e}$, along y = 0 line in Mode III.

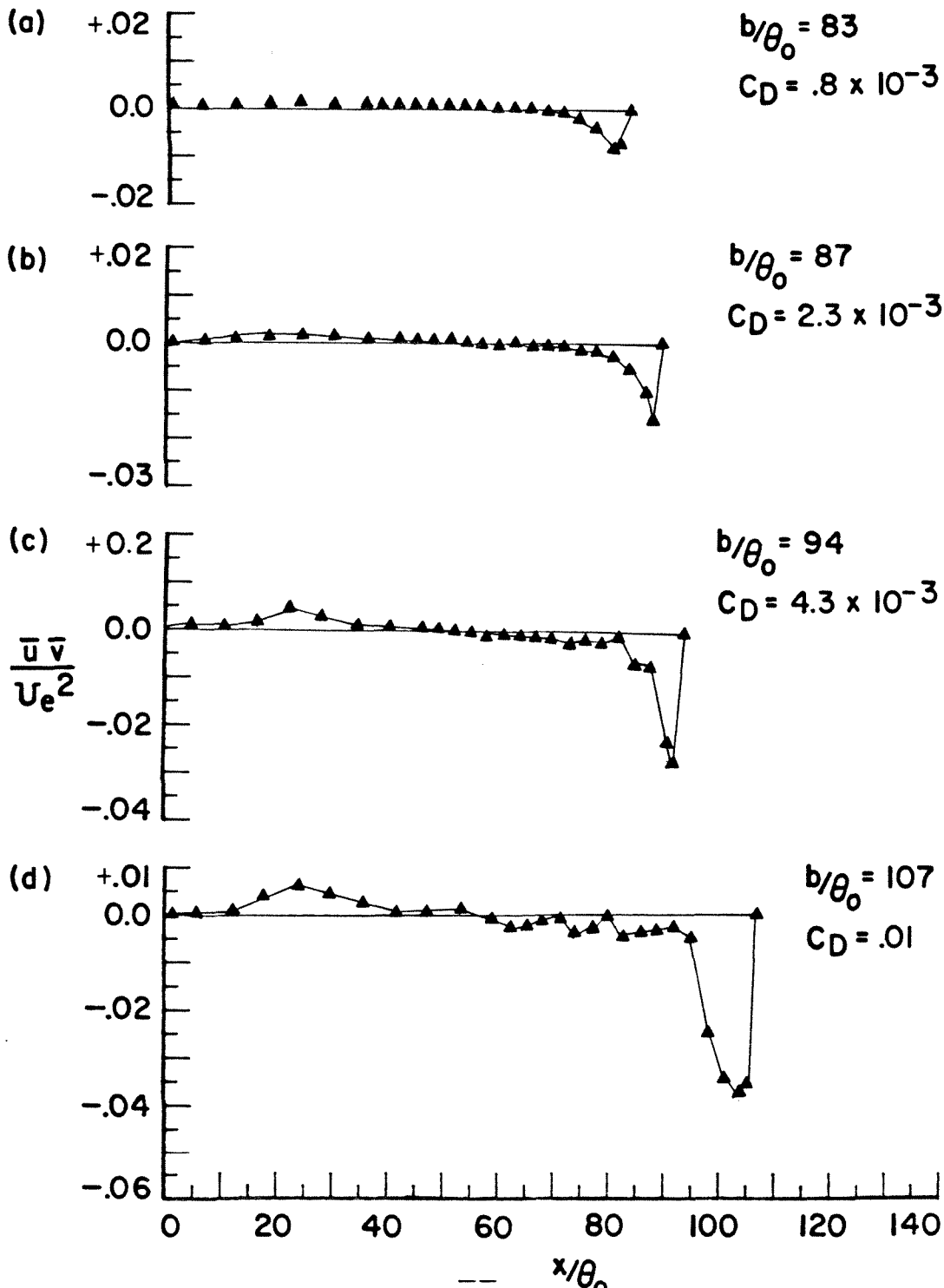

Fig. 52 Distribution of the $\frac{\overline{u}\,\overline{v}}{U_e^2}$ term along y = 0 line in Mode II.

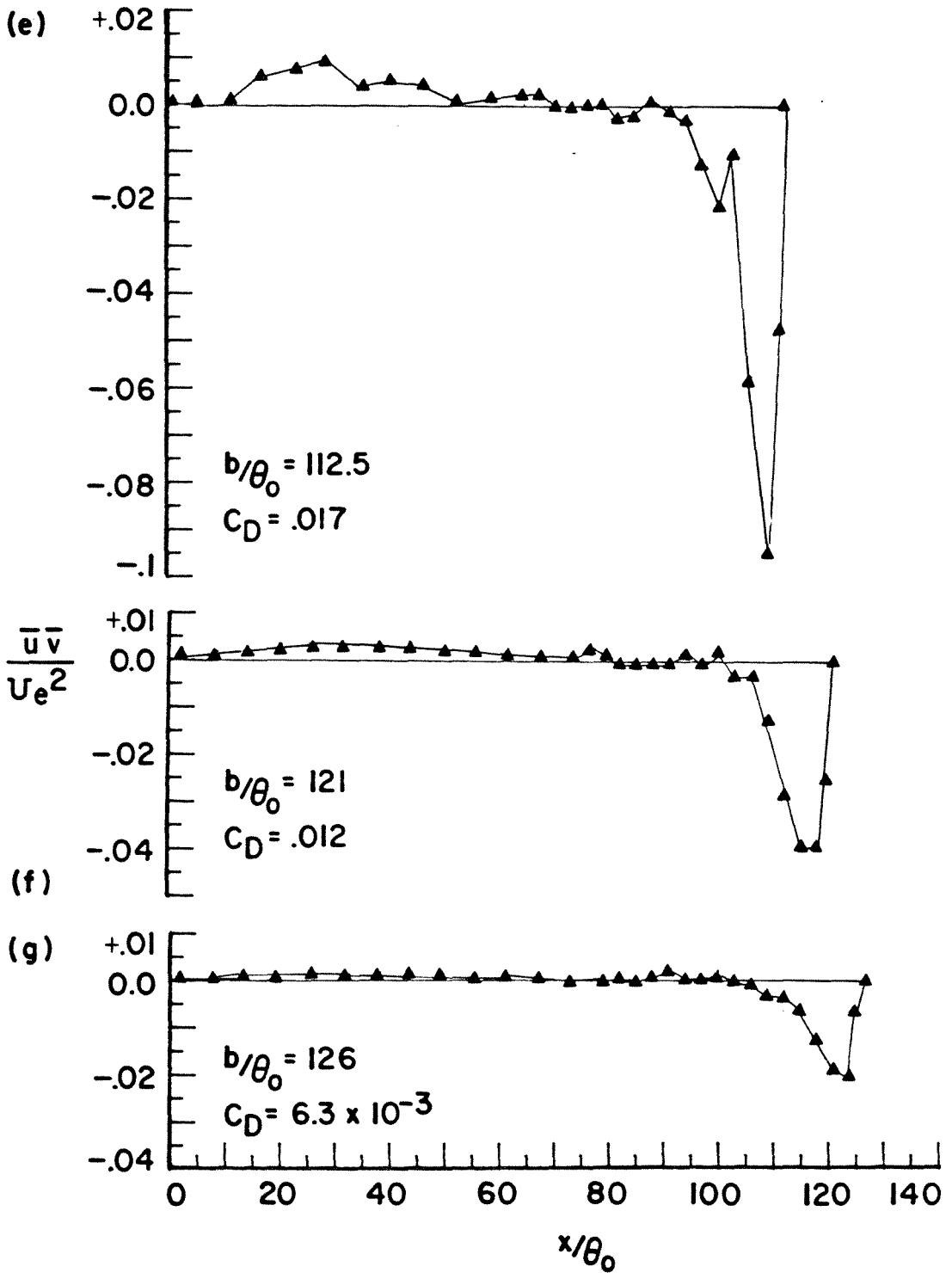

Fig. 52 Continued.

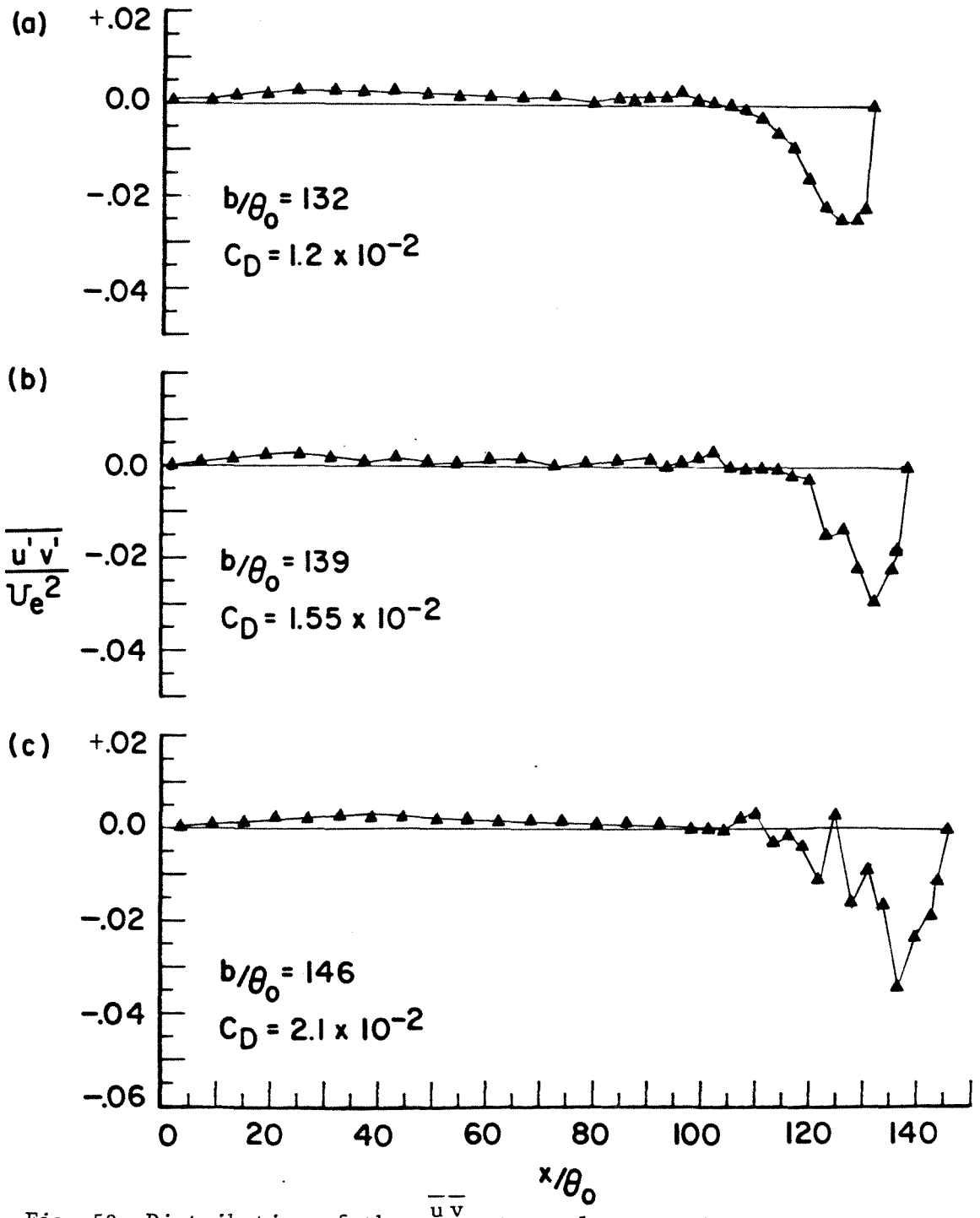

Fig. 53 Distribution of the $\frac{\overline{u}\,\overline{v}}{U_e^2}$ term along y = 0 line in Mode III.

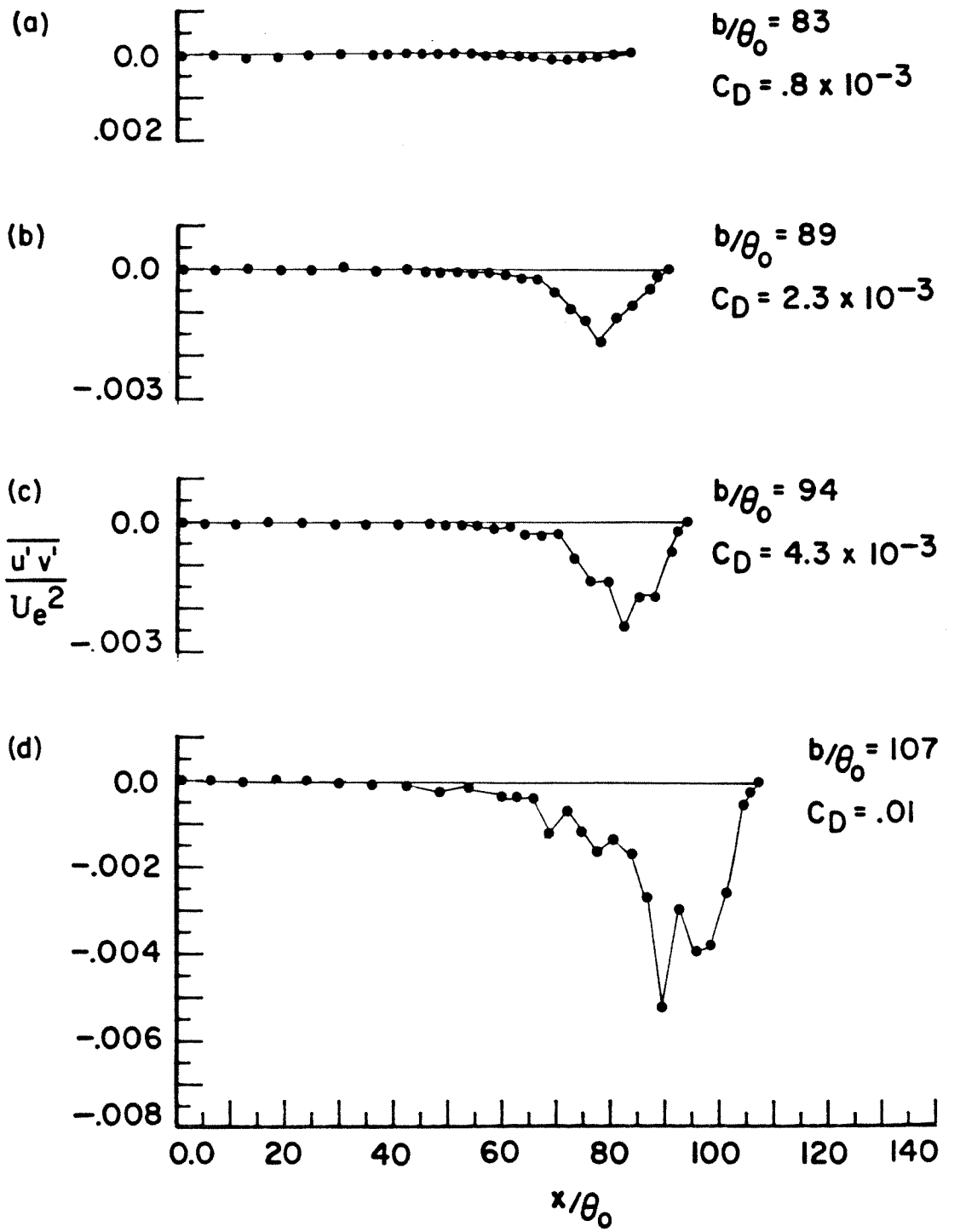

Fig. 54 Distribution of the shear stress along y = 0 line in Mode II.

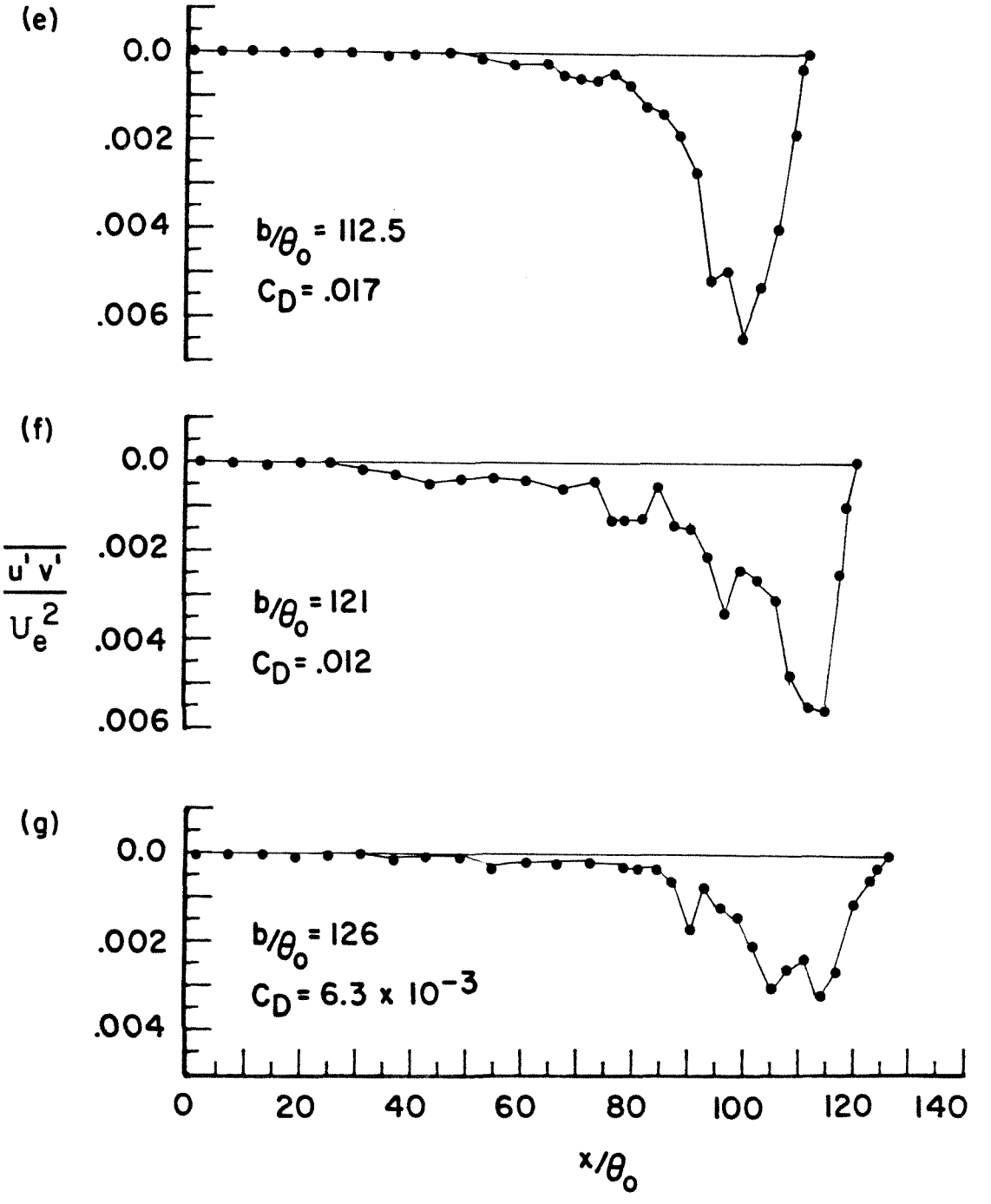

Fig. 54 Continued.

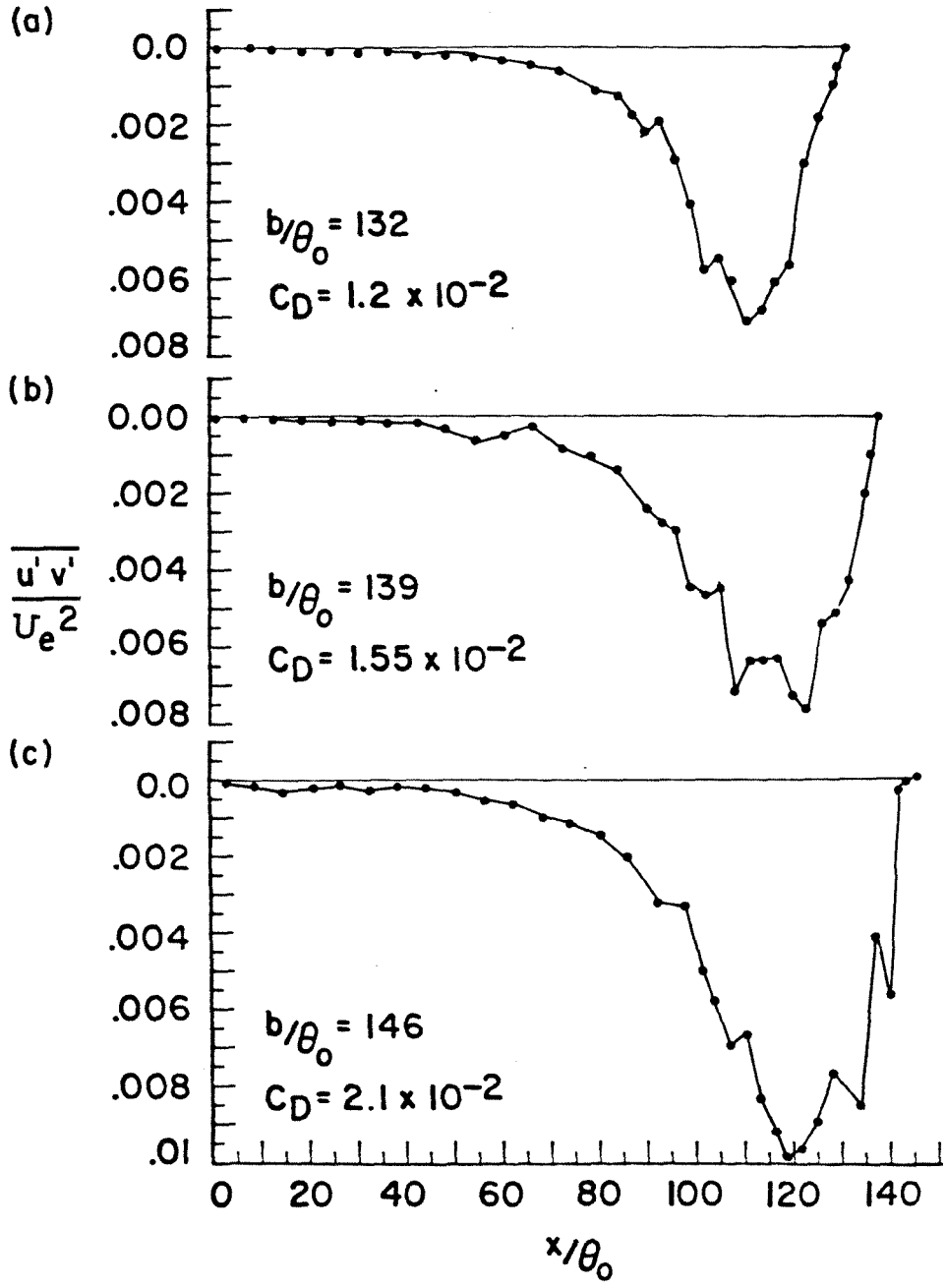

Fig. 55 Distribution of shear stress along y = 0 line in Mode III.

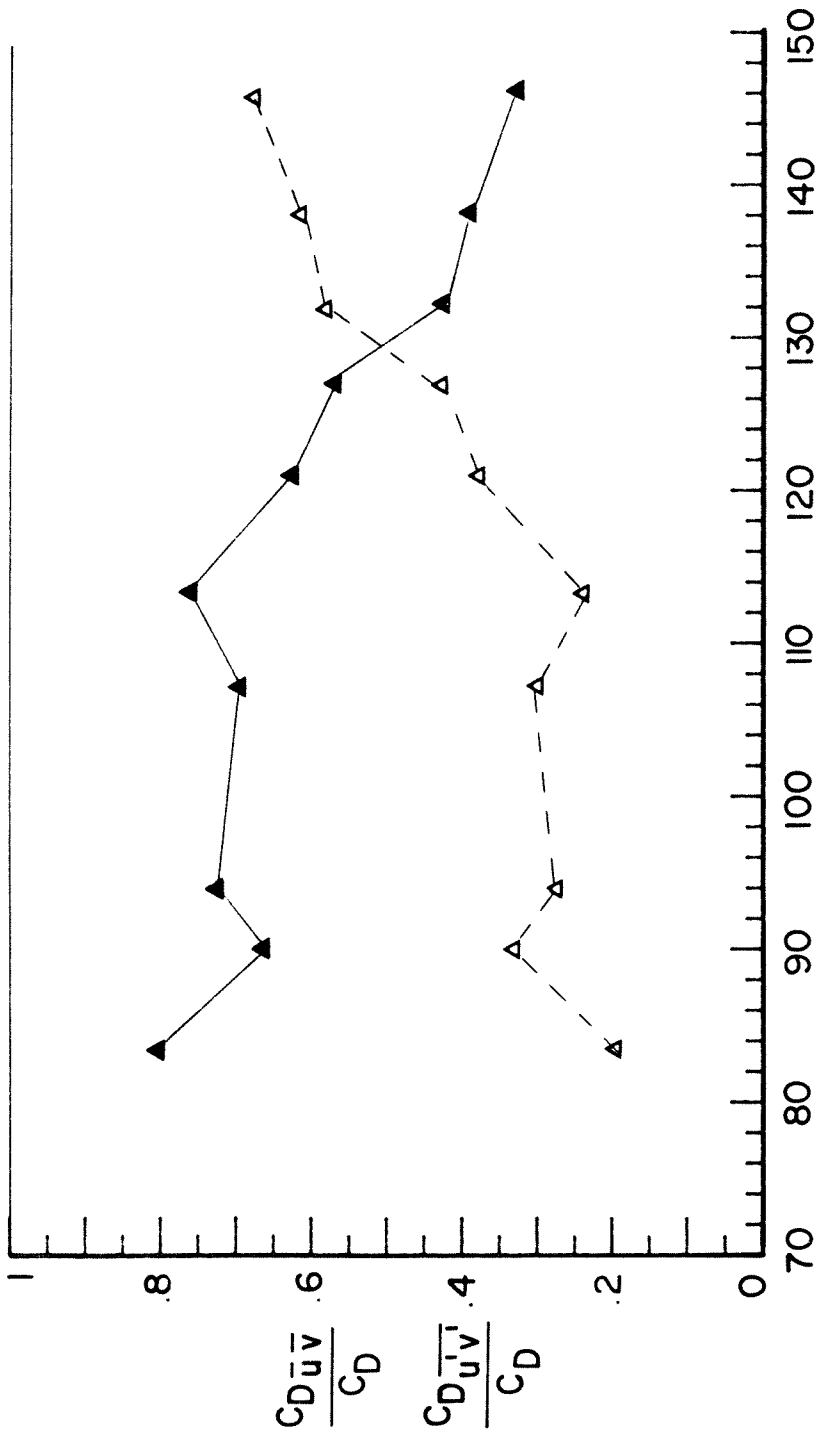

Fig. 56 ▲ Shear stress contribution to the net cavity drag

△ $\frac{\overline{u}\,\overline{v}}{U_e^2}$ term contribution to the net cavity drag

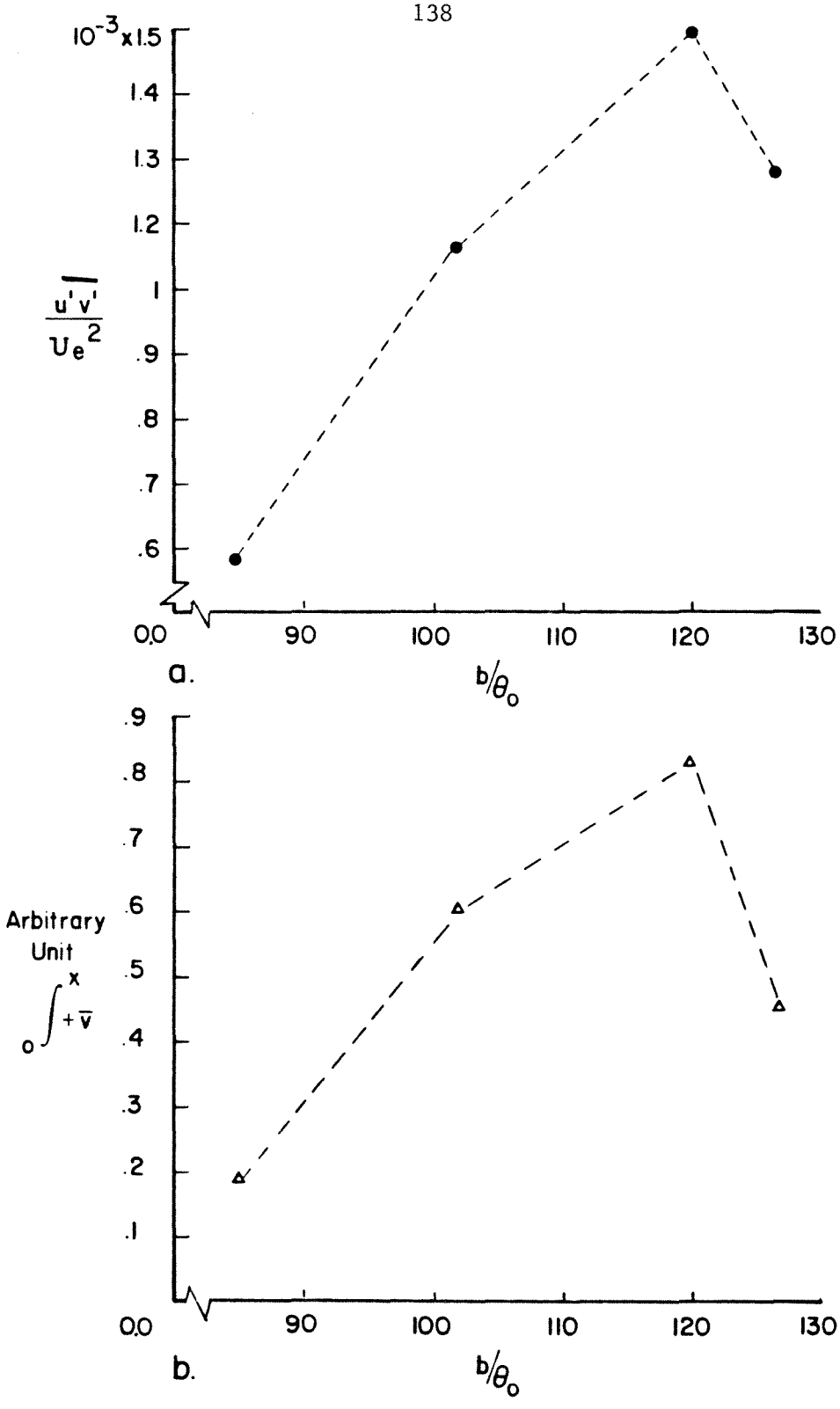

Fig. 57 (a) Variation of the shear stress at a fixed x/θ_0 with b/θ_0.

(b) Variation of the net positive outflow from the cavity with b/θ_0 .

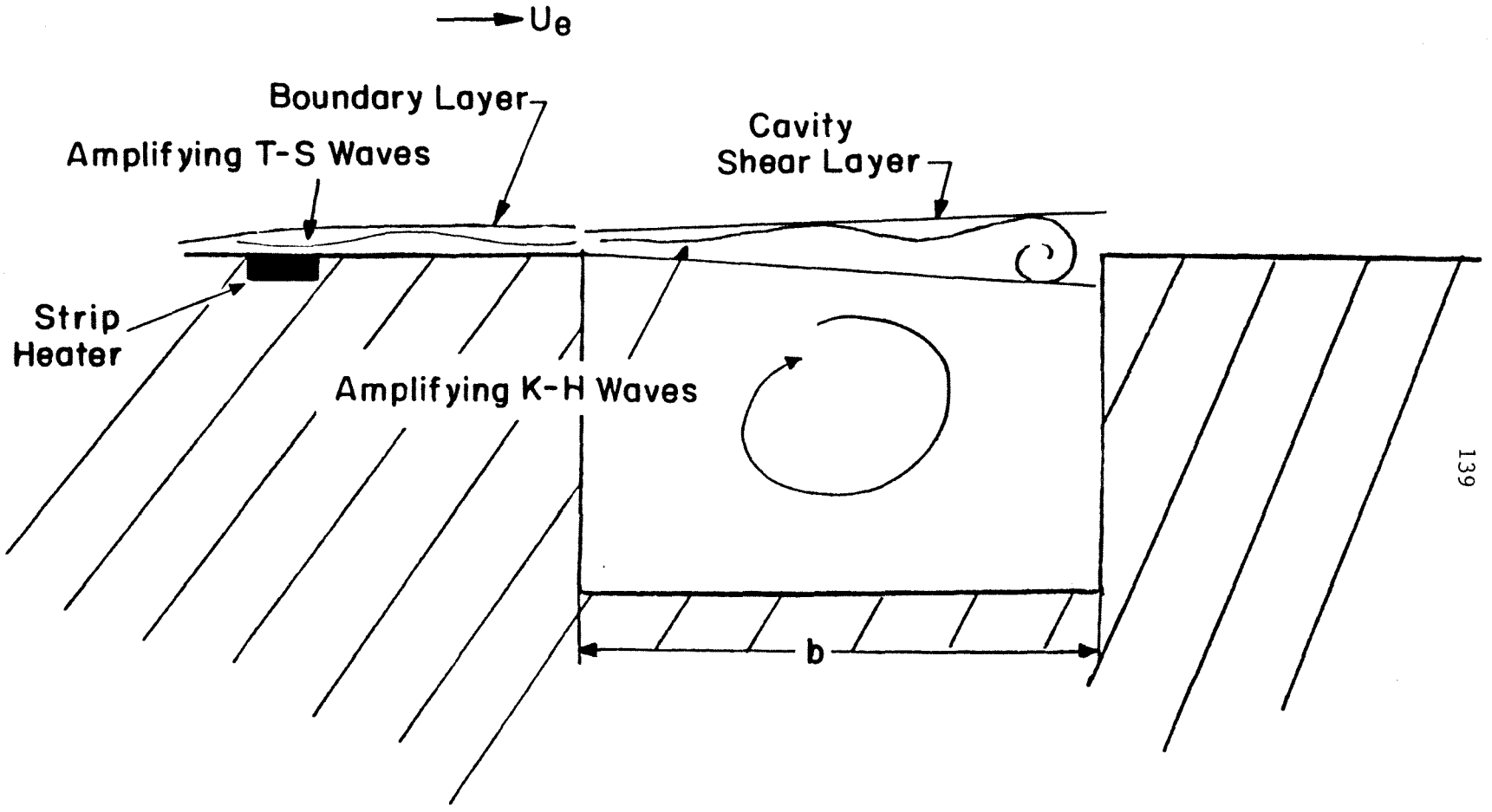

Fig. 58 Schematic of cavity flow illustrating the strip heater technique.

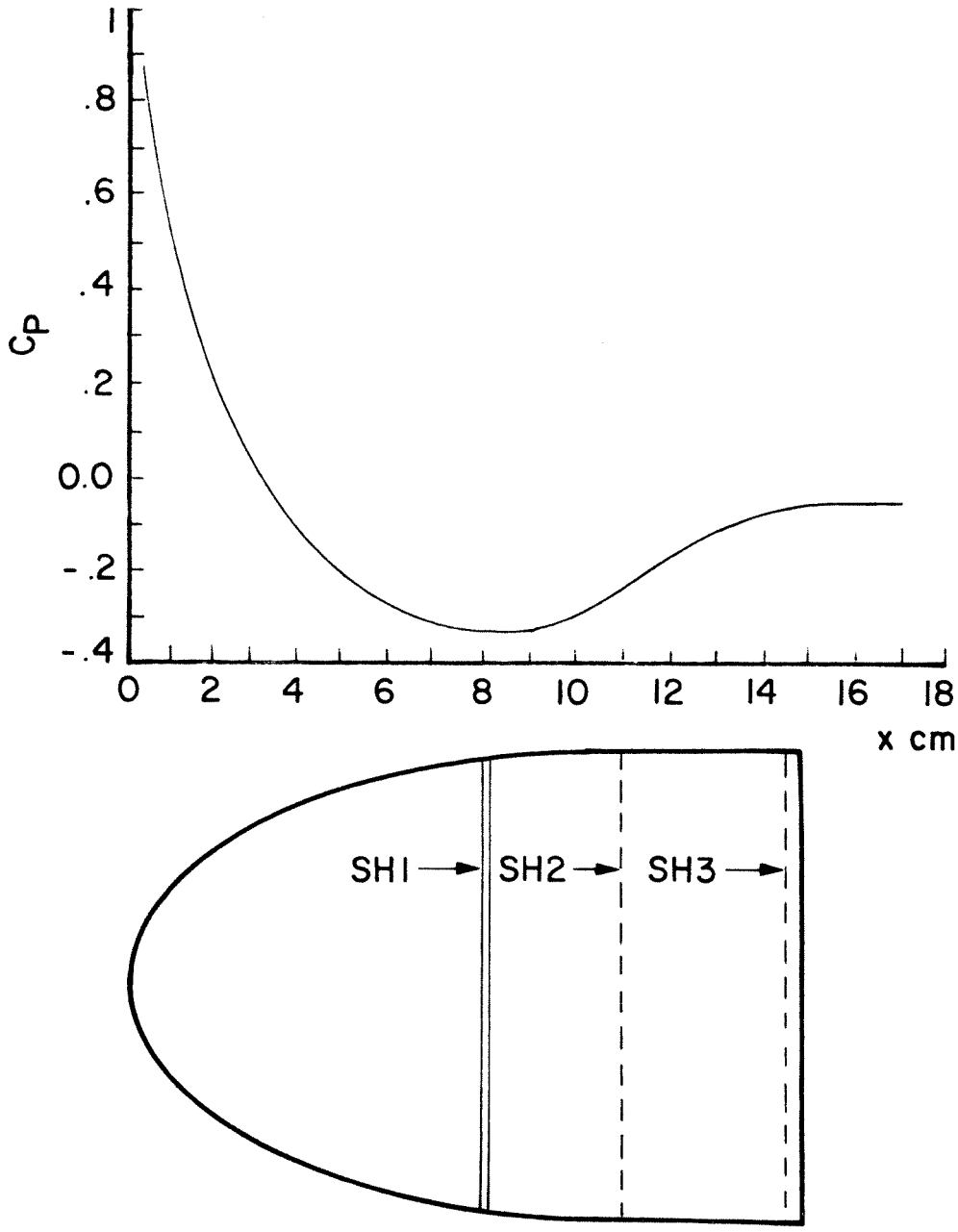

Fig. 59 Pressure distribution over the ellipsoidal nose cone and respective location of the strip heaters.

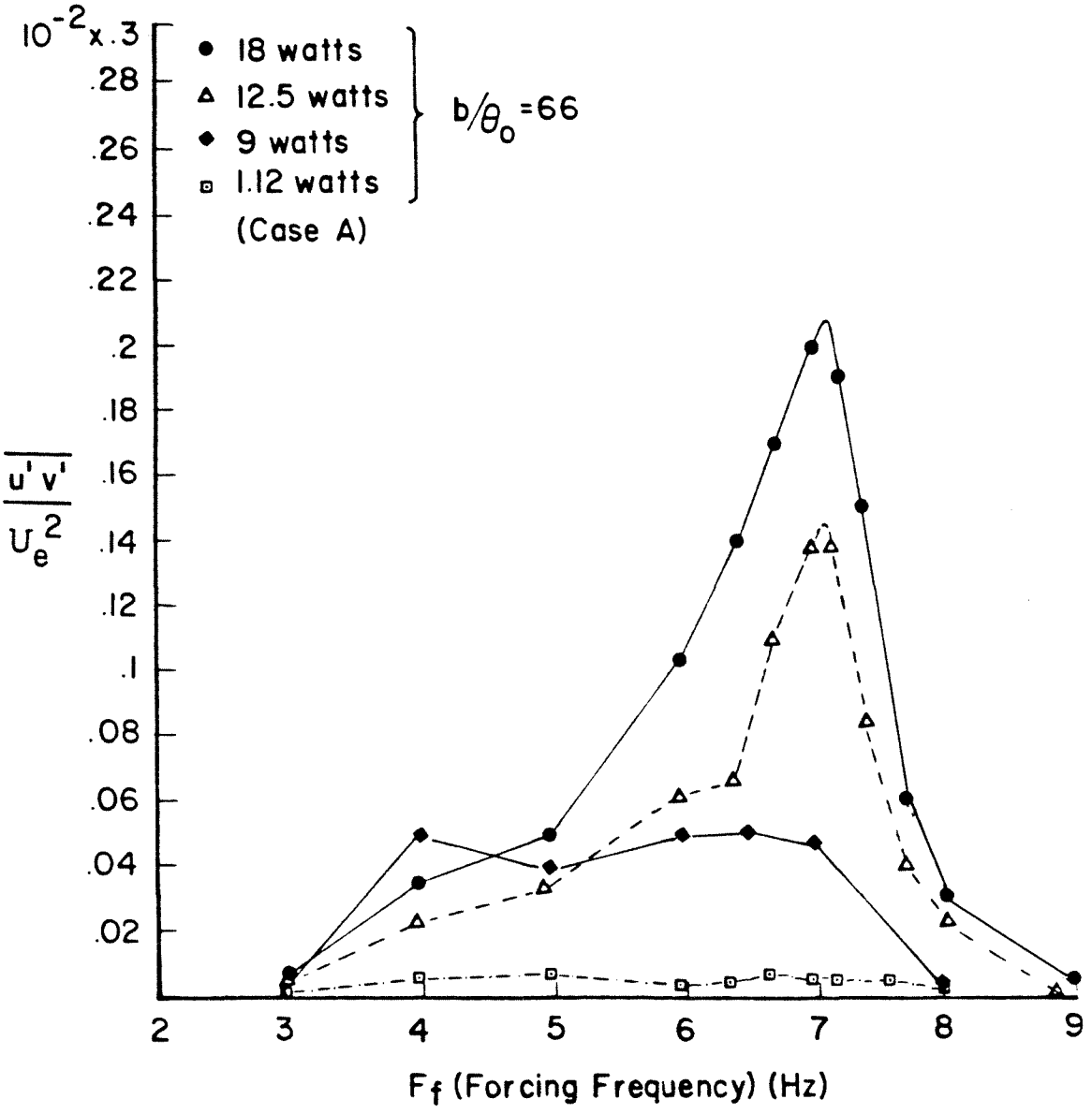

Fig. 60 Variation of maximum shear stress with forcing frequency at four different forcing power levels; Case A $b/\theta_0 = 66$, $U_e = 23$ cm/sec.

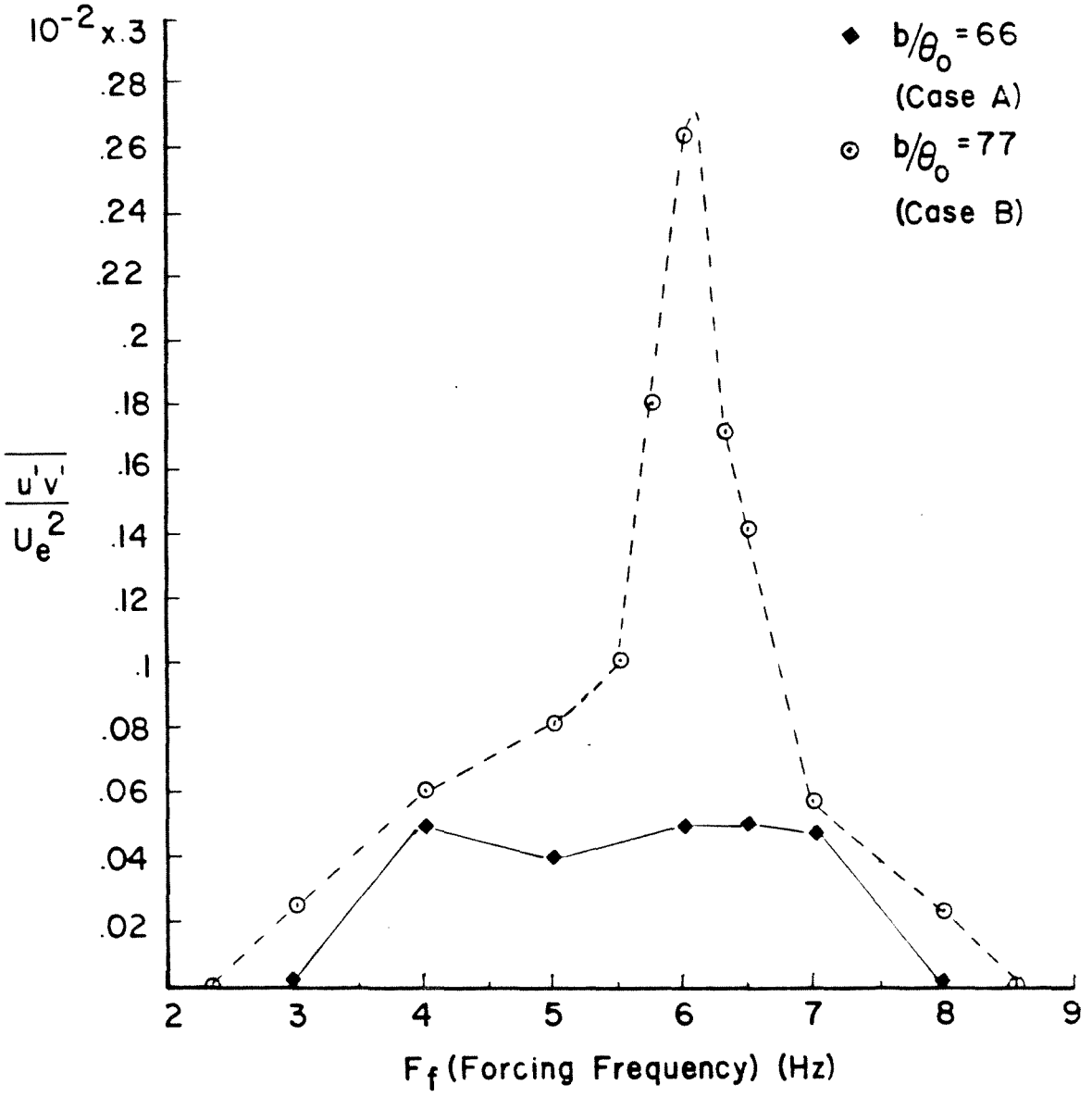

Fig. 61 Variation of the maximum shear stress in the shear layer with forcing frequency, constant power.

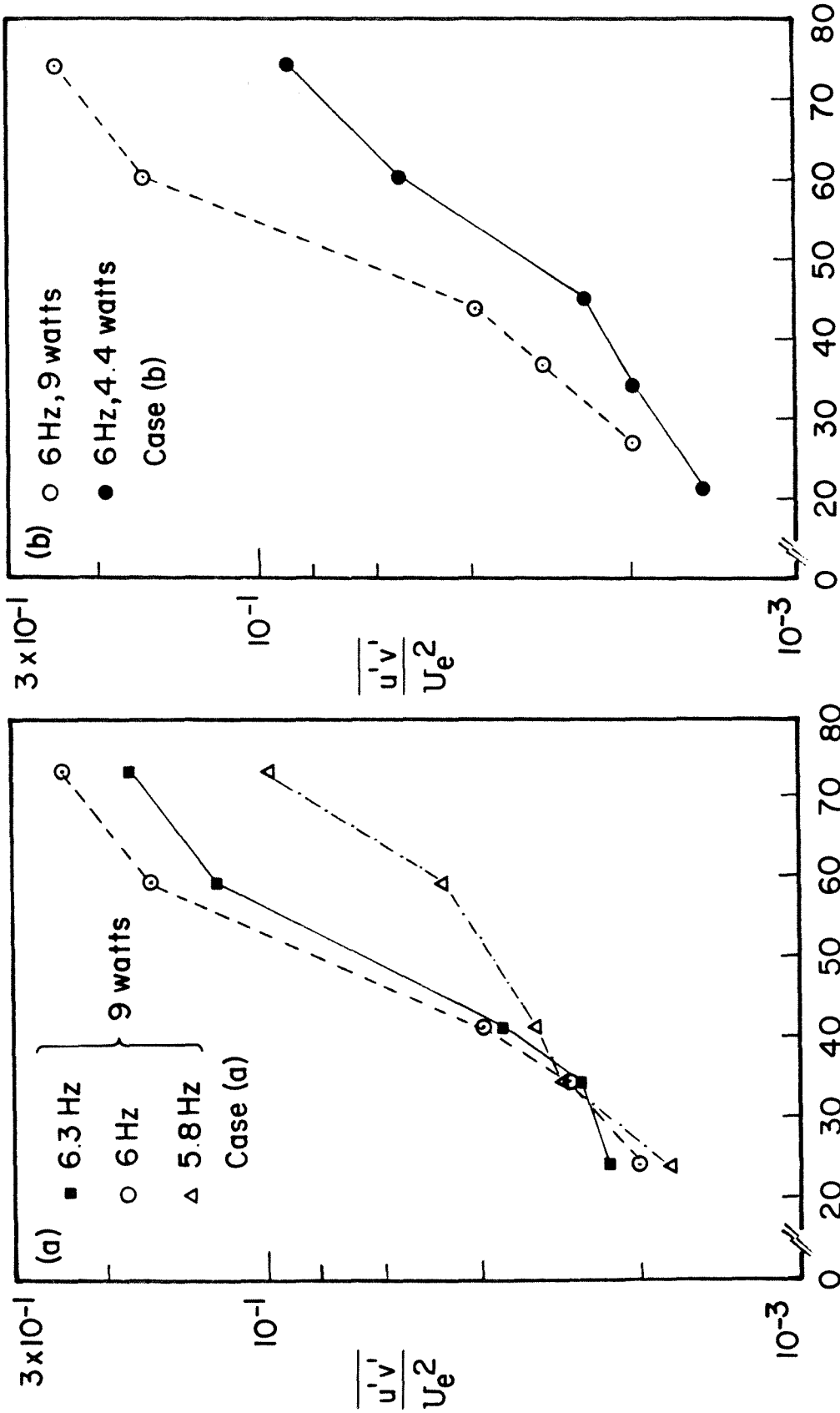

Fig. 62 Distribution of the maximum shear stress with the streamwise distance along the cavity shear layer; a) three different forcing frequencies, constant power; b) 2 different forcing powers, constant frequency; $b/\theta_0 = 77$.

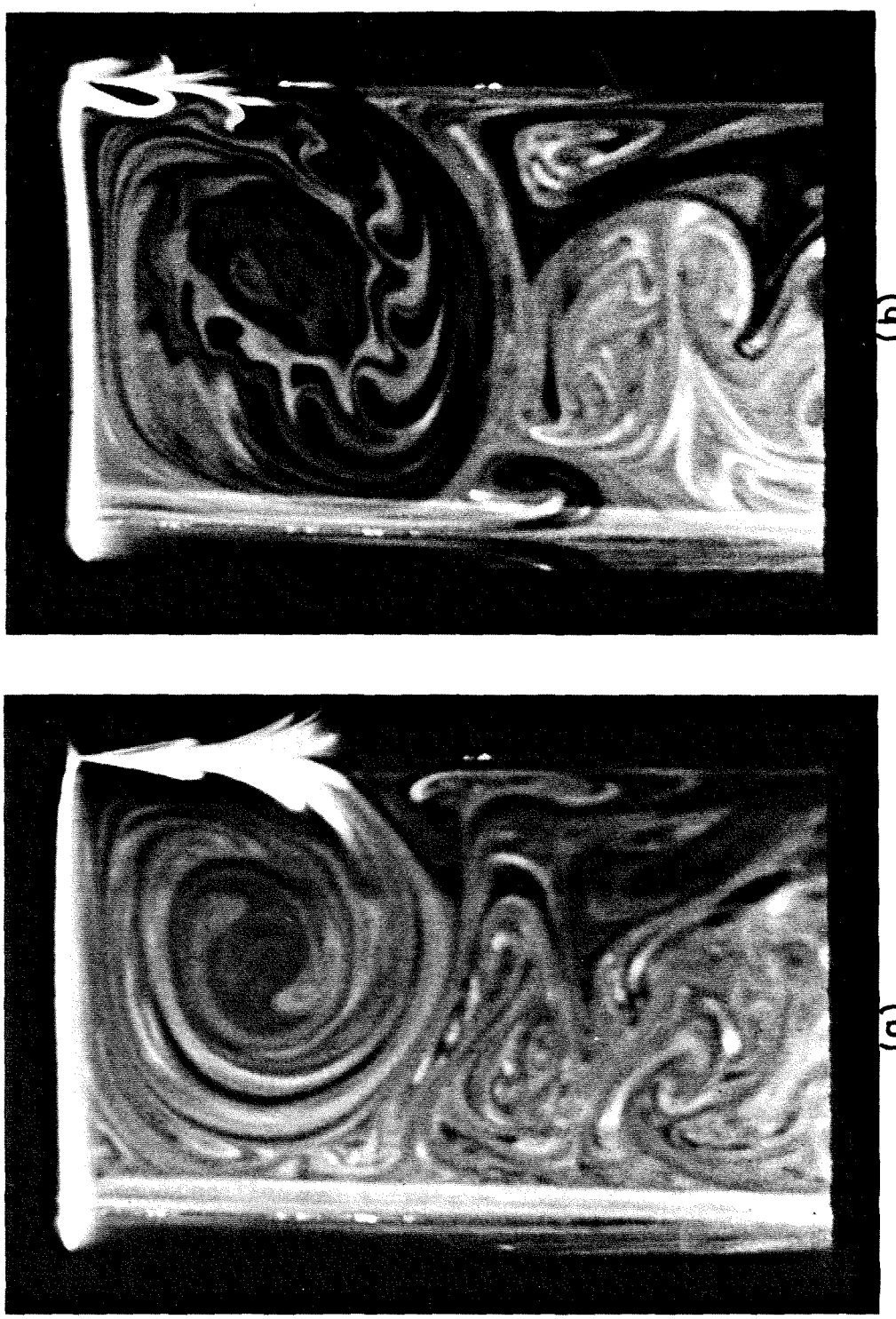

Fig. 63 Flow visualization of a naturally non-oscillating cavity flow; $b/\theta_0 = 66$. (a) unforced, (b) forced at F = 4 Hz, simulating Mode I of the oscillations.

a.

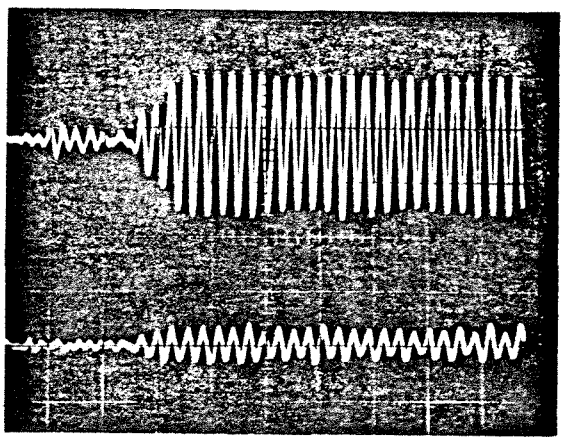

Horizontal scale .5 sec/div

b.

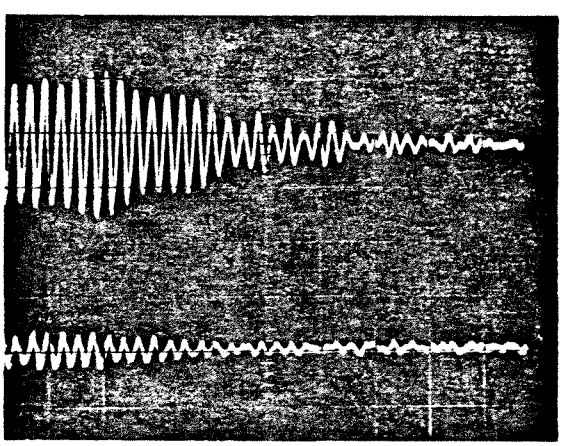

Horizontal scale .5 sec/div

Fig. 64 Oscilloscope traces of forced fluctuations, (a) turn on; (b) turn off; $b/\theta_0 = 66$, F = 7 Hz, $\frac{Fb}{U_c} = 2$.

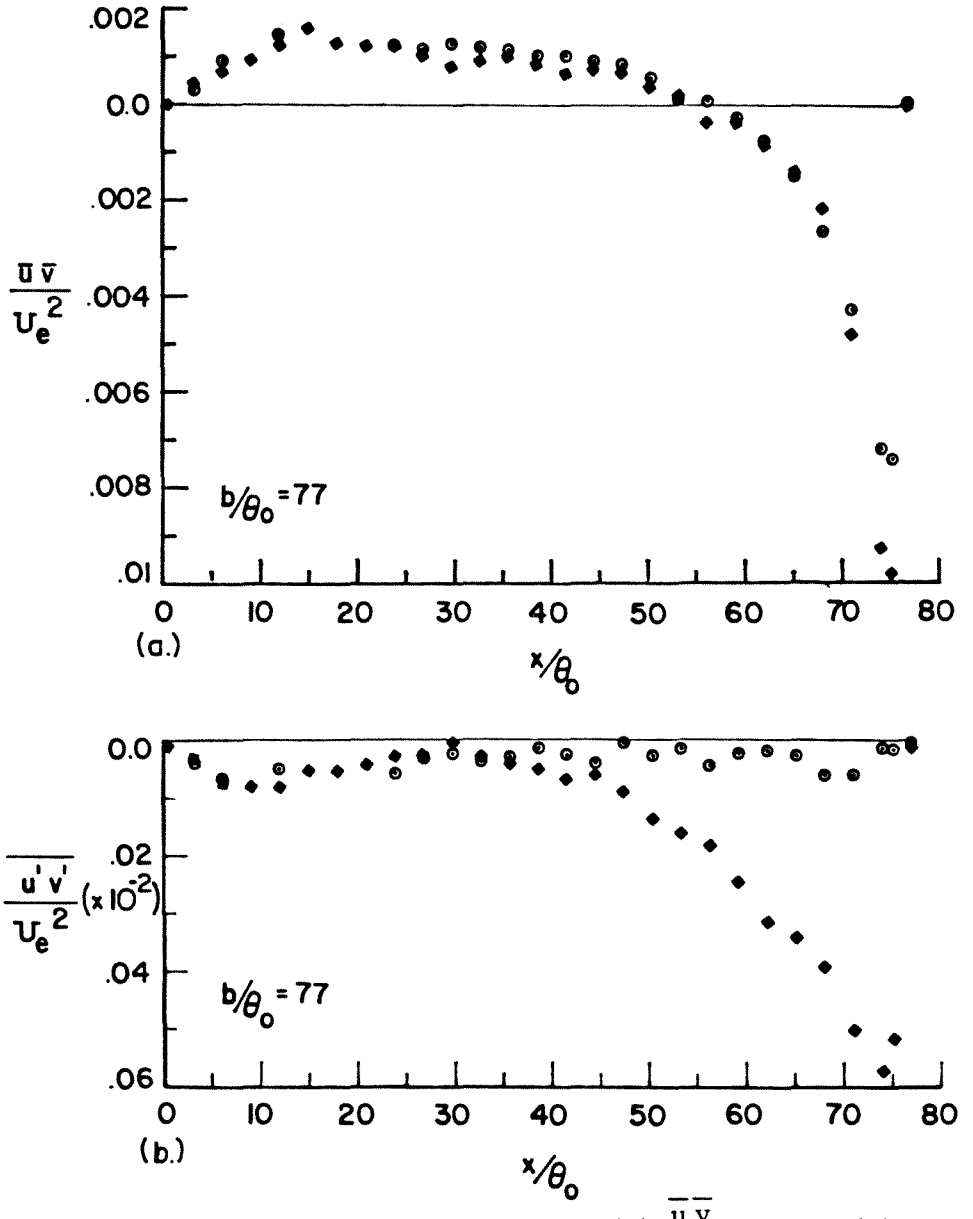

Fig. 65 Distribution of (a) $\frac{\overline{u}\,\overline{v}}{U_e^2}$ term, (b) shear stress along the y = 0 line in the non-oscillating mode; ⊙ unforced, ◆ forced at 6 Hz.

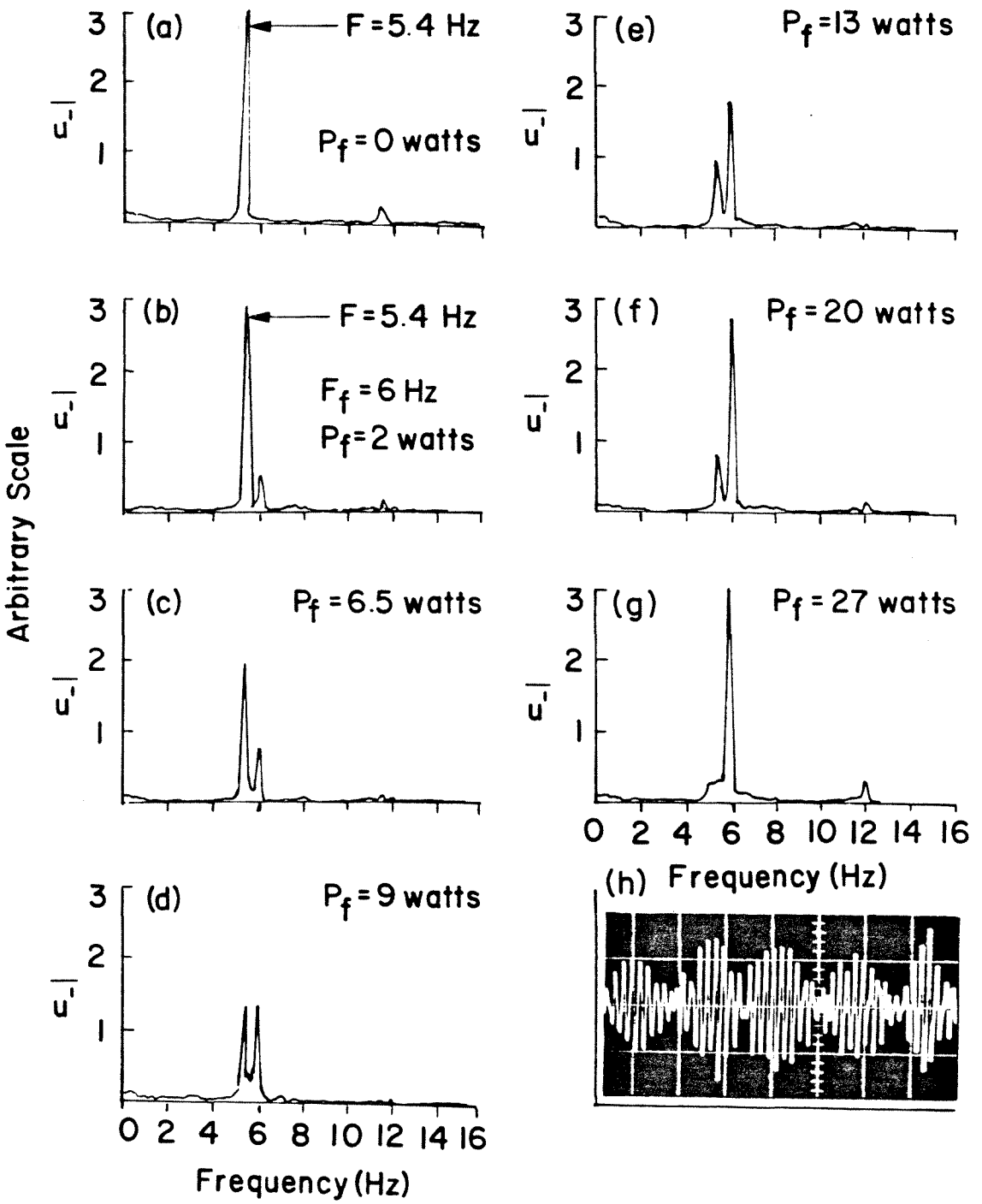

Fig. 66 Velocity fluctuation spectra, presenting interaction of the natural and forced frequencies in the cavity shear layer for different power levels (P_f), (h) scope trace of Case (d).

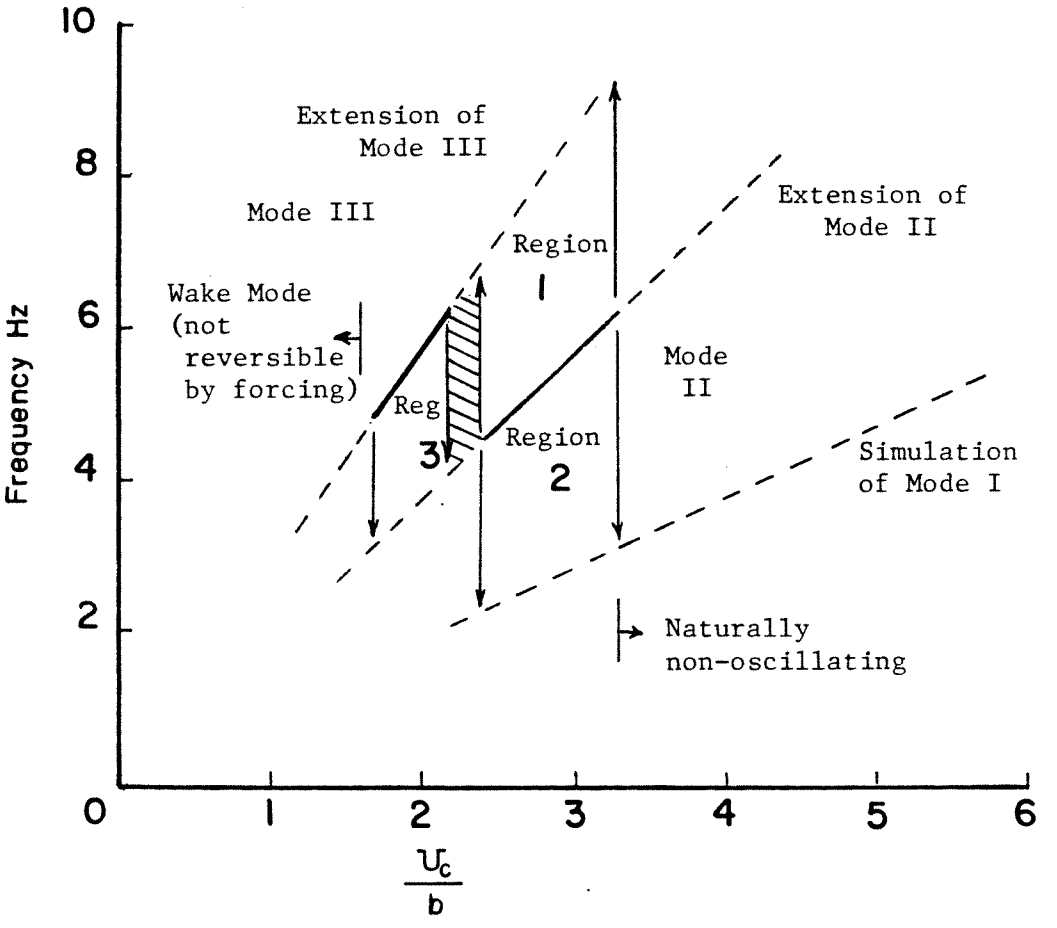

Fig. 67 Possible interactions with the cavity flow through external forcing.

1) Mapping of Mode II into Regions 1 and 2.
2) Mapping of Mode III into Region 3.
3) Extension of Mode II and III.
4) Delay of the wake Mode.
5) Simulation of Mode I.

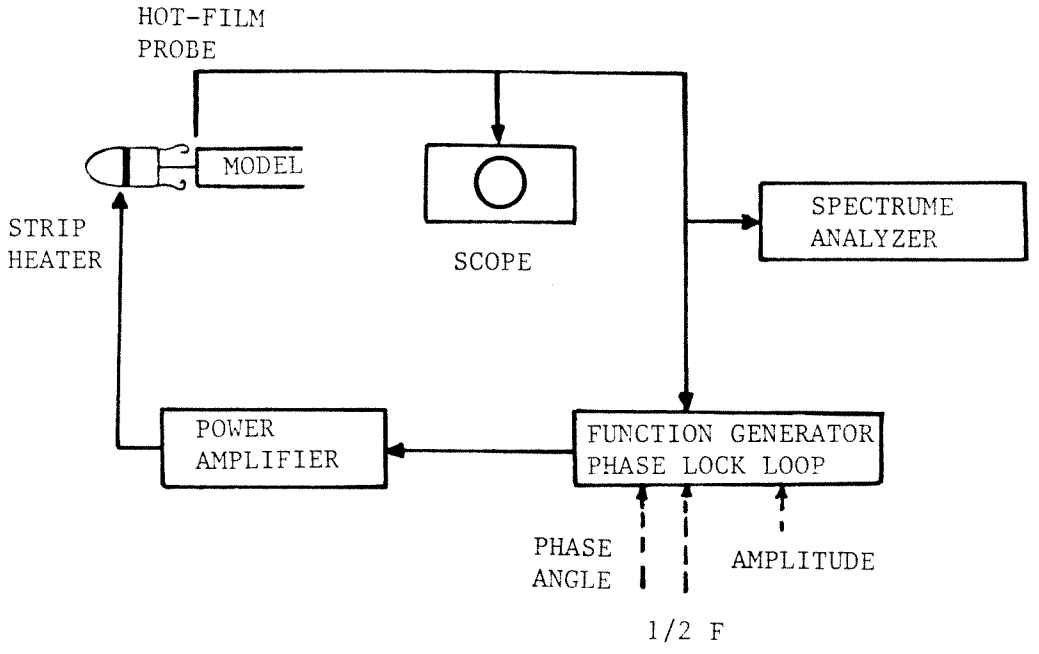

Fig. 68 Schematic of the cancellation set-up.

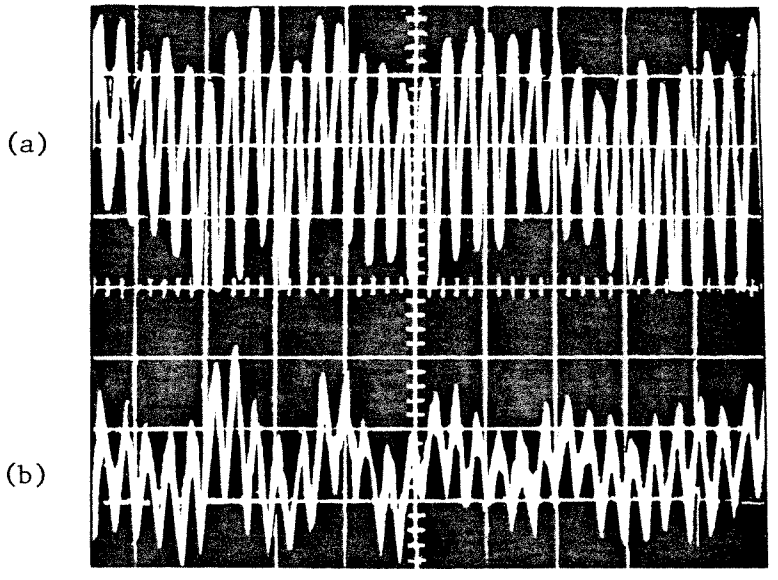

Fig. 69 Damping of natural oscillations through external forcing.
(a) natural oscillation
(b) strip heater on.

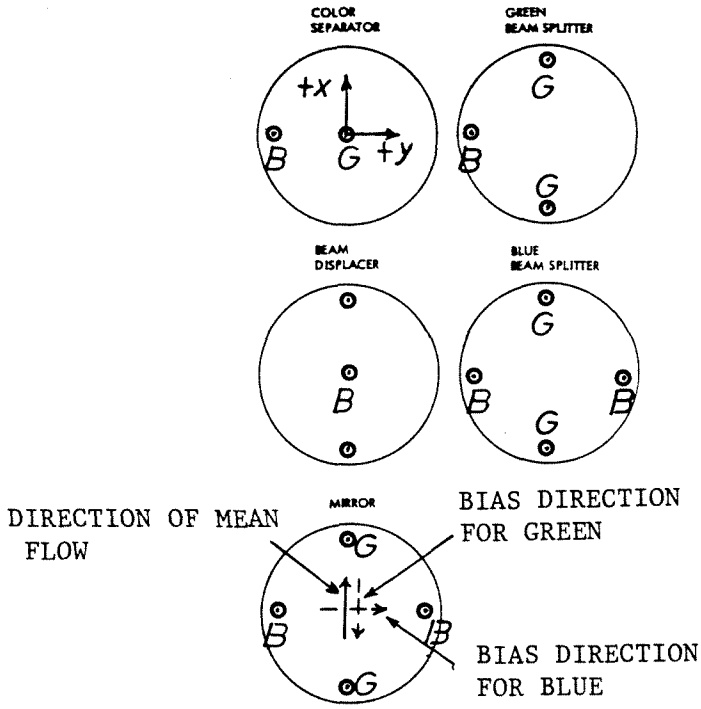

Fig. A-1 Measuring volume formation.

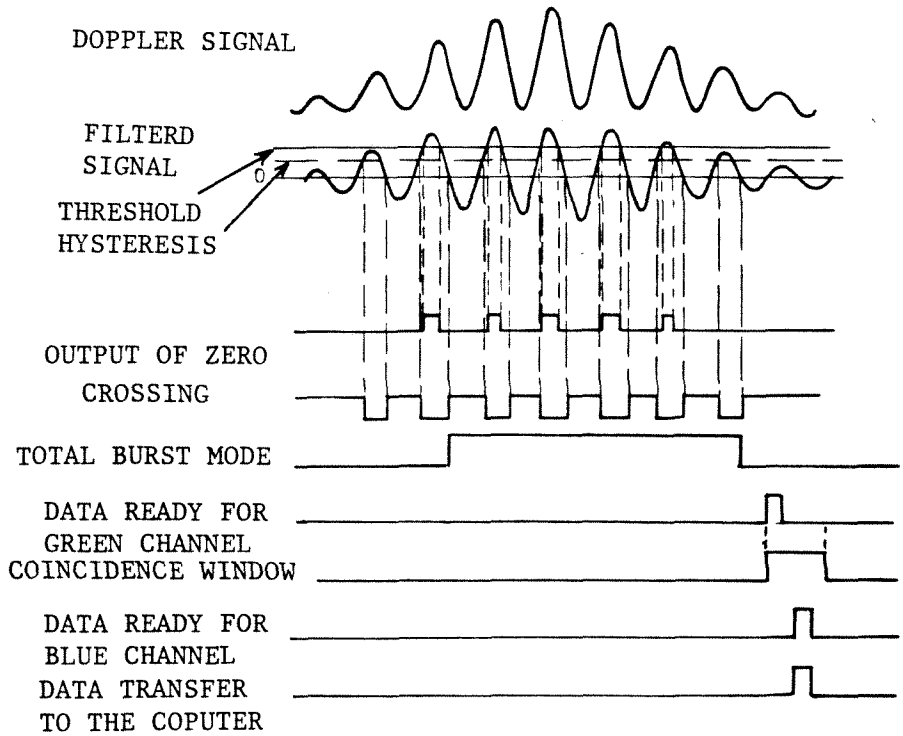

Fig. A-2 Valid burst processing and coincidence window operation.